

Artifact Correction
and Signal Quantification
in High Field Breast MRI

Mike van Rijssel

Artifact Correction and Signal Quantification in High Field Breast MRI

Mike van Rijssel

Artifact Correction and Signal Quantification in High Field Breast MRI

M.J. van Rijssel

PhD Thesis, Utrecht University, the Netherlands

Cover image: © Sabino Parente - Dreamstime.com

Photo of the author: © Tom Nauta Fotografie

Printing: Boekendeal.nl / PrintSupport4U B.V.

ISBN: 978-90-393-7196-1

The studies described in this thesis were supported by The Netherlands Organization for Health Research and Development (ZonMw, grant number 104003019).

The printing of this thesis was financially supported by ChipSoft and Pfizer BV.



Except where stated otherwise, this work is licensed under the Creative Commons Attribution-NonCommercial 4.0 International License. To view a copy of this license, visit <http://creativecommons.org/licenses/by-nc/4.0/> or send a letter to Creative Commons, PO Box 1866, Mountain View, CA 94042, USA.

Artifact Correction and Signal Quantification in High Field Breast MRI

Artefactcorrectie en signaalkwantificatie van MRI van de borst op hoog veld
(met een samenvatting in het Nederlands)

Proefschrift

ter verkrijging van de graad van doctor aan de
Universiteit Utrecht
op gezag van de
rector magnificus, prof. dr. H.R.B.M. Kummeling
ingevolge het besluit van het college voor promoties
in het openbaar te verdedigen op
dinsdag 26 november 2019 des middags te 2.30 uur

door

Michael Johannes van Rijssel

geboren op 10 mei 1991
te Haarlemmermeer

Promotoren:

Prof. dr. J.P.W. Pluim
Prof. dr. D.W.J. Klomp

Copromotor:

Dr. K.G.A. Gilhuijs

Contents

Chapter 1	General Introduction	7
Chapter 2	Estimating B_1^+ in the breast at 7T using a generic template	21
Chapter 3	Correcting time-intensity curves in dynamic contrast-enhanced breast MRI for inhomogeneous excitation fields	43
Chapter 4	Reducing distortions in echo-planar breast imaging at ultrahigh field with high-resolution off-resonance maps	61
Chapter 5	Untangling the diffusion signal using the phasor transform	79
Chapter 6	Summary & General Discussion	105
Appendix	Nederlandse samenvatting (Dutch summary)	116
	List of publications	128
	Dankwoord (Acknowledgements)	130
	About the author	135



General Introduction



1.1 Glow-in-the-dark stars

This thesis is about magnetic resonance imaging (MRI). But before we dive into that subject, let's briefly discuss the glow-in-the-dark stars that you probably had on the ceiling of your childhood bedroom. (If you didn't actually have those, perhaps you owned a watch with glow-in-the-dark hands at some point?) A particularly curious child, like the author of this manuscript, might wonder how those stars keep on glowing long after the lights have been switched off. The answer is a chemical process called phosphorescence, which causes electrons in the glow-in-the-dark paint on those stars to enter a higher energy state after absorbing energy from light, essentially 'charging' the star (1). This energy is then slowly released, causing the stars to glow up to hours after the light went off.

In many ways, making an MRI scan is just like taking a photo of glow-in-the-dark stars glowing in a dark room. In both cases, a recording is made of an object radiating electromagnetic waves. In both cases, this recording is only made after the original source of electromagnetic energy that excited the object is switched off. There are some obvious differences too. In MRI, the object is usually a human being. And the kind of electromagnetic radiation is not in the visible spectrum, but in the megahertz-range, the same range that FM-radio and VHF-television channels (used to) use.

Even though it is a simplification, the analogy with glow-in-the-dark is useful in order to understand an important concept in MRI: we have to excite our object of interest (or turn on the lights in the room to charge the stars) before we can acquire a signal (or take the photo). It also helps to get an intuitive understanding of what happens to our image when the excitation is not equally distributed throughout the imaged object. Just like the light intensity emitted by a glow-in-the-dark star located in a particularly dark corner of the room, the signal intensity in poorly excited regions of the image will be different.

Such non-uniformity effects can negatively impact the diagnostic performance of MR images. This thesis investigates the assessment of and correction for such field non-uniformities, specifically in the context of high field breast MRI. To properly introduce the field non-uniformities covered in this thesis and the artefacts that they cause in breast MRI, the oversimplified glow-in-the-dark stars analogy does no longer suffice. Therefore, the next section briefly introduces some important concepts in MRI, specifically related to the topics investigated in this thesis. This is by no means a comprehensive account of the MR physics involved with the imaging techniques used in this thesis. A more thorough discourse on this subject can be found in the book by Brown *et al.* (2).

1.2 Important concepts in MRI

1.2.1 Resonance

MRI scanners work with very strong magnetic fields, commonly in the order of 0.5 – 3 T. When a diamagnetic object, such as a glass of water, a piece of fruit or even a human volunteer or patient is put into such a strong magnetic field, the fields from hydrogen atoms (or protons) inside it will align with the magnetic field. Additionally, these proton fields start precessing (spinning) with a frequency determined by the strength of the magnetic field. Much like the rotation speed of windmills is determined by the

strength of the wind: the higher the magnetic field strength, the faster the precession of the proton spin. The frequency of this precession is called the Larmor resonance frequency.

1.2.2 Signal Generation

Putting the object in a magnetic field will cause the spins to align and resonate, but this is not enough to generate an MR signal. In order to do so, we need to rotate the spins to be perpendicular to the main magnetic field. This rotation is achieved using a radio wave with the same frequency as the resonance frequency described above. Since this radio wave is typically very short in duration, just a few milliseconds, it is often called a radiofrequency (RF) excitation pulse.

We can choose how far we want to rotate or flip the spins with respect to the main magnetic field by changing the amplitude of the RF pulse. MRI scanners conveniently allow you to specify the amplitude by inputting the desired flip angle. Up to a certain extent, the higher the flip angle, the higher the generated signal will be. After the flip angle is applied, the magnetization along the main magnetic field, the longitudinal magnetization, will be decreased. This is temporary, since the longitudinal magnetization will slowly restore. The time it takes for this magnetization to regrow is measured using the T_1 relaxation time, which is typically in the order of seconds. If we generate another signal before the longitudinal magnetization has fully restored, this second signal will be lower than the first. Since in MRI we need to generate many signals before we've acquired a full image (the reason for this will become apparent once we discuss position encoding) it is important to consider what happens if we apply many RF excitations in a rapid succession.

1.2.3 T_1 weighting

As mentioned, the T_1 is typically in the order of seconds, e.g. the T_1 of breast glandular tissue is around 2 seconds at 7 T. The most common type of breast MRI sequence typically uses a repetition time (TR) of around 5 - 15 milliseconds. That means that every 5 - 15 milliseconds we apply an RF excitation to generate some signal. At the start of the sequence, before any RF is applied, the longitudinal magnetization is at its maximum and a high amount of signal is generated after the first flip angle is applied. With every repetition however, the amount of signal will reduce because the longitudinal magnetization has too little time to fully regrow. This goes on until at some point the reduction of the magnetization due to the excitation and its regrowth between RF pulses are equal. This is called the steady state.

The amount of longitudinal magnetization in the steady state, as well as the amount of signal generated, depend on the T_1 of the tissue, the applied flip angle and the chosen TR. Since the T_1 measures the time it takes for the longitudinal signal to regrow, a shorter T_1 causes a higher signal. So does a longer TR. The influence of the flip angle is a little more complicated. A flip angle of 0 obviously generates no signal at all. A very high flip angle generates a very low signal because the longitudinal magnetization ends up in a very low steady state. In between these extreme cases there is an angle at which the maximum amount of signal is generated: this angle is called the Ernst angle. Figure 1.1 shows a plot of the amount of signal generated for a range of flip angles and for two

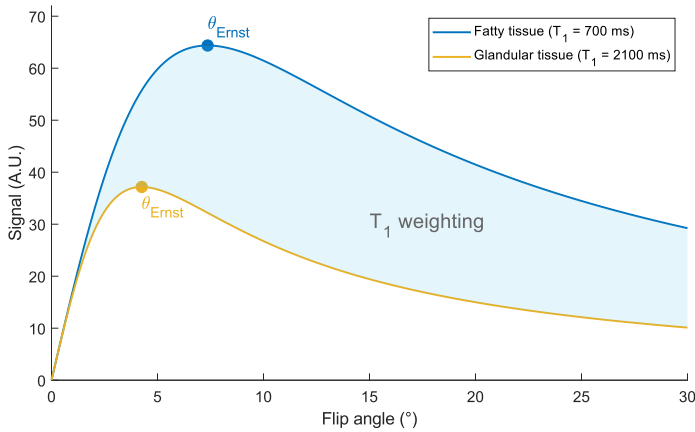


Figure 1.1: Steady state signal as a function of flip angle for either breast fatty tissue (blue, $T_1 = 700$ ms) or breast glandular tissue (yellow, $T_1 = 2100$ ms). Higher flip angles increase the relative difference in signal from these two tissues. Abbreviation: A.U. - Arbitrary Units.

tissues with a different T_1 . Higher flip angles enlarge the relative difference between signals coming from tissues with a different T_1 . This concept is called T_1 weighting and allows us to better discriminate between different tissue types.

1.2.4 Position Encoding

In order to be able to generate images using magnetic resonance, we need to know where the signals we generate come from. As discussed before, proton fields in a magnetic field resonate at the Larmor frequency and the signals we generate and receive also have this frequency. In an MRI scanner with a nicely homogeneous magnetic field, all proton spins will resonate at exactly the same frequency and there is no way for us to tell their signals apart. However, if there are slight differences in the magnetic field, the resonance frequencies shift with those and we can suddenly distinguish groups of signals stemming from different groups of protons sending signals at different frequencies.

In order to exploit this for position encoding, we apply these differences to the magnetic field in a very systematic way. We turn on an extra magnetic field, called a gradient field, which increases linearly from one side of the scanner to the other side of the scanner. For example the x-gradient that increases linearly from left to right. Now all protons on the left side are sending signals at a lower frequency than those on the right. In order to know how many protons were sending signals from each position, all we need to do is determine how much signal we received at each frequency. If we map this back to the position we associated to each frequency using our gradient field, we end up with a one-dimensional image of the object in our scanner.

MRI scanners are equipped with gradient coils in three orthogonal dimensions, which allow us to generate three-dimensional images. This is usually performed by acquiring lines of position encoded frequencies at a time. In order to measure the entire object, many repetitions are needed. Therefore, depending among other things on the image

resolution and the size of the image, typical in-vivo MRI scan times vary between several seconds to several minutes.

1.3 High field breast MRI

Breast MRI is a valuable imaging tool in the clinic. Though breast cancer diagnosis is mainly performed using a combination of x-ray mammography, ultrasound and biopsy, MRI is routinely used in the clinic for tumor evaluation prior to surgery, treatment monitoring after or during (neoadjuvant) chemotherapy and breast cancer screening in high-risk populations (3). Its sensitivity in detecting invasive breast cancer is superior to both mammography and ultrasound (4). Additionally, MRI is the most accurate imaging modality in assessing tumor size (5).

Currently, breast MRI is performed in the clinic using field strengths up to 3 T. Higher field strengths up to 7 T are used in clinical trials. Advantages of performing MR at higher field strengths include a higher signal-to-noise ratio (SNR) and a higher chemical shift dispersion (6). The first advantage can be used to increase spatial resolution, which has been shown to be feasible at 7 T in a clinical setting and might have potential for earlier and better diagnosis (7,8). The second advantage can be used to measure tumor metabolism using spectroscopy techniques. Measurements of this kind may be able to predict the response to neoadjuvant therapy in an earlier stage of treatment, enabling faster switching of treatment strategy if necessary (9,10).

Using higher field strengths also has disadvantages. The main disadvantage we zero in on in this thesis is that the electromagnetic fields we use become less uniform (6). The first electromagnetic field we explore is that of the RF excitation pulse. This RF transmit field (B_1^+) indicates how much electromagnetic energy from our RF excitation pulse actually reaches each position of the image. The second electromagnetic field that is affected is the permanent, main magnetic (B_0) field of the MRI scanner. The inhomogeneities of these electromagnetic fields cause artifacts in the recorded images. These artifacts can be so severe that they decrease the diagnostic value of the images (11). Therefore, this thesis focused on artifact correction in two imaging sequences often used in breast MRI: dynamic contrast-enhanced MRI (DCE-MRI) and diffusion weighted imaging (DWI).

1.4 DCE-MRI

In DCE-MRI the patient is injected with a T_1 -shortening contrast agent during the MRI scan. Due to their rapid growth, tumors tend to have more and leakier blood vessels (12). Consequently, a higher amount of contrast agent leaks from those vessels into the tumor (13). This, in turn, causes the T_1 of the tumor to decrease and the MR signal from the tumor to increase. Figure 1.2 shows an example of this. Over time, the contrast agent will leak back out of the tumor into the vessels. During a DCE-MRI scan multiple images are recorded over time, such that the speed of both the initial signal increase and the sequential signal decrease can be measured. These can be linked to the aggressiveness of the measured tumor: faster contrast agent uptake and release are indicative of a more aggressive tumor (14).

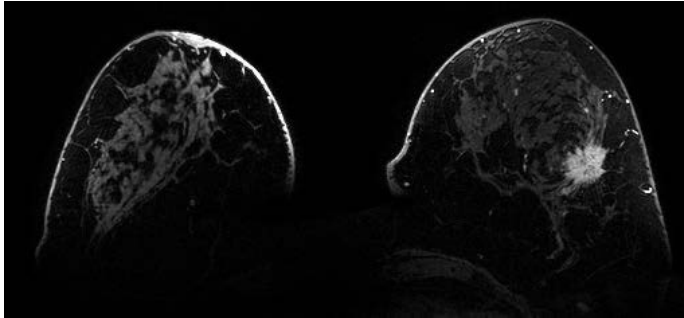


Figure 1.2: 7 T DCE-MRI of a patient with a breast tumor in the left breast (shown right). The tumor has an enhanced signal due to the injected contrast agent. Note that this image is also prone to the B_1^+ non-uniformity artefact. Abbreviation: DCE-MRI - Dynamic Contrast-Enhanced Magnetic Resonance Imaging.

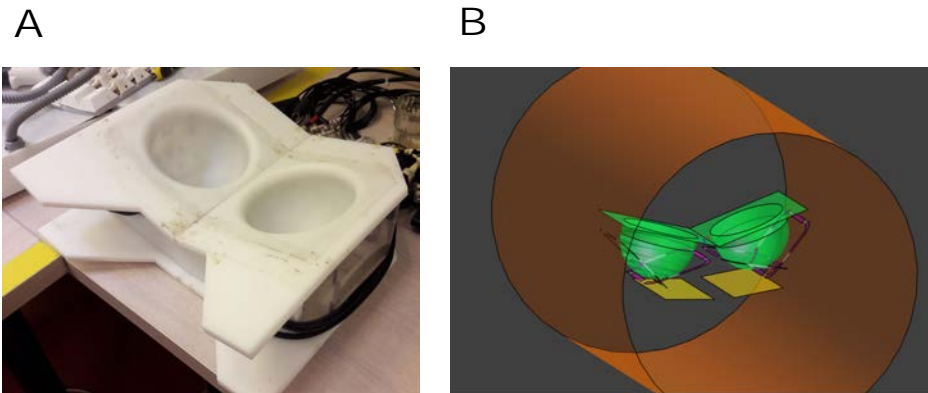


Figure 1.3: A: The bilateral local transmission breast coil used in this thesis. B: Schematic view showing the same coil positioned inside an MRI scanner, with the cups visible in panel A shown in green. The actual transmit coil elements are shown in white and purple. The orange cylinder represents the tunnel of the MRI scanner.

Early whole-body imaging experiments at 7 T revealed major inhomogeneities in the B_1^+ field distribution (15). These are due to the decreased wavelength of RF excitation at increasing field strengths, which causes standing waves in the excitation field and a lowered B_1^+ efficiency overall. All 7 T breast MRI experiments in this thesis use local transmission coils, which facilitate a high B_1^+ in the breast (16,17). Figure 1.3 shows a local transmission coil that was used in this thesis. Since these coils are positioned in front of the body and B_1^+ decreases with the distance from the coil, there is a lower amount of B_1^+ in the posterior parts of the breast.

In order to understand the effect of a low B_1^+ level on the acquired images, it is important to realize that a low B_1^+ level essentially means a lower flip angle. As was described in the section on T_1 weighting, a lower flip angle not only causes a different amount of signal generation in the steady state, it also means that the resulting image will have a lower amount of T_1 weighting. In other words, a low B_1^+ level also causes a lower sensitivity to changes in T_1 . Since the contrast agents used in DCE-MRI shorten the T_1 , a

low B_1^+ level also causes a lower sensitivity to changes in contrast agent concentration, which complicates tumor diagnosis (18).

The first step in trying to correct for this artifact, is to determine how much B_1^+ actually reached all parts of the image. Many methods have been proposed to map B_1^+ , each faster or more accurate than the next (19-23). While early methods were unsuited for in-vivo measurements due to practical considerations ranging from time requirements to unfeasibly high RF power depositions, recent methods have proven to be feasible in a clinical setting with suitably short acquisition times (24). Most commonly used B_1^+ mapping methods derive their estimates from a ratio of two acquired T_1 -weighted images. To avoid a dependency of the estimates on T_1 , they either use very long TRs, which lead to long acquisition times, or approximations of the signal equation which are only valid for a limited range of B_1^+ (21).

Correcting DCE-MRI for B_1^+ inhomogeneities is not commonly performed in the clinic, most likely since B_1^+ fields are quite homogeneous at conventional field strengths. Some studies have performed B_1^+ correction at those field strengths and in those cases, the objective was to improve quantification strategies (25-27). Most correction methods perform T_1 measurements of breast tissue prior to contrast injection and correct those for B_1^+ if needed. From there, the T_1 and contrast agent concentration at every time point of the DCE series can be determined (28). Some methods have been proposed to combine measurements of T_1 and B_1^+ prior to contrast injection in order to save scan time (29-31). The influence of B_1^+ on concentration estimates can be severe and corrections have been shown to be beneficial even at 1.5 T and 3 T, where B_1^+ fields are relatively homogeneous (26,27). Correcting for B_1^+ is even more crucial if pharmacokinetic modelling is applied. In a pharmacokinetic model, the rate of contrast agent transfer from the blood vessel into the tumor and vice versa is quantified (32).

1.5 DWI

DWI is a technique that sensitizes the MR signal for the (microscopic) motion of water molecules (33). It achieves this by applying a strong gradient (the same kind we use for position encoding) that reduces the signal and a little while later another equally strong gradient with an opposite effect that increases the signal again. The second gradient will cancel the effect of the first gradient, but not or only partly for spins that moved in the meantime. Consequently, in DWI the signal intensity decreases with increased diffusion.

Since tumors often consist of irregular cell structures, the diffusion of water molecules inside them is slower than that in healthy tissue (34). Therefore, tumors have a higher signal intensity on DWI. Studies have shown that DWI potentially allows differentiation between benign and malignant lesions and prediction of response to neoadjuvant chemotherapy, without the need to inject contrast agents (35,36).

In DWI the MR signal is sensitized for motion to capture diffusion in tissues. However, other kinds of motion are always present in the human body, ranging from body movements to breathing and blood circulation. These kinds of motion are often non-continuous and slow. Since we only want to capture diffusion and no other motion, the

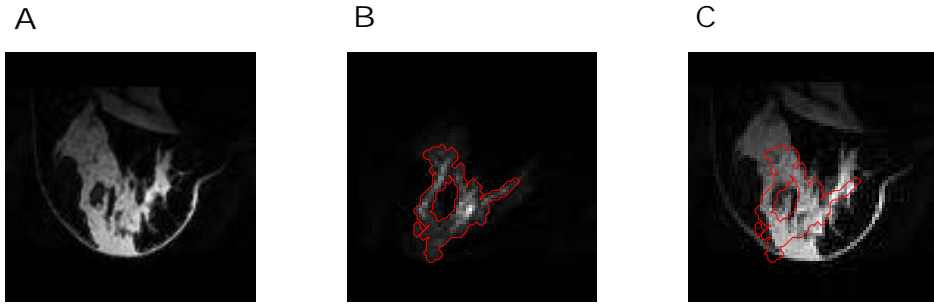


Figure 1.4: A: Breast MRI recorded with a conventional one-line-per-TR readout. B: The same image recorded with an EPI readout. This image is distorted with respect to panel A, even though it is recorded in the same patient on the same location. C: The outline of the distorted EPI image in B superimposed on the non-distorted image in A. Abbreviation: EPI - Echo Planar Imaging.

signal needs to be acquired as fast as possible after motion sensitization. Therefore, while most MRI techniques acquire their images in a line-by-line fashion, in DWI it is common to acquire a complete 2D image in one go. This technique is called echo planar imaging (EPI) (37,38).

The consequence of using EPI is an increased sensitivity to inhomogeneities in the B_0 field. These inhomogeneities cause geometrical distortions to appear in the recorded image. An example of this artifact is shown in Figure 1.4. This effect is similar to what happens to a photo taken through a glass of water or an irregularly shaped glass object. The mechanism behind this effect can be conceptually understood if you think back to how position encoding works in MRI. Since the B_0 field is not equal throughout the breast, the resonance frequency of the spins differs with it. This might mean that a spin on the left side of the breast is resonating with a frequency that is too high. A frequency we associated to a position a few millimeters to the right. Our reconstruction algorithm will wrongly place the signal from that spin a few millimeters to the right, leading to a distorted image. This mismatch increases with increasing differences in B_0 , causing EPI images of the breast to appear more distorted at places where the B_0 field differs strongly from the average.

These inhomogeneities in the B_0 field arise because spins in different tissues in the body respond differently to the main magnetic field of the scanner. This is especially noticeable for spins that are close to transitions between tissues that have different susceptibilities, such as water and fat. These differences in magnetic susceptibility frequently occur in the breast, which contains a lot of water-fat tissue interfaces. Consequently, the B_0 field in the breast at high field is especially irregular.

The earliest papers proposing methods for EPI distortion correction date back to the 90s (39,40). Since then, many refinements to these early methods as well as novel strategies have been proposed. Most prominently, Andersson *et al.* presented a method to correct for B_0 distortions without the need to actually measure the B_0 field (41). Instead, they acquire two EPI's with opposed phase-encoding directions, such that the distortions in both images go in opposite directions, and estimate a smooth B_0

field from there. This method works well for smooth B_0 fields and is one of the two most used strategies today. The alternative approach is to apply deformable image registration to a non-distorted scan, for example the DCE-MRI (42). Though good results have been achieved with this method, there is always a risk of contaminating the corrected DWI image with information from the reference DCE image. For example, contrast differences in the DCE image that are absent in the source EPI may be propagated into the corrected image. Moreover, these techniques may insufficiently correct very local distortions that arise due to steep B_0 gradients at tissue interfaces.

In DWI the diffusion weighting and the direction of this weighting can be chosen. In a typical acquisition, multiple diffusion weightings and directions are acquired. This allows for quantification of the signal decay with increasing diffusion weighting. The measured signal will actually be a mix of signals decaying at different speeds. This is because water molecules in the body are divided over different compartments or water pools ranging from freely diffusing water molecules in e.g. the cerebrospinal fluid, to water molecules in between cells hindered in their diffusion and water molecules inside cells restricted by the cell wall (34). Separation of this mixed signal decay is valuable in tumor characterization and improves tumor visibility as demonstrated for brain tumors (34,43).

Quantification of mixed signal decay using a multi-exponential model can be unstable, especially in the presence of noise (44). A popular approach to circumvent this instability is a two-stage linear approach, often referred to as segmented fitting (45). However, since the segmented method fits the model parameters sequentially instead of iteratively, this method is prone to error propagation. This leads to a bias in parameter estimates (46). More recently, the phasor transform has been proposed as a tool for mixed signal fraction estimation, achieving robust parameter maps (47). After transformation to phasor space, single-exponential curves align on a semi-circle while mixed multi-exponential signals are found on the line connecting their base components (48). This can be used as prior knowledge when fitting a multi-exponential model.

1.6 Thesis Outline

The aim of this thesis is to improve artifact correction and signal quantification in high field breast MRI. In particular, we investigate strategies to correct for B_1^+ inhomogeneities in DCE-MRI and B_0 inhomogeneities in DWI at 7 T. These techniques are investigated in the context of improving the diagnostic power of high field breast MRI.

In **Chapter 2** we propose a method for B_1^+ mapping of the breast at 7 T, which requires no scan time and is essentially noise-free. This is achieved by creating a coil-specific B_1^+ template of the transmit coil and applying this template to each subject, taking into account scaling differences caused by power optimization. We investigate whether the use of this template is justified by comparing B_1^+ distributions within a group of volunteers with a large variation in breast anatomies. The performance of this method is compared against a B_1^+ mapping method.

Chapter 3 investigates correcting measured image intensities in DCE-MRI for B_1^+ inhomogeneities. This is achieved by increasing measured image intensities at relatively

low B_1^+ levels. Doing so will adjust the measured intensities to the correct level, but it will also blow up the noise already present in the image. Therefore we propose a direct mapping from measured image intensities to corrected image intensities that minimizes noise amplification.

In **Chapter 4** we develop a correction technique to correct for the EPI distortion artifact present in DWI. This technique predicts the distortion given a known B_0 field and subsequently compensates for this distortion. Given the irregular nature of the B_0 field inside the breast, the developed correction strategy uses high-resolution B_0 field maps to improve upon existing correction techniques.

Chapter 5 investigates if the phasor transform can aid in achieving more stable quantification of mixed decay signals in DWI. The performance of phasor-aided methods is compared against widespread conventional methods. The influence of sampling strategies and noise are investigated in both digital phantoms and human volunteers.

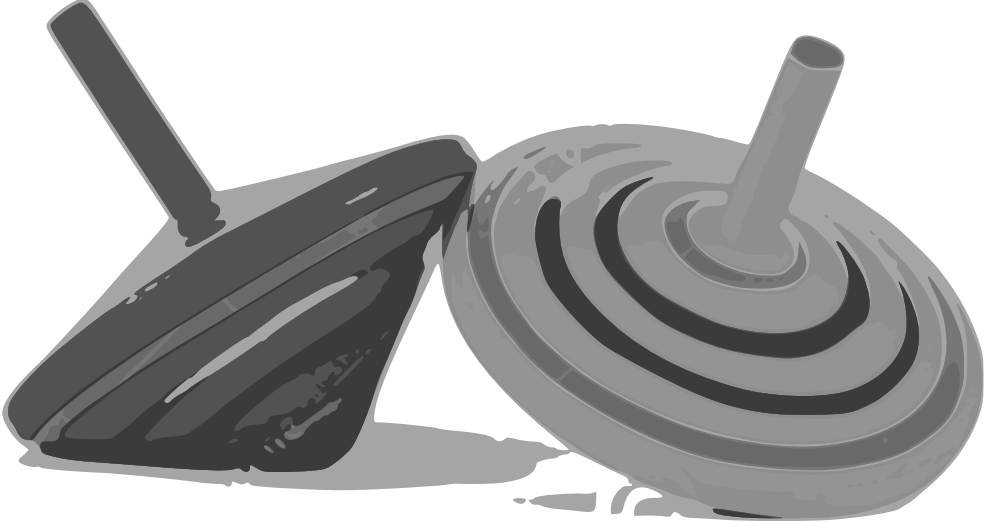
Finally, **Chapter 6** summarizes the results of this thesis and discusses its advances in the context of clinical integration of high field breast MRI.

References

1. Lewis GN, Kasha M. Phosphorescence and the triplet state. *J Am Chem Soc* 1944;66:2100-2116.
2. Brown RW, Cheng Y-CN, Haacke EM, Thompson MR, Venkatesan R. *Magnetic resonance imaging: physical principles and sequence design*: John Wiley & Sons; 2014.
3. American College of Radiology Practice Parameter for the Performance of Contrast-Enhanced Magnetic Resonance Imaging (MRI) of the Breast. Available from: <https://www.acr.org/-/media/ACR/Files/Practice-Parameters/MR-Contrast-Breast.pdf>. Accessed on: May 28, 2019.
4. Berg WA, Gutierrez L, Ness-Aiver MS, Carter WB, Bhargavan M, Lewis RS, Ioffe OB. Diagnostic accuracy of mammography, clinical examination, US, and MR imaging in preoperative assessment of breast cancer. *Radiology* 2004;233(3):830-849.
5. Boetes C, Mus RDM, Holland R, Barentsz JO, Strijk SP, Wobbes T, Hendriks JHCL, Ruys SHJ. Breast-Tumors - Comparative Accuracy of Mr-Imaging Relative to Mammography and Us for Demonstrating Extent. *Radiology* 1995;197(3):743-747.
6. Ladd ME, Bachert P, Meyerspeer M, Moser E, Nagel AM, Norris DG, Schmitter S, Speck O, Straub S, Zaiss M. Pros and cons of ultra-high-field MRI/MRS for human application. *Prog Nucl Mag Res Sp* 2018;109:1-50.
7. Stehouwer BL, Klomp DWJ, van den Bosch MAAJ, Korteweg MA, Gilhuijs KGA, Witkamp AJ, van Diest PJ, Houwert KAF, van der Kemp WJM, Luijten PR, Mali WPTM, Veldhuis WB. Dynamic contrast-enhanced and ultra-high-resolution breast MRI at 7.0 Tesla. *Eur Radiol* 2013;23(11):2961-2968.
8. Pinker K, Bogner W, Baltzer P, Trattng S, Gruber S, Abeyakoon O, Bernathova M, Zaric O, Dubsy P, Bago-Horvath Z, Weber M, Leithner D, Helbich TH. Clinical application of bilateral high temporal and spatial resolution dynamic contrast-enhanced magnetic resonance imaging of the breast at 7 T. *Eur Radiol* 2014;24(4):913-920.
9. Krikken E, Khlebnikov V, Zaiss M, Jibodh RA, van Diest PJ, Luijten PR, Klomp DWJ, Van Laarhoven HWM, Wijnen JP. Amide chemical exchange saturation transfer at 7 T: a possible biomarker for detecting early response to neoadjuvant chemotherapy in breast cancer patients. *Breast Cancer Res* 2018;20.
10. Krikken E, van der Kemp WJM, van Diest PJ, van Dalen T, van Laarhoven HWM, Luijten PR, Klomp DWJ, Wijnen JP. Early detection of changes in phospholipid metabolism during neoadjuvant chemotherapy in breast cancer patients using phosphorus magnetic resonance spectroscopy at 7T. *NMR Biomed* 2019:e4086.
11. Umutlu L, Maderwald S, Kraff O, Theysohn JM, Kuemmel S, Hauth EA, Forsting M, Antoch G, Ladd ME, Quick HH, Lauenstein TC. Dynamic Contrast-Enhanced Breast MRI at 7 Tesla Utilizing a Single-loop Coil: A Feasibility Trial. *Acad Radiol* 2010;17(8):1050-1056.
12. Nagy JA, Chang SH, Shih SC, Dvorak AM, Dvorak HF. Heterogeneity of the Tumor Vasculature. *Semin Thromb Hemost* 2010;36(3):321-331.

13. Hylton N. Dynamic contrast-enhanced magnetic resonance imaging as an imaging biomarker. *J Clin Oncol* 2006;24(20):3293-3298.
14. Kuhl CK, Mielcareck P, Klaschik S, Leutner C, Wardelmann E, Gieseke J, Schild HH. Dynamic breast MR imaging: Are signal intensity time course data useful for differential diagnosis of enhancing lesions? *Radiology* 1999;211(1):101-110.
15. Vaughan TT, Snyder CJ, DelaBarre LJ, Bolan PJ, Tian J, Bolinger L, Adriany G, Andersen P, Strupp J, Ugurbil K. Whole-Body Imaging at 7T: Preliminary Results. *Magn Reson Med* 2009;61(1):244-248.
16. Klomp DWJ, van de Bank BL, Raaijmakers A, Korteweg MA, Possanzini C, Boer VO, van den Berg CAT, van de Bosch MAAJ, Luijten PR. (31)P MRSI and (1)H MRS at 7T: initial results in human breast cancer. *NMR Biomed* 2011;24(10):1337-1342.
17. van der Velden TA, Italiaander M, van der Kemp WJM, Raaijmakers AJE, Schmitz AMT, Luijten PR, Boer VO, Klomp DWJ. Radiofrequency Configuration to Facilitate Bilateral Breast P-31 MR Spectroscopic Imaging and High-Resolution MRI at 7 Tesla. *Magn Reson Med* 2015;74(6):1803-1810.
18. Kuhl CK, Kooijman H, Gieseke J, Schild HH. Effect of B-1 inhomogeneity on breast imaging at 3.0 T. *Radiology* 2007;244(3):929-930.
19. Murphyboesch J, So GJ, James TL. Precision Mapping of the B1 Field Using the Rotating-Frame Experiment. *J Magn Reson* 1987;73(2):293-303.
20. Insko EK, Bolinger L. Mapping of the Radiofrequency Field. *J Magn Reson Ser A* 1993;103(1):82-85.
21. Yarnykh VL. Actual flip-angle imaging in the pulsed steady state: A method for rapid three-dimensional mapping of the transmitted radiofrequency field. *Magn Reson Med* 2007;57(1):192-200.
22. Sacolick LI, Wiesinger F, Hancu I, Vogell MW. B-1 Mapping by Bloch-Siebert Shift. *Magn Reson Med* 2010;63(5):1315-1322.
23. Nehrke K, Börnert P. DREAM - a novel approach for robust, ultrafast, multislice B-1 mapping. *Magn Reson Med* 2012;68(5):1517-1526.
24. Sprinkart AM, Nehrke K, Traber F, Block W, Gieseke J, Schmitz G, Willinek WA, Schild H, Bornert P. Ultrafast Volumetric B-1(+) Mapping for Improved Radiofrequency Shimming in 3 Tesla Body MRI. *J Magn Reson Imaging* 2014;40(4):857-863.
25. Sung KH, Daniel BL, Hargreaves BA. Transmit B-1(+) Field Inhomogeneity and T-1 Estimation Errors in Breast DCE-MRI at 3 Tesla. *J Magn Reson Imaging* 2013;38(2):454-459.
26. Bedair R, Graves MJ, Patterson AJ, McLean MA, Manavaki R, Wallace T, Reid S, Mendichovszky I, Griffiths J, Gilbert FJ. Effect of Radiofrequency Transmit Field Correction on Quantitative Dynamic Contrast-enhanced MR Imaging of the Breast at 3.0 T. *Radiology* 2016;279(2):368-377.
27. Tsai WC, Kao KJ, Chang KM, Hung CF, Yang Q, Lin CE, Chen CM. B1 Field Correction of T1 Estimation Should Be Considered for Breast Dynamic Contrast-enhanced MR Imaging Even at 1.5 T. *Radiology* 2017;282(1):55-62.
28. Haacke EM, Filletti CL, Gattu R, Ciulla C, Al-Bashir A, Suryanarayanan K, Li M, Latif Z, DelProposto Z, Sehgal V, Li T, Torquato V, Kanaparti R, Jiang J, Neelavalli J. New algorithm for quantifying vascular changes in dynamic contrast-enhanced MRI independent of absolute T1 values. *Magn Reson Med* 2007;58(3):463-472.
29. Sung K, Saranathan M, Daniel BL, Hargreaves BA. Simultaneous T-1 and B-1(+) Mapping Using Reference Region Variable Flip Angle Imaging. *Magn Reson Med* 2013;70(4):954-961.
30. van Schie JJN, Lavini C, van Vliet LJ, Vos FM. Feasibility of a fast method for B-1-inhomogeneity correction for FSPGR sequences. *Magn Reson Imaging* 2015;33(3):312-318.
31. Li ZF, Zhao W, Qi TF, Gao C, Gu Q, Zhao JS, Koh TS. A simple B-1 correction method for dynamic contrast-enhanced MRI. *Phys Med Biol* 2018;63(16).
32. Tofts PS, Berkowitz B, Schnall MD. Quantitative-Analysis of Dynamic Gd-Dtpa Enhancement in Breast-Tumors Using a Permeability Model. *Magn Reson Med* 1995;33(4):564-568.
33. Stejskal EO, Tanner JE. Spin Diffusion Measurements: Spin Echoes in the Presence of a Time-Dependent Field Gradient. *J Chem Phys* 1965;42(1):288-+.
34. White NS, McDonald CR, Farid N, Kupernnan J, Karow D, Schenker-Ahmed NM, Bartsch H, Rakow-Penner R, Holland D, Shabaik A, Bjornerud A, Hope T, Hattangadi-Gluth J, Liss M, Parsons JK, Chen CC, Raman S, Margolis D, Reiter RE, Marks L, Kesari S, Mundt AJ, Kaine CJ, Carters BS, Bradley WG, Dale AM. Diffusion-Weighted Imaging in Cancer: Physical Foundations and Applications of Restriction Spectrum Imaging. *Cancer Res* 2014;74(17):4638-4652.
35. Woodhams R, Matsunaga K, Kan S, Hata H, Ozaki M, Iwabuchi K, Kuranami M, Watanabe M, Hayakawa K. ADC mapping of benign and malignant breast tumors. *Magn Reson Med Sci* 2005;4(1):35-42.
36. Sharma U, Danishad KKA, Seenu V, Jagannathan NR. Longitudinal study of the assessment by MRI and diffusion-weighted imaging of tumor response in patients with locally advanced breast cancer undergoing neoadjuvant chemotherapy. *NMR Biomed* 2009;22(1):104-113.

37. Mansfield P. Multi-Planar Image-Formation Using Nmr Spin Echoes. *J Phys C Solid State* 1977;10(3):L55-L58.
38. Rzedzian R, Mansfield P, Doyle M, Guilfoyle D, Chapman B, Coupland RE, Chrispin A, Small P. Real-Time Nuclear Magnetic-Resonance Clinical Imaging in Pediatrics. *Lancet* 1983;2(8362):1281-1282.
39. Bowtell R, McIntyre D, Commandre M, Glover P, Mansfield P. Correction of geometric distortion in echo planar images. *Proc Soc Magn Res* 1994;2:411.
40. Jezzard P, Balaban RS. Correction for Geometric Distortion in Echo-Planar Images from B-0 Field Variations. *Magn Reson Med* 1995;34(1):65-73.
41. Andersson JLR, Skare S, Ashburner J. How to correct susceptibility distortions in spin-echo echo-planar images: application to diffusion tensor imaging. *Neuroimage* 2003;20(2):870-888.
42. Mendez CA, Pizzorni Ferrarese F, Summers P, Petralia G, Menegaz G. DCE-MRI and DWI Integration for Breast Lesions Assessment and Heterogeneity Quantification. *International journal of biomedical imaging* 2012;2012:676808.
43. Hu YC, Yan LF, Wu L, Du P, Chen BY, Wang L, Wang SM, Han Y, Tian Q, Yu Y, Xu TY, Wang W, Cui GB. Intravoxel incoherent motion diffusion-weighted MR imaging of gliomas: efficacy in preoperative grading. *Sci Rep* 2014;4.
44. Lemke A, Stieltjes B, Schad LR, Laun FB. Toward an optimal distribution of b values for intravoxel incoherent motion imaging. *Magn Reson Imaging* 2011;29(6):766-776.
45. Pekar J, Moonen CTW, van Zijl PCM. On the Precision of Diffusion/Perfusion Imaging by Gradient Sensitization. *Magn Reson Med* 1992;23(1):122-129.
46. Cho GY, Moy L, Zhang JL, Baete S, Lattanzi R, Moccaldi M, Babb JS, Kim S, Sodickson DK, Sigmund EE. Comparison of Fitting Methods and b-Value Sampling Strategies for Intravoxel Incoherent Motion in Breast Cancer. *Magn Reson Med* 2015;74(4):1077-1085.
47. Vergeldt FJ, Prusova A, Fereidouni F, van Amerongen H, van As H, Scheenen TWJ, Bader AN. Multi-component quantitative magnetic resonance imaging by phasor representation. *Sci Rep* 2017;7.
48. Clayton AHA, Hanley QS, Verveer PJ. Graphical representation and multicomponent analysis of single-frequency fluorescence lifetime imaging microscopy data. *J Microsc-Oxford* 2004;213:1-5.



Estimating B_1^+ in the breast at 7T using a generic template

Based on:

M.J. van Rijssel, J.P.W. Pluim, P.R. Lijten, K.G.A. Gilhuijs, A.J.E. Raaijmakers, D.W.J. Klomp; Estimating B_1^+ in the breast at 7 T using a generic template, *NMR in Biomedicine* 2018, 31(5):e3911

Abstract

Purpose

Dynamic contrast-enhanced MRI (DCE-MRI) is the workhorse of breast MRI, where the diagnosis of lesions is largely based on the enhancement curve shape. However, this curve shape is biased by radiofrequency transmit (B_1^+) field inhomogeneities. B_1^+ field information is required in order to correct these. The use of a generic, coil-specific B_1^+ template is proposed and tested.

Methods

Finite-difference time-domain simulations for B_1^+ were performed for healthy female volunteers with a wide range in breast anatomies. A generic B_1^+ template was constructed by averaging simulations based on 4 volunteers. Three-dimensional B_1^+ maps were acquired in 15 other volunteers. Root mean square error (RMSE) metrics were calculated between individual simulations and the template, and between individual measurements and the template. The agreement between the proposed template approach and a B_1^+ mapping method was compared against the agreement between acquisition and reacquisition using the same mapping protocol.

Results

RMSE values (in % of nominal flip angle) comparing individual simulations with the template were in the range 2.00-4.01%, with mean 2.68%. RMSE values comparing individual measurements with the template were in the range 8.1-16%, with mean 11.7%. The agreement between the proposed template approach and a B_1^+ mapping method was only slightly worse than the agreement between two consecutive acquisitions using the same mapping protocol in three volunteers: the range of agreement increased from $\pm 16\%$ of the nominal angle for repeated measurement to $\pm 22\%$ for the B_1^+ template.

Conclusion

With local RF transmit coils, intersubject differences in B_1^+ fields of the breast are comparable to the accuracy of B_1^+ mapping methods, even at 7T. Consequently, a single generic B_1^+ template suits subjects over a wide range of breast anatomies, eliminating the need for a time-consuming B_1^+ mapping protocol.

2.1 Introduction

Dynamic contrast-enhanced MRI (DCE-MRI) is the workhorse of clinical breast MRI examinations. Since its introduction in the 1980s, it has become a standard in breast MRI examinations due to its robustness and ability to detect tumor malignancy (1,2). This ability is based on the differences in dynamics of contrast agent uptake between tumors and healthy parenchymal tissue, leading to characteristic enhancement curve shapes. Automated analysis of these curves enabled the introduction of computer aided diagnosis methods into clinical practice, and pharmacokinetic models have been proposed to quantify the exchange of contrast agents between the inflowing blood and surrounding tissue (3-5).

Taking breast DCE-MRI to higher field strengths such as 7T is currently being investigated, showing potential for earlier and more accurate diagnosis (6). The higher signal-to-noise ratio that is available at higher field strengths enables higher spatial resolution. A higher resolution not only permits detection of smaller lesions, it also improves assessment of the heterogeneity of contrast uptake, such as rim enhancement, which is associated with worse survival in triple negative breast cancers (7). It was shown that using the available signal-to-noise ratio to achieve a higher temporal resolution at 7T is also feasible in a clinical setting (8).

A fast wash-out rate is a typical indication of a malignant tumor, while a stable curve or continued wash-in often reflect benign lesions. However, the curve shape can be compromised by radiofrequency transmit (B_1^+) field variations, potentially shifting the curve of a tumor that should have caused a wash-out shape into a more stable curve. This can be conceptually understood by considering the fact that at different B_1^+ levels there is a different amount of T_1 saturation, and the effects of a change in T_1 (due to contrast administration) will differ. If we define B_1^+ induced image intensity bias as: $bias = \frac{\text{measured intensity}}{\text{true intensity}(B_1^+=100\%)}$, then for fast RF spoiled gradient echo sequences: $bias = \frac{\sin(B_1^+ \theta_{nom}) \cdot (1 - e^{-TR/T_1} \cos(\theta_{nom}))}{\sin(\theta_{nom}) \cdot (1 - e^{-TR/T_1} \cos(B_1^+ \theta_{nom}))}$. Observe that this bias not only depends on B_1^+ , but also on T_1 , which in DCE-MRI is not constant in time and the image intensity bias will change over the dynamic series. Generally, for any B_1^+ below 100%, the bias increases with increasing T_1 ; consequently when the T_1 of tumor tissue drops due to contrast injection, the DCE curve's wash-in is reduced due to the counteracting effect of the intensity bias. The opposite effect occurs when due to contrast wash-out the tumor's T_1 rises again, leading to a compromised curve, shifted to appear more stable than the true curve.

Correction for this B_1^+ effect is possible, using B_1^+ field maps and an estimate of T_1 before contrast injection (9). It has been shown that applying B_1^+ correction at 3T has a significant effect on the results of quantitative analysis and serves to reduce differences in quantitative parameter estimations between the right and left breast (10). Recent work shows that even at 1.5 T, refraining from B_1^+ field corrections, leads to a 50% estimation error in tumor T_1 and consequently a 41% estimation error in pharmacokinetic parameters (11). At 7T, the B_1^+ field variations manifest themselves on a smaller spatial scale, such that variations within a single breast become significant. Therefore, when applying DCE-MRI at 7T, corrections using B_1^+ field maps are imperative.

B_1^+ field variations are much more significant on higher field strengths due to the reduced wave length of the radiofrequency (RF) field. At 7T, the proton excitation frequency is 300 MHz, leading to an RF wavelength of around 15 cm inside the body (assuming a relative permittivity around 60). The breasts however, contain high amounts of fat, which has a relative permittivity that is an order of magnitude lower than that of most other tissues. This leads to a longer RF wavelength inside the breasts, approximately 40 cm assuming a relative permittivity around 10. Such a wavelength is usually larger than the size of the imaged anatomy. In that case, the B_1^+ field distribution within the breast will mainly depend on the local transmit setup used, and hardly on the individual anatomy. Therefore we hypothesize that one generic, coil-specific B_1^+ template suits a wide range of subjects in the case of breast examinations with local transmit coils. We set out to test our hypothesis at 7T, where local transmit is a commonly used strategy to overcome RF inhomogeneity issues.

The advantages of using a generic B_1^+ template in a clinical setting are twofold. It eliminates the need to acquire a B_1^+ field map, saving scan time. Furthermore, B_1^+ mapping techniques are known to be prone to noise and many are only reliable within a certain range (12,13). Since the generic template is based on (partly simulated) data of multiple subjects, it is essentially noise-free and reliable in the full range of B_1^+ inhomogeneities present. Though other techniques to estimate B_1^+ in breast without acquiring field maps exist, these methods often rely on fat as a reference tissue (with a fixed T_1) in order to estimate B_1^+ in the parenchyma (14,15). Such methods may not be suitable for fat-suppressed sequences and rely on extrapolation of a fitted field distribution outside fatty regions. The template method presented is not hampered by these limitations since B_1^+ distributions can be deduced regardless of the sequence used. This method is limited only by the availability of a B_1^+ template of the used coil design.

The present work aims to explore the feasibility of using a generic B_1^+ template by investigating the inter-subject differences in B_1^+ inhomogeneity. The work comprises both simulated field maps and measured ones, in order to compare template performance to the accuracy of B_1^+ mapping.

2.2 Methods

In order to test our hypothesis that one generic, coil-specific B_1^+ template suits a wide range of subjects when performing breast MRI with local transmit coils, a number of experiments were performed. First, RF simulations from previous work were used to create the template (Section 2.2.1). Next, B_1^+ and T_1 mapping was performed on 15 new volunteers (Section 2.2.2) and their breast volume and composition were estimated (Section 2.2.3). Section 2.2.4 describes Q-measurements of the coil we conducted to investigate the influence of breast anatomy on coil loading. The acquired B_1^+ maps were used to compare against the predictions made using the constructed template (Section 2.2.5). Finally, we tested the ability of the B_1^+ template predictions to correct T_1 maps for B_1^+ inhomogeneity corruption against B_1^+ map corrected T_1 measurements (Section 2.2.6), using methodology that is common in quantitative DCE-MRI.

All experiments conducted were in accordance with the guidelines of the local ethical committee and, prior to the exam, written informed consent was obtained from all vol-

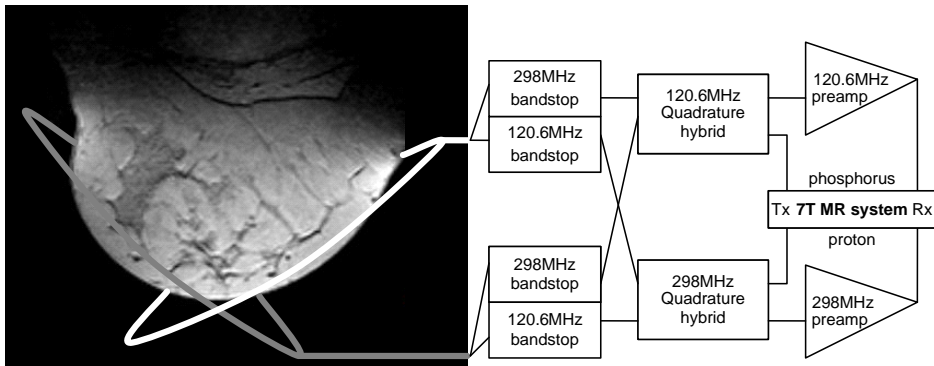


Figure 2.1: Schematic overview of the dual-channel unilateral breast coil for the detection of ^{31}P and ^1H MR signals. The location of the two elements is illustrated by two ellipsoids on a transverse MR image of the human breast. These elements are interfaced to the transmit (Tx) and receive (Rx) line of the 7T MR system using bandstop filters, quadrature hybrids and preamplifiers as illustrated on the right. Reproduced from (16).

unteers.

2.2.1 Simulations and template construction

The coil setup used in this work was a quadrature setup illustrated in Figure 2.1 and presented in earlier work by Klomp *et al.* (16). Their work also demonstrates the high efficiency of this coil and its usefulness in imaging and spectroscopy applications for 7T breast MRI.

Finite difference time domain simulations of B_1^+ and B_1^- distributions in five healthy female volunteers (V1-V5), presented in previous work, were used to investigate inter-subject differences in B_1^+ distribution when using this local transmit coil setup at 7T (17). In short, B_1 field distributions were calculated from personalized breast segmentations obtained from T_1w Dixon scans fused with Virtual Family model E1a, and a 3D model of the relevant MR equipment (18,19). Segmentations of glandular tissue, adipose tissue and skin were assigned their corresponding dielectric permittivity and conductivity values (20). Finite difference time domain simulations were conducted for 201.000 time steps of 3×10^{-12} s (1 Larmor period) with a mesh of $2 \times 2 \times 2$ mm³, assuming perfectly absorbing boundary layers. Convergence was assessed by visual inspection. Coil losses weren't considered, since these have no impact on B_1^+ distributions. Vitamin tablets were attached to the coil elements using adhesive tape, in order to identify their position in the T_1w scans. Though a limited number of volunteers was used to conduct the simulations, volunteers were selected to represent a reasonably wide range in breast anatomies, as can be appreciated from their T_1w gradient echo scans in Figure 2.2 and anatomical characteristics in Table 2.1. Due to missing data, the simulation for V1 had to be excluded.

In order to directly compare the simulated B_1^+ and B_1^- fields, that did not share a common coordinate system, all simulated field distributions were aligned using multi-resolution intensity-based rigid registration in elastix (21). For this purpose, a mutual information

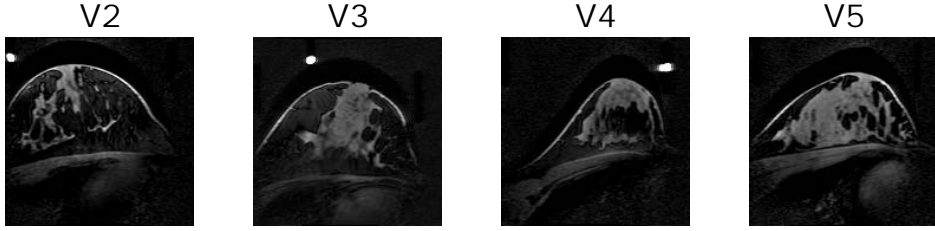


Figure 2.2: Fat-suppressed T_1w scans of the four included simulation volunteers (sagittal view). Bright dots mark the location of vitamin tablets used to determine the position of the coil by Van der Velden *et al.* (17).

Table 2.1: Inclusion table reporting the breast volume and volumetric glandular percentage for all simulation volunteers (V2-V5).

Subject	Breast volume (cm ³)	Gland percentage
V2	756	17%
V3	777	29%
V4	285	33%
V5	474	44%
Mean	573	31%
SD	205	9%
Min	285	17%
Max	777	44%

similarity metric, third order B-spline interpolation and an Adaptive Stochastic Gradient Descent optimizer were used. This allows transmit coil alignment, since these coils are present in the simulations as hyperintense fields closest to the coil conductors. Differences in RF amplification settings between volunteers were overcome by normalizing all simulations relative to the simulation of V5 (arbitrarily chosen). In order to do so, the following intensity scaling factor was applied to the simulated field distribution for volunteers V2-V5:

$$Scale(i) = \text{median} \left\{ \forall \vec{r} : \frac{Simulation_5(\vec{r})}{Simulation_i(\vec{r})} \right\} \quad (2.1)$$

where i is the volunteer number and $\vec{r} = (x, y, z)$ the position in the simulation. Note that the use of the median was preferred over the mean to ensure robustness against outliers.

Subsequently the average of the rescaled simulation distributions of volunteer V2-V5 was taken, we denote these the B_1^+ and B_1^- templates. Differences between volunteers were assessed per volunteer by comparing each individual simulation result with the B_1^+ template. The comparison was quantified using mean difference, standard deviation (SD) of difference and root mean square error (RMSE) metrics. All metrics were calculated over all voxels within the breast region-of-interest, which was determined previously (17). The B_1^- template was created to facilitate B_1^+ template scaling using information obtained from the power optimization phase.

2.2.2 Scanning protocol

In order to prospectively compare the accuracy of the template approach to B_1^+ mapping, a validation set of fifteen additional healthy female volunteers (S1-S15), mean age 39 years (range 24–62, all ages are reported in Table 2.2), were scanned in prone position using the same unilateral breast coil setup on a 7T whole-body MR system (Achieva; Philips, Cleveland, Ohio, USA) (16). A 3D B_1^+ map was acquired using the dual refocusing echo acquisition mode (DREAM) technique with the following parameters: pulse repetition time 4.0 ms, stimulated echo time 1.49 ms, free induction decay echo time 1.97 ms, 2.5 mm isotropic resolution, preparation angle 55°, imaging angle 25°, and turbo field echo factor 32 (12). For three volunteers, S13-S15, the DREAM B_1^+ acquisition was repeated, to compare the accuracy of the proposed template method with the variation between repeated measures. 3D T_1 weighted gradient echo images were acquired at four flip angles (2°, 4°, 13° and 27°) using Dixon water-fat separation with parameters: in-phase echo time 1.97 ms, out-phase echo time 4.4 ms, repetition time 6.0 ms, and 1.5 mm isotropic resolution (19). Both scans were planned according to a fast survey scan, measurements obtained during this scan's power optimization phase were logged and later used in template scaling. Scan parameters for both sequences are summarized in Table 2.3. The B_1^+ map and variable flip angle images allowed the calculation of T_1 maps using the driven-equilibrium single-pulse observation of T_1 relaxation (DESPOT1) technique (22); see Section 2.2.6 for more details and the rationale behind the choice of angles.

2.2.3 Estimating breast volume and composition

For all volunteers estimates of breast volume and composition were calculated. Since the pectoral muscle was not visible for all volunteers due to the limited range where the coil transmits and receives sufficient signal, estimates of breast volume were obtained using the method described by Katariya *et al.* (23) on transversal maximum intensity projections. Though this method is rather simplistic and potentially imprecise, it has been shown to be highly reproducible, correlated with mastectomy excision volume and allows for comparison with published population data (24,25). The Dixon water and fat reconstructions were used to estimate volumetric gland percentage for each volunteer.

2.2.4 Q factor measurements

In order to check individual differences of coil loading, all volunteers (S1-S15) were asked to return on a different day to perform additional Q factor measurements. Out of 15, 9 volunteers were able to participate and in 1 volunteer the measurement failed, leading to 8 useable data points. Measurements were performed using a purpose-built coil that contained a replica of the innermost element of the coil that was used in the MR experiments. The mechanics of the setup were identical to the setup used in the scanner. The Q factor (defined as central resonance frequency over bandwidth) was determined using a network analyzer. Volunteers were asked to lie down in prone position on the setup as they did in the scanner, positioning the arms on their back. Values for Q both with and without loading were recorded for each volunteer, the ratio $Q_{unloaded}/Q_{loaded}$ was calculated as a measure for coil loading. The ratios were plotted against breast volume and volumetric glandular percentage for each volunteer, a trend line was calculated using analytical ordinary least squares estimation.

Table 2.2: Inclusion table reporting the age, breast volume, volumetric glandular percentage and the ratio $Q_{\text{unloaded}}/Q_{\text{loaded}}$ for all validation volunteers (S1-S15).

Subject	Age (years)	Breast volume (cm ³)	Gland percentage	$Q_{\text{unloaded}} /$ Q_{loaded}
S1	24	495	28%	-
S2	26	479	28%	3.2
S3	24	638	64%	5.2
S4	25	382	26%	3.7
S5	30	309	25%	3.7
S6	33	213	38%	3.9
S7	57	184	17%	3.0
S8	62	570	10%	-
S9	45	1032	7.2%	-
S10	55	235	24%	2.8
S11	53	928	7.5%	4.5
S12	40	707	41%	-
S13	28	129	87%	-
S14	24	351	81%	-
S15	28	494	35%	-
Mean	36.9	476	35%	3.7
SD	13.4	256	25%	0.74
Min	24	129	7.2%	2.8
Max	62	1032	87%	5.2

2.2.5 Comparing B_1^+ template and measured maps

Rigid registration was applied to the B_1^+ template to facilitate direct comparison with the measured B_1^+ map for every volunteer. The map was masked before registration to exclude regions where a B_1^+ reconstruction was not available. The template was masked by thresholding to exclude values corresponding to flip angles below 20% and above 100% of the nominal flip angle. All values higher than 100% are very close to or in coil elements, the bottom cut-off of 20% was empirically chosen to avoid registration of the edge of the map to the edge of the template. In the resulting binary image, a 3D connected components algorithm using a 6-connected neighborhood was used to find connected regions. The largest connected component was selected as the mask. Multi-resolution intensity-based rigid registration was applied in elastix, using a mutual information similarity metric, B-spline interpolation and an Adaptive Stochastic Gradient Descent optimizer.

Subsequently, the B_1^+ values of the registered template were intensity scaled using information from the scanner's power optimization phase. During this phase, a global B_1^+ level (PO B_1^+) for the sample is measured. Using scanner log data from the power

Table 2.3: Summary of scan parameters per sequence. Abbreviations: DREAM - Dual Refocusing Echo Acquisition Mode, 3D - three-dimensional acquisition, RF - radiofrequency, TR - repetition time, TE - echo time, SE - Spin Echo, FID - Free Induction Decay, IP - In Phase, OP - Opposite Phase, TFE - Turbo Field Echo.

	DREAM B_1^+ map	Dual-echo gradient echo (4x)	Survey (3D, fast RF-spoiled gradient echo)
TR (ms)	4	6	6
TE (ms)	SE: 1.49 FID: 1.97	IP: 1.97 OP: 4.4	1.25
Resolution (mm ³)	2.5x2.5x2.5	1.5x1.5x1.5	3x3x10
Flip angle (°)	Preparation: 55 Imaging: 25	2 / 4 / 13 / 27	10
Other parameters	TFE acceleration factor: 32	Dixon water & fat images	Reconstructed to 2x2x5 mm ³

optimization phase for all volunteers, a calibration line was determined between this global PO B_1^+ and an average B_1^+ value determined from the registered template, scaled to match the measured B_1^+ map (i.e. the best possible template scale for every volunteer). Taking into account the global nature of the PO B_1^+ , the average B_1^+ value was weighted with both B_1^+ and B_1^- : $weighted |B_1^+| = \frac{\sum_{r \in M} ((B_1^-(r) \cdot B_1^+(r)) B_1^+(r))}{\sum_{r \in M} (B_1^-(r) \cdot B_1^+(r))}$, where M is a mask created by thresholding the survey scan using Otsu's method (26). The calibration line obtained in this fashion was subsequently used to scale each registered B_1^+ template, independently of their measured B_1^+ map.

The map and the registered template were compared on individual bases through calculation of the RMSE, mean error and SD of the error per volunteer and a total mean absolute error for the validation set. Additionally, a Bland-Altman density plot was created, showing the agreement between the measured B_1^+ map and the registered and scaled template for all fifteen volunteers (S1-S15). As suggested by Bland & Altman, the same kind of plot was created for two repeated DREAM-based B_1^+ mapping measurements to study repeatability (27). This allowed for comparison of the limits of agreement between the template method and the DREAM method with the degree of variation between repeated B_1^+ mapping procedures for volunteers S13-S15.

2.2.6 T_1 mapping

As is commonly done in quantitative DCE-MRI, we used B_1^+ maps to correct for the effects of B_1^+ inhomogeneities using a variable flip-angle T_1 mapping method (10,11,22,28,29). This method uses several T_1 -weighted gradient echo scans at different flip angles to estimate the T_1 value at every recorded voxel by performing a fit of the signal equation, which is a function of the applied flip angle. Since this is a voxel-wise method, B_1^+ correction can be easily applied by fitting the function while using the

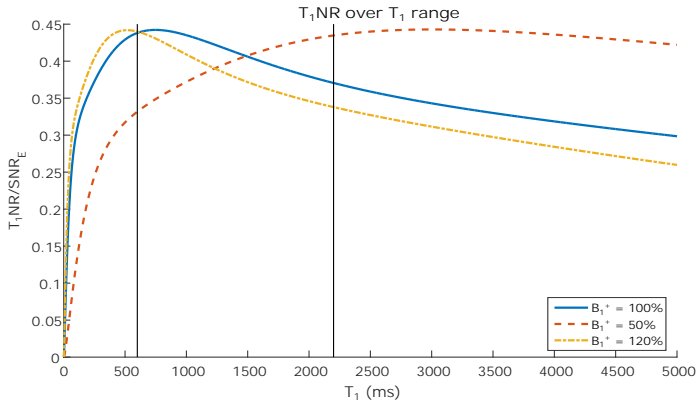


Figure 2.3: T_1 -to-noise ratio (T_1 NR) of the variable-flip-angle acquisition scheme, when using the DESPOT1 analysis method. Profiles for T_1 -to-noise are plotted for three levels of B_1^+ ; vertical lines indicate the T_1 for glandular tissue (2200 ms) and fat (600 ms).

actual flip angle as the independent variable, i.e. the nominal angle multiplied by the value in the B_1^+ map for that voxel.

The flip-angle combination was chosen by taking into consideration the notions put forth by Deoni *et al.* (30), ensuring an accurate T_1 measurement over the wide B_1^+ range (50 – 120% of the nominal angle) and the wide T_1 range (600 – 2200 ms) present in the breast. To determine the best flip-angle combination, all combinations of four integer angles in the range 1 - 90° were tested and the T_1 -to-noise-ratio (T_1 NR) was calculated for every combination of angles with T_1 set to either 600 or 2200 ms and B_1^+ set to either 50% or 120% of the nominal angle. The sum over all four combinations of B_1^+ and T_1 for T_1 NR determined the suitability of every combination of angles. Figure 2.3 shows the T_1 NR using the selected flip angle combination (2°, 4°, 13° and 27°) over a wide range of T_1 values for three levels of B_1^+ .

T_1 maps were calculated from the data using the DESPOT1 method (22). In the fitting procedure, the independent variable was either the nominal angle, the angle as measured by the DREAM sequence or the angle as predicted by the template. This leads to T_1 maps that are not corrected for B_1^+ , corrected by the DREAM B_1^+ data or corrected by the generic B_1^+ template respectively. The SD of the T_1 estimate was calculated in every voxel, following the methodology described in (30). An estimate of the noise level was obtained by taking the SD of the image intensity in anatomy-free regions of the gradient echo images. Finally, all voxels for which the SD in the T_1 estimate was larger than 100 ms were (empirically) considered unreliable and excluded (the average exclusion percentage was 10.3% of all voxels inside the region where the DREAM B_1^+ map was defined).

The obtained T_1 maps were analyzed by comparing the measurements corrected using the measured map vs using the template. The T_1 estimates were compared on individual bases through calculation of the RMSE, mean error and SD of the error.

Table 2.4: Comparison between individual B_1^+ simulations and the generic template for all simulation volunteers (V2-V5). Abbreviation: % ona - percentage of nominal angle.

Subject	Mean error (% ona)	SD of error (% ona)	RMSE (% ona)
V2	0.87	3.92	4.01
V3	0.80	2.24	2.38
V4	-1.42	1.85	2.34
V5	0.35	1.97	2.00
Mean	0.15	2.50	2.68
SD	0.93	0.83	0.78
Min	-1.42	1.85	2.00
Max	0.87	3.92	4.01

2.3 Results

Table 2.1 shows the breast volume and volumetric glandular percentage of all simulation volunteers; Table 2.2 shows the same for all validation volunteers. In the simulation set, breast volume ranged from 285 to 777 cm³, glandular percentage from 17 to 44%; in the validation set, breast volume ranged from 129 to 1032 cm³, glandular percentage from 7 to 87%.

The difference between the constructed generic template and every individual volunteer's simulation is shown in Figure 2.4. Panel B shows that the differences between individuals are small particularly compared to the large dynamic range in B_1^+ in each individual. As Table 2.4 shows, the mean RMSE between the generic template and individual simulations was 2.68% of the nominal angle, while in the worst agreeing volunteer (V2) this was 4.01%.

Measurements for $Q_{unloaded}/Q_{loaded}$ ranged from 2.8 to 5.2. Measurements per volunteer are reported in Table 2.2.

The calibration line used in power optimization-based scaling of the template is shown in Figure 2.5. The calibration line fit had an adjusted R^2 of 0.825. The (registered and scaled) generic template and the measured B_1^+ map are similar, as can be appreciated visually from Figure 2.6. It shows both the best matching case (S6) and the worst matching case (S11), based on the RMSE. Table 2.5 shows statistics for all volunteers (S1-S15). The mean RMSE between the generic template and individual prospective measurements was 11.7% of the nominal angle, the total mean absolute error was 5.37%. The Bland-Altman analysis of all volunteers in Figure 2.7, panel A shows that in regions with low B_1^+ the measured maps and generic template agree less than areas with high B_1^+ . Panel B shows the same analysis for a subset, only data from volunteers S13-S15 has been included. Panel C shows a Bland-Altman of repeated DREAM B_1^+ mapping for the same volunteers (S13-S15), note that the limits of agreement in panel B are 12% wider than in panel C.

T_1 estimates calculated with DESPOT1 and either map-based or template-based B_1^+ information are close, as can be appreciated visually in Figure 2.8 for volunteer S1. Table

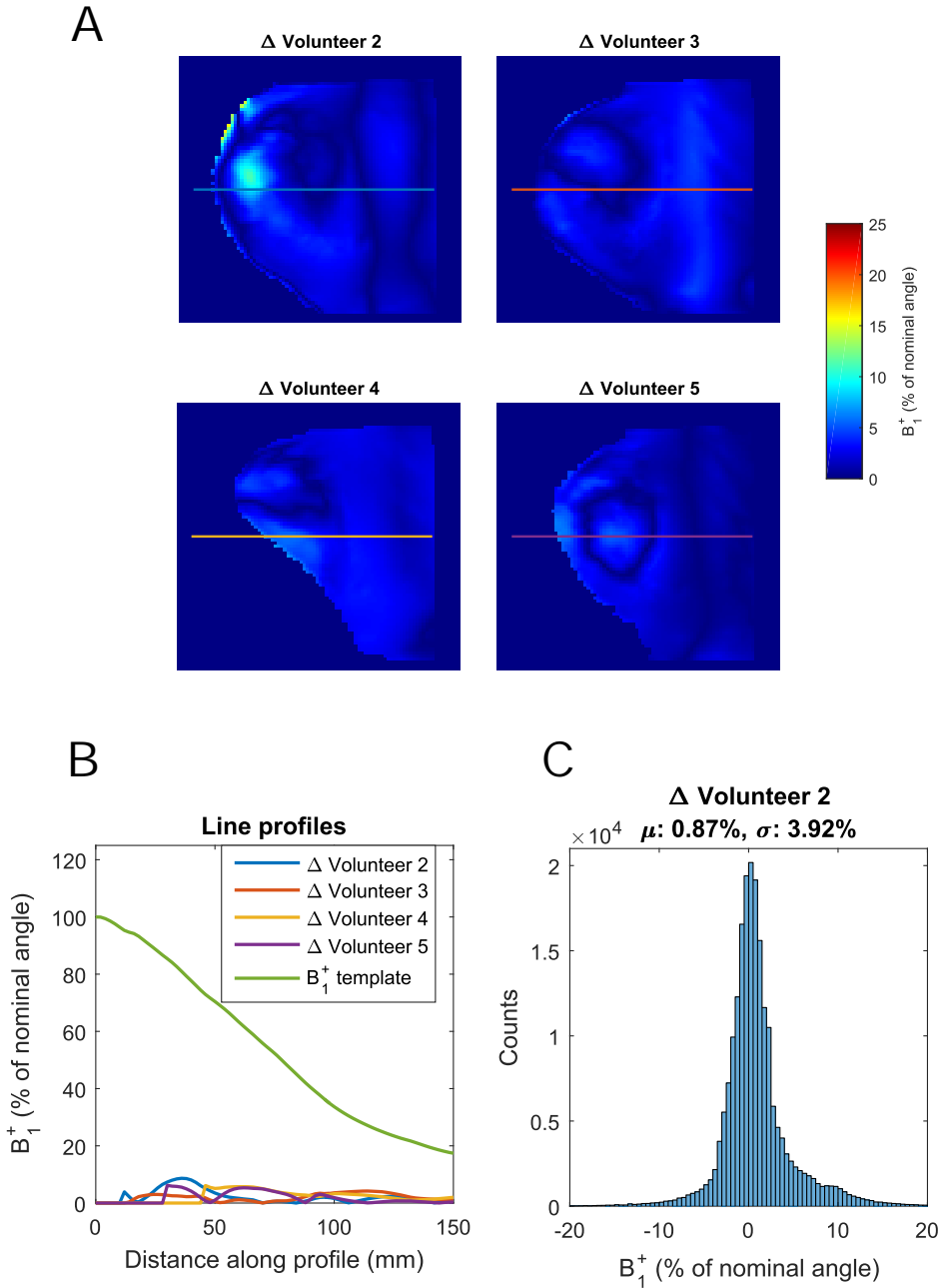


Figure 2.4: A: Absolute difference between mean B_1^+ (template) and individual simulations. B: Line profiles corresponding to same-colored lines in A. C: Histogram of difference between template and simulation of volunteer 2 (which showed least agreement).

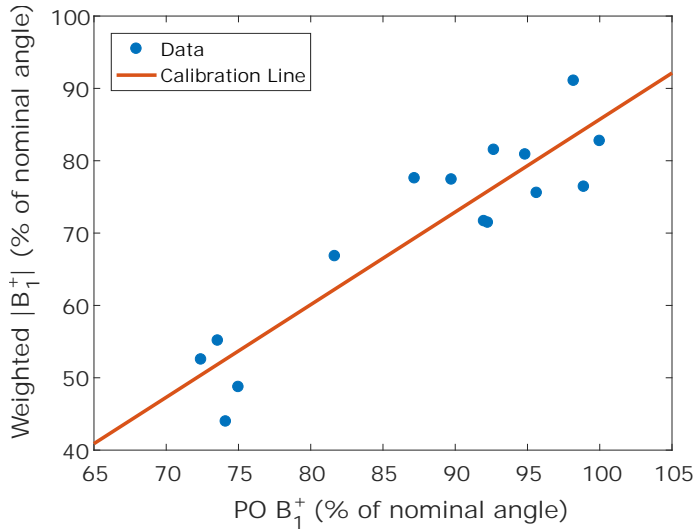


Figure 2.5: Calibration line for B_1^+ template scaling. The global B_1^+ measured during the scanners power optimization phase is regressed against a weighted average of the B_1^+ template, scaled to match the measured B_1^+ map. Adjusted R^2 of the fit is 0.825. Abbreviation: PO - Power Optimization.

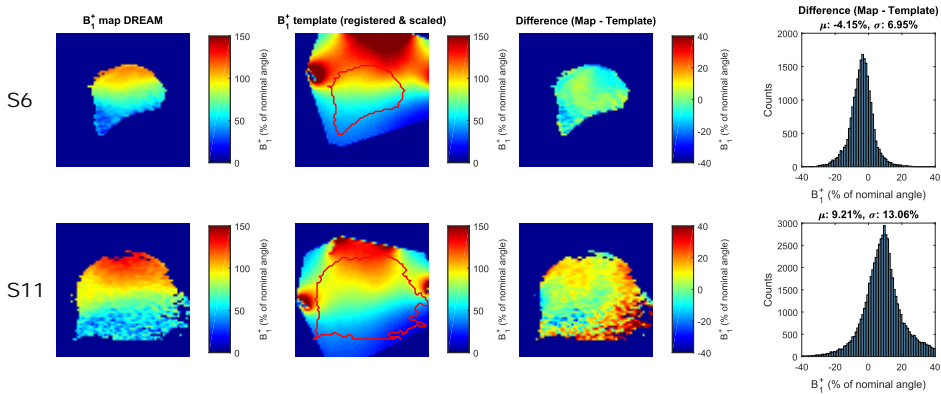


Figure 2.6: For volunteer S6(top row) and volunteer S11(bottom row), from left to right: B_1^+ map measured with DREAM technique; B_1^+ template registered and scaled to measured map, red line indicates breast outline as in first panel; Difference between template and map; Histogram of difference between template and map. Abbreviation: DREAM - Dual Refocusing Echo Acquisition Mode.

Table 2.5: Comparison between individual B_1^+ measurements and the generic template for all validation volunteers (S1-S15). Abbreviation: % ona - percentage of nominal angle.

Subject	Mean error (% ona)	SD of error (% ona)	RMSE (% ona)
S1	-1.9	11	11
S2	7.9	9.4	12
S3	-0.93	12	12
S4	4.9	8.3	9.6
S5	3.9	7.5	8.4
S6	-4.2	7.0	8.1
S7	-6.3	8.4	10
S8	3.0	10	10
S9	5.6	12	14
S10	2.2	9.0	9.3
S11	9.2	13	16
S12	8.8	12	15
S13	-10	11	15
S14	-5.5	11	13
S15	-6.1	11	12
Mean	0.710	10.2	11.7
SD	5.96	1.85	2.34
Min	-10	7.0	8.1
Max	9.2	13	16

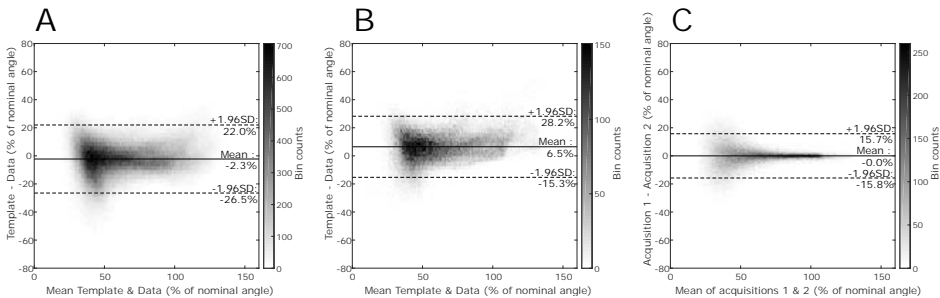


Figure 2.7: A: Bland-Altman analysis of the registered templates and measured maps for all volunteers (S1-S15). The data is visualized using a density histogram, the scale bar on the right indicates the amount of counts in each bin. B: Bland-Altman analysis of a subset of the data displayed in A, only volunteers S13-S15 are shown. C: Bland-Altman analysis of repeated measured B_1^+ maps of volunteers S13-S15.

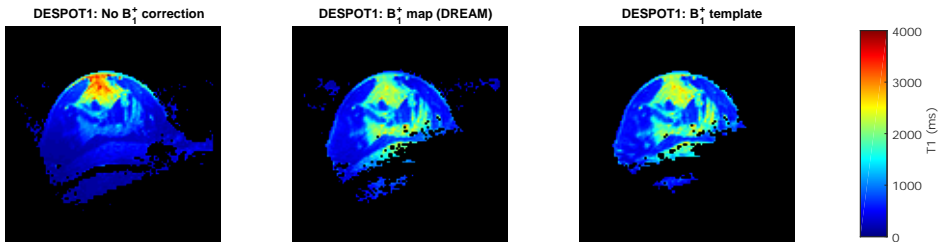


Figure 2.8: For volunteer S1, from left to right: T_1 map using DESPOT1 and no B_1^+ correction; T_1 map using DESPOT1 and B_1^+ map measured with DREAM; T_1 map using DESPOT1 and B_1^+ template registered and scaled to measured map. Abbreviations: DESPOT1 - Driven-Equilibrium Single-Pulse Observation of T_1 relaxation, DREAM - Dual Refocusing Echo Acquisition Mode.

2.6 shows a quantitative analysis for all volunteers (S1-S15), the mean RMSE was 318 ms.

2.4 Discussion

Our results from the simulations show that differences in B_1^+ distributions in the breast between volunteers covering a wide anatomical range are generally very small, only in the order of 2-3%. This amount of variation is of the same order of magnitude as the accuracy of popular B_1^+ mapping methods (31). This is a strong indication that in breast MRI with local RF transmit coils at 7T or lower, resorting to field mapping for every subject is unnecessary.

The width of the anatomical range of the validation set, quantified in Table 2.2, is substantial, both in terms of breast volume and glandular percentage. Comparing our distribution of breast volumes to that of 225 healthy women in (24), shows that we have captured a wide range, except for the high end of the spectrum since the maximum included volume is only one standard deviation away from the reported average; sadly our coil setup and non-wide bore MR system are incapable of accommodating women with higher breast volumes. The included range of breast densities is also broad when compared to a representative group of 531 consecutively included patients receiving breast MRI; the largest reported volumetric glandular percentage is 50% in (32). Note that Gubern-Mérida *et al.* showed that volumetric estimations of breast density based on MRI tend to underestimate BI-RADS (Breast Imaging Reporting and Data System) density scores and that in their study of 132 women from a high-risk group with comparable age characteristics to our study, none of the subjects had a percentage higher than 60% (33). The width of the simulation set is inevitably smaller, due to the small number of four included volunteers. Yet it captures a reasonably wide range (at least one standard deviation from the average for both breast density and volume) and, arguably, our results obtained with only the limited simulation set make the case for a template-based B_1^+ estimation only stronger.

Our results from the measured B_1^+ maps show that a generic template can accommodate volunteers over a wide range of breast anatomies. The Bland-Altman analysis in Figure 2.7A makes clear that the measured maps are interchangeable with the registered and scaled generic template, within the range between the limits of agreement

Table 2.6: Comparison between the DREAM-corrected and template-corrected measurements of T_1 (ms) for all validation volunteers (S1-S15). Abbreviation: DREAM - Dual Refocusing Echo Acquisition Mode.

Subject	Mean error (ms)	SD of error (ms)	RMSE (ms)
S1	-54	171	180
S2	213	255	332
S3	-80	231	244
S4	160	215	268
S5	146	295	329
S6	-144	201	248
S7	-232	261	349
S8	-47	225	230
S9	-66	184	196
S10	-23	286	287
S11	-110	165	199
S12	-181	353	397
S13	-586	359	687
S14	300	400	500
S15	187	272	331
Mean	-34	258	318
SD	213	68	128
Min	-586	165	180
Max	300	400	687

(-26.5% - +22.0% of the nominal angle). In other words, if one is satisfied with an error between the two methods up to approximately 20% of the nominal angle, the methods may be exchanged. Note that the range of agreement is considerably narrower (and thus better) if one were to exclude regions where B_1^+ is low, where the measured maps are unreliable (12). In those regions, the generic template might actually be at an advantage, since it does not suffer from such a limitation and is noise-free in nature. To investigate whether the observed limits of agreement between the proposed template method and the DREAM method are acceptable, Figure 2.7B and 2.7C show the results for three volunteers (S13-S15) of an identical Bland-Altman analysis between measured data and proposed template (2.7B) and between measured data and repeated measurement (2.7C) respectively. The range between the limits of agreement is slightly larger for the template than for repeated measurements: where repeated measurements had an error of up to 15% of the nominal angle for volunteers S13-S15, this range increased with approximately 6% using a B_1^+ template. The bias that can be observed in Figure 2.7B is mainly due to the use of the calibration line for template scaling, and this bias will differ for each volunteer. Note from Table 2.5 that volunteers S13-S15 all have quite large mean errors, which explains the high mean offset (bias) in Figure 2.7B; for most subjects, this bias will be smaller.

It is clear from Figure 2.8 that the B_1^+ corrected DESPOT1-based T_1 maps are substantially more homogeneous in both lipids and glandular tissue, irrespective of whether the B_1^+ information comes from a map or the template. When comparing the analyses in Table 2.5 and Table 2.6 it is clear that the mean errors in B_1^+ propagate into mean errors in T_1 estimates. In all cases but one, the standard deviation of the error distribution is bigger than the mean error, which means that the two measurements of T_1 do not significantly differ.

A limitation of this study is the fact that we have to rely on RF simulations to be able to construct the template. Several studies, however, have shown that these kinds of simulations are able to accurately predict B_1^+ distributions and show high agreement between measured and simulated field maps (34-37). The fact that all simulations were performed using a single body model with different breast models may further impact the validity of our simulations, though since local transmit coils were used, the effect will be limited to an increase or decrease of the total efficiency. If this effect is present, it will be corrected by the intensity scaling of the registered template (Section 2.2.5). The results of the Q measurements also contribute to this conclusion. While they show that tissue load is dominant ($Q_{unloaded}/Q_{loaded}$ was around 4 for all volunteers), they also show that even with breast volume changes up to a factor 5, load variations were all within 30% of $Q_{unloaded}/Q_{loaded} = 4$. This means that the biggest tissue load is caused by the rest of the body and that the Q variance with over breast anatomies is limited, analogous to our results in B_1^+ . Probably, the RF eddy currents that occur in the rest of the body may predominantly have a local B_1^+ effect that is either of insufficient strength to effect the B_1^+ in the breast, or hardly differs from the effects observed in the Virtual Family model (EIIa).

Though this chapter only demonstrates the use of a template for a unilateral breast coil, we believe this can be extended to bilateral cases. Hardware developments in high-field MRI tend to go towards parallel multi-transmit systems where amplitude and phase of all coil elements can be steered individually. In such setups, regarding each breast independently in terms of B_1^+ is a reasonable assumption.

It is of note that demonstrating agreement between measured and simulated B_1^+ distributions is often used to validate predictions in specific absorption rate (SAR). While our work shows that B_1^+ distributions in the breast are very similar from person to person, the same does not necessarily hold for SAR. In fact, in recent work by Alon *et al.*, it was demonstrated that B_1^+ distributions tend to be correlated over samples, but the same did not hold for SAR (38). Therefore, they conclude that using B_1^+ distributions to validate SAR predictions should be done with caution. The present work serves as further proof to the statement that B_1^+ distributions tend to have high correlations between subjects; this is the very phenomenon we exploit when constructing and using a B_1^+ template.

Implementation of the generic template approach in a clinical setting requires knowledge on both the position of the transmit coil in the image and the amount of template scaling that is needed for each subject. In many setups, the position of the coil is fixed on the bed, eliminating the positioning problem altogether. We have solved the scaling issue by using readily available information from the power optimization phase and

the survey scan, information that will be present in any clinical protocol. This strategy brings a dependence of the template's performance on the goodness of fit of the calibration line of Figure 2.5: a large variation from the calibration line causes a large mean error (bias) in the resulting template-based B_1^+ distribution. As reported in Table 2.5, the standard deviation of the mean error was 5.96% of the nominal angle; in the ideal situation where the scaling is calculated directly from a measured B_1^+ map, this standard deviation reduces to 1.78% of the nominal angle. The main reason for the reduced performance (and the goodness of fit of the calibration line) might be that the B_1^+ measured during the power optimization procedure is non-localized. Therefore, it was assumed that the measured B_1^+ level during the power optimization was a weighted average over the entire imaged region that contained tissue. The differences in mean error between volunteers may be further reduced when a localized power optimization method is employed for template scaling (39).

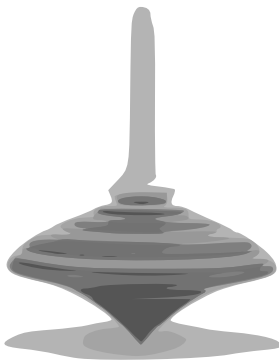
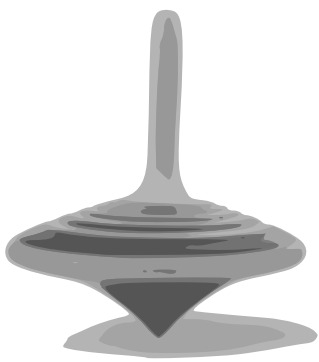
In conclusion, simulations show that inter-subject differences in B_1^+ fields of the breast at 7T are comparable to the accuracy of popular B_1^+ mapping methods reported in literature. Consequently, we have shown that, at the cost of a small loss in accuracy (the range of agreement increased from $\pm 16\%$ of the nominal angle for repeated measurement to $\pm 22\%$ for the B_1^+ template), using a generic B_1^+ template to account for substantial RF transmit inhomogeneity in T_1 mapping may be feasible across a wide range of volunteers.

References

1. Kaiser WA, Zeidler E. MR Imaging of the Breast - Fast Imaging Sequences with and without Gd-Dtpa - Preliminary-Observations. *Radiology* 1989;170(3):681-686.
2. Morris EA. Breast cancer imaging with MRI. *Radiol Clin North Am* 2002;40(3):443-466.
3. Chen WJ, Giger ML, Bick U, Newstead GM. Automatic identification and classification of characteristic kinetic curves of breast lesions on DCE-MRI. *Med Phys* 2006;33(8):2878-2887.
4. Gilhuijs KGA, Giger ML, Bick U. Computerized analysis of breast lesions in three dimensions using dynamic magnetic-resonance imaging. *Med Phys* 1998;25(9):1647-1654.
5. Tofts PS, Berkowitz B, Schnall MD. Quantitative-Analysis of Dynamic Gd-Dtpa Enhancement in Breast-Tumors Using a Permeability Model. *Magn Reson Med* 1995;33(4):564-568.
6. Stehouwer BL, Klomp DWJ, van den Bosch MAAJ, Korteweg MA, Gilhuijs KGA, Witkamp AJ, van Diest PJ, Houwert KAF, van der Kemp WJM, Luijten PR, Mali WPTM, Veldhuis WB. Dynamic contrast-enhanced and ultra-high-resolution breast MRI at 7.0 Tesla. *Eur Radiol* 2013;23(11):2961-2968.
7. Schmitz AMT, Loo CE, Wesseling J, Pijnappel RM, Gilhuijs KGA. Association between rim enhancement of breast cancer on dynamic contrast-enhanced MRI and patient outcome: impact of subtype. *Breast Cancer Res Treat* 2014;148(3):541-551.
8. Pinker K, Bogner W, Baltzer P, Trattng S, Gruber S, Abeyakoon O, Bernathova M, Zaric O, Dubsky P, Bago-Horvath Z, Weber M, Leithner D, Helbich TH. Clinical application of bilateral high temporal and spatial resolution dynamic contrast-enhanced magnetic resonance imaging of the breast at 7 T. *Eur Radiol* 2014;24(4):913-920.
9. Haacke EM, Filletti CL, Gattu R, Ciulla C, Al-Bashir A, Suryanarayanan K, Li M, Latif Z, DelProposto Z, Sehgal V, Li T, Torquato V, Kanaparti R, Jiang J, Neelavalli J. New algorithm for quantifying vascular changes in dynamic contrast-enhanced MRI independent of absolute T1 values. *Magn Reson Med* 2007;58(3):463-472.
10. Bedair R, Graves MJ, Patterson AJ, McLean MA, Manavaki R, Wallace T, Reid S, Mendichovszky I, Griffiths J, Gilbert FJ. Effect of Radiofrequency Transmit Field Correction on Quantitative Dynamic Contrast-enhanced MR Imaging of the Breast at 3.0 T. *Radiology* 2016;279(2):368-377.
11. Tsai W-C, Kao K-J, Chang K-M, Hung C-F, Yang Q, Lin C-YE, Chen C-M. B1 Field Correction of T1 Estimation Should Be Considered for Breast Dynamic Contrast-enhanced MR Imaging Even at 1.5 T. *Radiology*;0(0):160062.

12. Nehrke K, Börnert P. DREAM - a novel approach for robust, ultrafast, multislice B-1 mapping. *Magn Reson Med* 2012;68(5):1517-1526.
13. Yarnykh VL. Actual flip-angle imaging in the pulsed steady state: A method for rapid three-dimensional mapping of the transmitted radiofrequency field. *Magn Reson Med* 2007;57(1):192-200.
14. Pineda FD, Medved M, Fan XB, Karczmar GS. B-1 and T-1 Mapping of the Breast with a Reference Tissue Method. *Magn Reson Med* 2016;75(4):1565-1573.
15. Sung K, Saranathan M, Daniel BL, Hargreaves BA. Simultaneous T-1 and B-1(+) Mapping Using Reference Region Variable Flip Angle Imaging. *Magn Reson Med* 2013;70(4):954-961.
16. Klomp DWJ, van de Bank BL, Raaijmakers A, Korteweg MA, Possanzini C, Boer VO, van den Berg CAT, van de Bosch MAAJ, Luijten PR. (31)P MRSI and (1)H MRS at 7T: initial results in human breast cancer. *NMR Biomed* 2011;24(10):1337-1342.
17. van der Velden TA, Italiaander M, van der Kemp WJM, Raaijmakers AJE, Schmitz AMT, Luijten PR, Boer VO, Klomp DWJ. Radiofrequency configuration to facilitate bilateral breast 31P MR spectroscopic imaging and high-resolution MRI at 7 Tesla. *Magn Reson Med* 2015;74(6):1803-1810.
18. Christ A, Kainz W, Hahn EG, Honegger K, Zefferer M, Neufeld E, Rascher W, Janka R, Bautz W, Chen J, Kiefer B, Schmitt P, Hollenbach HP, Shen JX, Oberle M, Szczerba D, Kam A, Guag JW, Kuster N. The Virtual Family-development of surface-based anatomical models of two adults and two children for dosimetric simulations. *Phys Med Biol* 2010;55(2):N23-N38.
19. Dixon WT. Simple Proton Spectroscopic Imaging. *Radiology* 1984;153(1):189-194.
20. Gabriel C, Gabriel S, Corthout E. The dielectric properties of biological tissues: 1. Literature survey. *Phys Med Biol* 1996;41(11):2231-2249.
21. Klein S, Staring M, Murphy K, Viergever MA, Pluim JPW. elastix: A Toolbox for Intensity-Based Medical Image Registration. *IEEE Trans Med Imaging* 2010;29(1):196-205.
22. Deoni SCL, Rutt BK, Peters TM. Rapid combined T-1 and T-2 mapping using gradient recalled acquisition in the steady state. *Magn Reson Med* 2003;49(3):515-526.
23. Katariya RN, Forrest APM, Gravelle IH. Breast Volumes in Cancer of Breast. *Br J Cancer* 1974;29(3):270-273.
24. Scutt D, Manning JT, Whitehouse GH, Leinster SJ, Massey CP. The relationship between breast asymmetry, breast size and the occurrence of breast cancer. *Br J Radiol* 1997;70(838):1017-1021.
25. Senie RT, Rosen PP, Lesser ML, Snyder RE, Schottenfeld D, Duthie K. Epidemiology of Breast-Carcinoma II: Factors Related to the Predominance of Left-Sided Disease. *Cancer* 1980;46(7):1705-1713.
26. Otsu N. A threshold selection method from gray-level histograms. *IEEE transactions on systems, man, and cybernetics* 1979;9(1):62-66.
27. Bland JM, Altman DG. Statistical Methods for Assessing Agreement between Two Methods of Clinical Measurement. *Lancet* 1986;1(8476):307-310.
28. Christensen KA, Grant DM, Schulman EM, Walling C. Optimal Determination of Relaxation-Times of Fourier-Transform Nuclear Magnetic-Resonance - Determination of Spin-Lattice Relaxation-Times in Chemically Polarized Species. *J Phys Chem* 1974;78(19):1971-1977.
29. Homer J, Beevers MS. Driven-Equilibrium Single-Pulse Observation of T1 Relaxation - a Reevaluation of a Rapid New Method for Determining NMR Spin-Lattice Relaxation-Times. *J Magn Reson* 1985;63(2):287-297.
30. Deoni SCL, Peters TM, Rutt BK. Determination of optimal angles for variable nutation proton magnetic spin-lattice, T-1, and spin-spin, T-2, relaxation times measurement. *Magn Reson Med* 2004;51(1):194-199.
31. Nehrke K, Sprinkart AM, Börnert P. An in vivo comparison of the DREAM sequence with current RF shim technology. *Magn Reson Mater Phy* 2015;28(2):185-194.
32. van der Velden BHM, Dmitriev I, Loo CE, Pijnappel RM, Gilhuijs KGA. Association between Parenchymal Enhancement of the Contralateral Breast in Dynamic Contrast-enhanced MR Imaging and Outcome of Patients with Unilateral Invasive Breast Cancer. *Radiology* 2015;276(3):675-685.
33. Gubern-Merida A, Kallenberg M, Platel B, Mann RM, Marti R, Karssemeijer N. Volumetric Breast Density Estimation from Full-Field Digital Mammograms: A Validation Study. *PLoS One* 2014;9(1).
34. Graesslin I, Homann H, Biederer S, Bornert P, Nehrke K, Vernickel P, Mens G, Harvey P, Katscher U. A specific absorption rate prediction concept for parallel transmission MR. *Magn Reson Med* 2012;68(5):1664-1674.
35. Homann H, Bornert P, Eggers H, Nehrke K, Dossel O, Graesslin I. Toward Individualized SAR Models and In Vivo Validation. *Magn Reson Med* 2011;66(6):1767-1776.
36. Murbach M, Neufeld E, Capstick M, Kainz W, Brunner DO, Samaras T, Pruessmann KP, Kuster N. Thermal tissue damage model analyzed for different whole-body SAR and scan durations for standard MR body coils. *Magn Reson Med* 2014;71(1):421-431.

37. Voigt T, Homann H, Katscher U, Doessel O. Patient-individual local SAR determination: in vivo measurements and numerical validation. *Magn Reson Med* 2012;68(4):1117-1126.
38. Alon L, Deniz CM, Carluccio G, Brown R, Sodickson DK, Collins CM. Effects of Anatomical Differences on Electromagnetic Fields, SAR, and Temperature Change. *Concepts in magnetic resonance Part B, Magnetic resonance engineering* 2016;46(1):8-18.
39. Versluis MJ, Kan HE, van Buchem MA, Webb AG. Improved Signal to Noise in Proton Spectroscopy of the Human Calf Muscle at 7 T Using Localized B1 Calibration. *Magn Reson Med* 2010;63(1):207-211.



Correcting time-intensity curves in dynamic contrast-enhanced breast MRI for inhomogeneous excitation fields



Based on:

M.J. van Rijssel, J.P.W. Pluim, H.M. Chan, L. van den Wildenberg, A.M.Th. Schmitz, P.R. Lijten, K.G.A. Gilhuijs, D.W.J. Klomp; Correcting time-intensity curves in dynamic contrast-enhanced breast MRI for inhomogeneous excitation fields, *submitted*

Abstract

Purpose

Inhomogeneous excitation at ultrahigh field strengths (7 T and above) compromises the reliability of quantified dynamic contrast-enhanced breast MRI. This can hamper the introduction of ultrahigh field MRI into the clinic. Compensation for this non-uniformity effect can consist of both hardware improvements and post-acquisition corrections. This chapter investigates the correctable radiofrequency transmit (B_1^+) range post-acquisition in both simulations and patient data for 7T MRI.

Methods

Simulations are conducted to determine the minimum B_1^+ level at which corrections are still beneficial due to noise amplification. Two correction strategies leading to differences in noise amplification are tested. The effect of the corrections on a 7 T patient dataset (N=38) with a wide range of B_1^+ levels is investigated in terms of time-intensity curve types as well as washin, washout and peak enhancement values.

Results

In simulations, the lowest B_1^+ level at which the signal-to-noise ratio of the corrected images was at least that of the original precontrast image was 43% of the nominal angle. After correction, time-intensity curve types changed in 24% of included patients and the distribution of curve types corresponded better to the distribution found in literature. Additionally, the overlap between the distributions of washin, washout and peak enhancement values for grade 1 and grade 2 tumors was reduced.

Conclusion

Post-acquisition correction for inhomogeneous excitation is feasible down to B_1^+ levels of 43% of the nominal angle, if accurate B_1^+ maps are available. Correcting DCE-MRI for B_1^+ non-uniformity might increase the performance of grade prediction models.

3.1 Introduction

The most used sequence in breast MRI is dynamic contrast-enhanced MRI (DCE-MRI). It has a high diagnostic power due to its ability to detect abnormalities and to differentiate malignant from benign lesions (1,2). To a great extent, its diagnostic power is based on differences in dynamics of contrast agent uptake. These differences in contrast agent uptake have led to the characterization of time-intensity curves (TICs) into three categories: type I curves, which show steady enhancement; type II curves, which show a plateau; or type III curves, which show a washout (3).

Currently, breast MR examinations are routinely performed at field strengths up to 3 T. Efforts are underway to enable breast MRI at ultrahigh field strengths, most notably 7 T. Advantages of performing MR at ultrahigh field strengths include a higher signal-to-noise ratio (SNR) and a higher chemical shift (4). The first advantage can be used to increase spatial resolution, which has been shown to be feasible in a clinical setting and might have potential for earlier and better diagnosis (5,6). Additionally, a better spatial resolution enables the assessment of tumor heterogeneity (7). The second advantage can be used to measure tumor metabolism using spectroscopy techniques. Measurements of this kind may be able to predict the response to neoadjuvant therapy in an early stage of treatment (8,9). A multiparametric analysis combining phosphorous spectroscopy with DCE-MRI achieves a better agreement with postoperative findings than the conventional preoperative workup (10).

A major factor hampering the clinical acceptance of ultrahigh field breast MRI in the clinic is the fact that time-intensity curves acquired during DCE-MRI acquisitions may be unreliable due to radiofrequency transmit (B_1^+) inhomogeneities (11,12). The unreliability of TICs in DCE-MRI is caused by B_1^+ field inhomogeneities, which increase with increasing field strengths (4). A lower B_1^+ level means that spins experience a lower RF excitation angle and consequently a lower amount of T_1 saturation is applied. For DCE-MRI, this means that a decrease in B_1^+ level causes a decrease in sensitivity to changes in T_1 and ultimately a flattening of TICs, as illustrated in Figure 3.1.

The most obvious solution may be to tackle the problem at the source: improve the homogeneity of the B_1^+ field. In recent years, progress has been made in the field of radiofrequency coil design towards that end (13,14). However, a completely homogeneous B_1^+ field is nontrivial to achieve even with state-of-the-art hardware, so some amount of field inhomogeneity is always expected. This is illustrated by recent works showing that corrections for B_1^+ can be beneficial even at 1.5 T and 3 T (15,16).

DCE scans can be corrected for inhomogeneous B_1^+ effects post-acquisition if the B_1^+ field distribution is known. Haacke *et al.* described an approach to quantify T_1 at every time point in a DCE time series that allows straightforward incorporation of B_1^+ field maps to calculate unbiased estimates of T_1 (17). From these estimates, synthetic MR images corrected for B_1^+ can be generated. However, since this method is based on the ratio of each postcontrast image with the precontrast image, the resulting SNR is limited by the low SNR of the precontrast image. We investigate a simplification of this two-step approach to limit the amount of noise amplification in the corrected images.

Even though B_1^+ corrections post-acquisition are possible, the correctable range will be

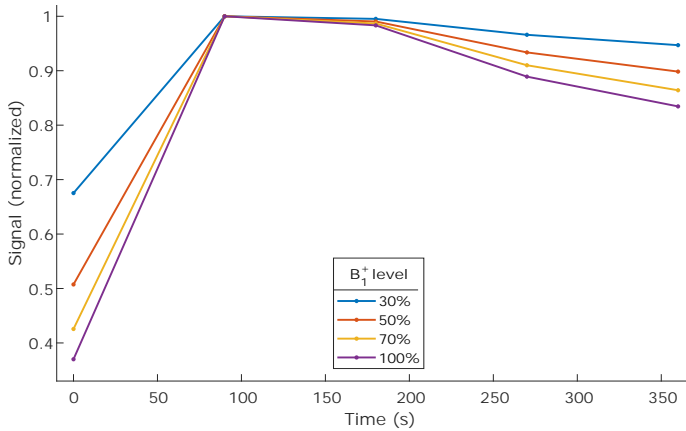


Figure 3.1: Influence of B_1^+ on time-intensity curves in DCE-MRI. Low B_1^+ induces a type II plateau curve, even in tumors that should show a type III washout curve. Each curve has been normalized to its own maximum for clarity. Abbreviation: DCE-MRI - Dynamic Contrast-Enhanced Magnetic Resonance Imaging.

limited by the absolute amount of signal that is generated at the actual flip angle. Figure 3.2A shows the amount of signal generated for a range of flip angles by an enhancing tumor, assuming a spoiled gradient echo imaging sequence with a TR of 5.8 ms (as was used in this study) and enhancing signal from tumor tissue with a T_1 of 400 ms. If an imaging angle above the Ernst angle is used, e.g. 15° as in this study, there will be a lower angle that generates the same amount of signal, in this example that is 6.3° . Thus, one might think that the range of B_1^+ at which correction is still possible extends at least as far as $6.3/15 = 42\%$ of the nominal angle. However, a decrease in flip angle not only induces a change in signal intensity, it also means a decrease in T_1 sensitivity. Figure 3.2B shows the change in signal induced by a change in T_1 . Even though at an imaging angle of 6.3° the amount of generated signal is equivalent, the sensitivity of the signal to changes in T_1 is only 41.8% of the sensitivity at the nominal angle. This decrease in sensitivity to changes in T_1 , and ultimately to changes in contrast uptake, will further limit the correctable B_1^+ range.

This chapter will investigate the B_1^+ range in which DCE-MRI is still correctable post-acquisition. This will ultimately dictate the degree of homogeneity of the B_1^+ field that coil designers need to achieve. This study will include both simulations and patient data obtained at 7 T, which were acquired with a large variation in B_1^+ levels. Furthermore, we will look at the effect of correction on the patient data with respect to individual time-intensity curves and curve types, as well as to imaging features and grade prediction.

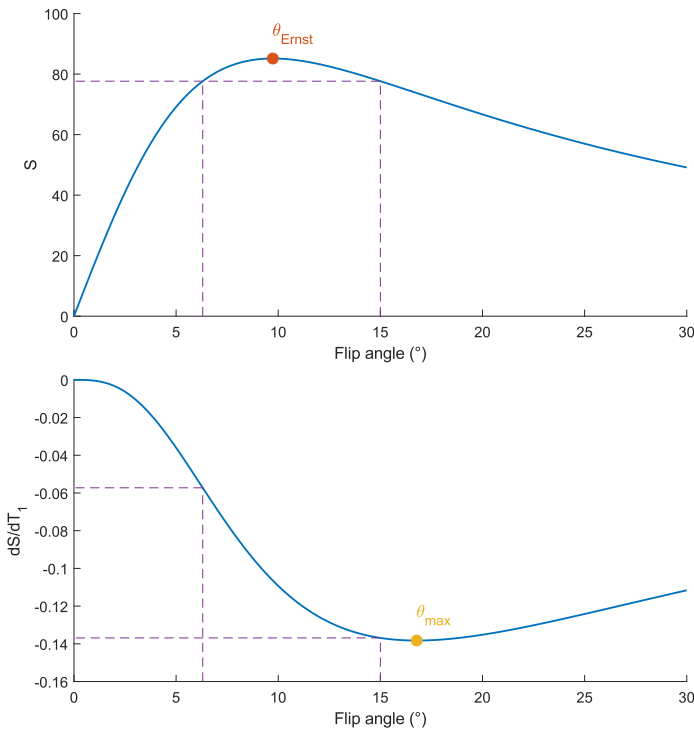


Figure 3.2: A: Signal intensity (S) versus flip angle. In case of a nominal imaging angle above the Ernst angle (θ_{Ernst}), a lower flip angle can be found that produces the same signal intensity, the equivalent angle. The range between the nominal angle and the equivalent angle determines the B_1^+ buffer in terms of signal loss. B: Derivative of the signal intensity with respect to T_1 versus flip angle. The sensitivity to T_1 changes decreases rapidly for low flip angles. This limits the correctable B_1^+ range further.

3.2 Methods

3.2.1 Correction strategies

The measured signal in DCE MRI can be described using the signal equation for spoiled gradient echo acquisitions:

$$S(\theta) = \rho \frac{\sin(\theta)(1 - e^{-TR/T_1})}{1 - \cos(\theta)e^{-TR/T_1}} \quad (3.1)$$

where S is the MR signal, θ is the flip angle, ρ is the proton density weighted with the sensitivity of the MR system's receive chain, TR is the repetition time and T_1 is the longitudinal relaxation time.

Two correction strategies were implemented in MATLAB (R2017b, Natick, MA). The first strategy was based on the T_1 quantification method of Haacke *et al.* (17). Using this method, a T_1 value at every time point was calculated using B_1^+ information and assuming a fixed T_1 of glandular tissue. For all patients in the dataset, a fixed precontrast T_1 value was assumed as proposed by Haacke *et al.* The value that was used was 2100 ms, which corresponds to the average of a previously measured group of healthy volunteers (18). Subsequently, synthetic MR images were calculated using the calculated

T_1 maps, the protocol TR, nominal flip angle and an estimated ρ -map. The ρ -map was estimated using the precontrast image, by inverting the signal equation (Equation 3.1).

The method of Haacke *et al.* was devised to achieve quantification of contrast enhancement in DCE-MRI. This quantification is achieved by measuring the ratio of the signal intensity at every time point with respect to the precontrast signal intensity, at which the T_1 is known or assumed. This ratio image can only be reliably calculated if all post-contrast images align well with the precontrast image. Moreover, the SNR of the resulting images is limited by the SNR of the noisiest image in the DCE series, usually the precontrast image. Since the goal of the current study is not to quantify the contrast enhancement, but to correct for B_1^+ inhomogeneity, a more direct approach was devised. This approach circumvents the calculation of the ratio with respect to the precontrast image and skips the T_1 quantification step.

The proposed method aims to achieve a direct mapping from the measured signal intensities to the true, or corrected, signal intensities. Such a mapping can be achieved analytically, starting with the signal equation for spoiled gradient echo acquisitions as described by Equation 3.1. The measured signal at any B_1^+ level is then given by $S(f\theta_{nom})$, with f the B_1^+ fraction and θ_{nom} the nominal flip angle. Therefore, the relationship between measured and true signal intensities can be described using the following system of equations:

$$\begin{cases} M = S(f\theta_{nom}) \\ T = S(\theta_{nom}) \end{cases} \quad (3.2)$$

where M is the measured signal at B_1^+ level f and T is the true signal at a B_1^+ level of 100%. The system in Equation 3.2 can be solved for the true signal T , which gives a direct mapping from measured signal intensities to true signal intensities:

$$T(M, f) = \frac{M \rho \sin(\theta_{nom})(\cos(f\theta_{nom}) - 1)}{M(\cos(f\theta_{nom}) - \cos(\theta_{nom})) + \rho \sin(f\theta_{nom})(\cos(\theta_{nom}) - 1)} \quad (3.3)$$

Figure 3.3 shows a plot of this direct signal intensity mapping for several levels of B_1^+ .

Note that the direct signal intensity mapping of Equation 3.3 still depends on ρ . In the Haacke-based correction strategy, a ρ -map was estimated using the precontrast image, by inverting the signal equation (Equation 3.1). In order to avoid introducing a ρ -map as another source of noise into our correction strategy, we use assume value for the entire scan. Although this is a simplification, the direct mapping of Equation 3.3 still preserves proton density contrast from the measured image in the corrected image. In most cases, the average estimated ρ in the tumor was used. However, there is a theoretical maximum signal intensity, which is given by $S_{max} = \rho \sin(f\theta_{nom})$. To avoid the highly noncontinuous behavior of Equation 3.3 that occurs for high values of M (see the inset of Figure 3.3), scans that measured a signal intensity higher than this theoretical maximum were treated differently. For these scans, a heuristic approach was taken: the minimum ρ required to explain the highest measured signal in the tumor was used instead of the average ρ in the tumor.

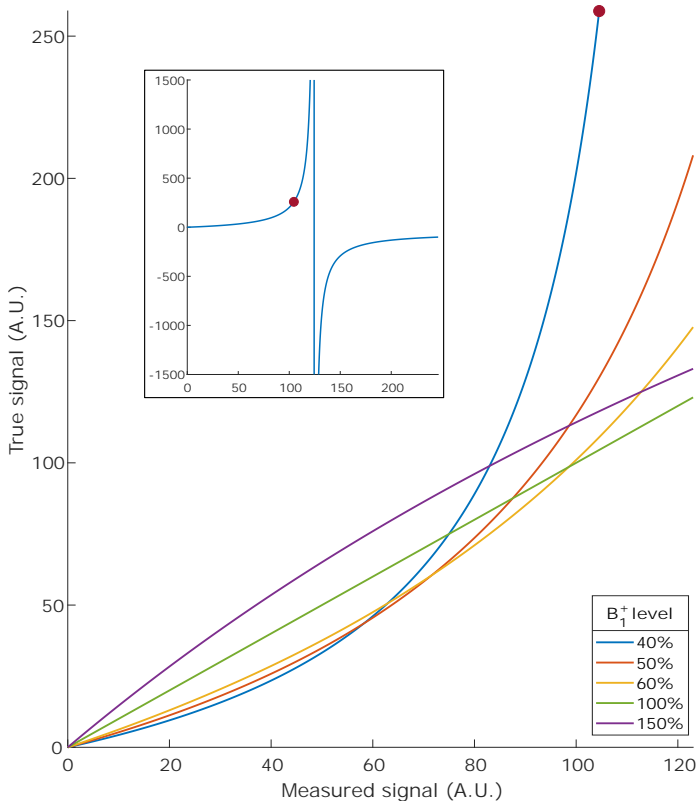


Figure 3.3: True vs measured image intensity at different B_1^+ levels. This direct mapping is the basis of the proposed correction mechanism. The inset shows the nonlinear behavior of this mechanism for measured image intensity levels higher than the theoretical maximum: the blue curve shows the mapping from measured signals to corrected signals for a B_1^+ level of 40% and the red dot indicates the theoretical maximum signal. Abbreviation: A.U. - Arbitrary Units.

3.2.2 Simulations

In order to investigate the amount of noise amplification of both the Haacke-based and the proposed direct correction method, a time-intensity curve was simulated at 100 B_1^+ levels ranging from 1% to 100% of the nominal angle with 1% increments. Gaussian noise was added to the signal such that the SNR was 20, where SNR is defined as average over standard deviation in the precontrast image. Each curve was simulated 3375 times for different noise instances. In order to investigate at which B_1^+ level the curves no longer benefit from correction due to noise amplification, the SNR and standard deviation of the simulated and corrected curves were calculated per time point, as well as the RMSE between the curves and the ground truth. These values were compared to the RMSE and SNR of the uncorrected simulation, such that the resulting minimum B_1^+ level is independent of the chosen SNR in the simulations.

Table 3.1: Overview of the number of included and excluded patients enrolled in the study. Exclusion reasons are indicated in italic. Abbreviation: DCE - Dynamic Contrast Enhanced (MRI).

Patients enrolled in study	55
Patients included in DCE correction	38
Patients not included in DCE correction	17
<i>Patient withdrew from study</i>	1
<i>(imaging not performed)</i>	
<i>DCE acquisition failure</i>	3
<i>B_1^+ map not performed</i>	1
<i>Insufficient power to generate B_1^+ map</i>	9
<i>on one or both sides</i>	
<i>DCE imaging artifact (fat excitation)</i>	1
<i>Tumor segmentation failure</i>	2

3.2.3 Patient data

Data from a previous trial, the Patient Risk Based on Functional MRI (PROFILE) trial, was used in this work (19). This trial included women with histologically proven invasive carcinoma of the breast, eligible for breast conserving surgery based on conventional imaging. This trial ran for 26 months between January 2013 and February 2015. Included patients were scanned using a 7 T MRI whole body scanner (Philips Healthcare, Cleveland, OH). Patients were scanned using a bilateral local transmit coil, either in a transceive configuration or with a dedicated 26-channel receive setup (14). A comprehensive multiparametric protocol was performed, including DCE-MRI and B_1^+ mapping. DCE-MRI with one precontrast and five postcontrast images was acquired using a three-dimensional spoiled gradient echo sequence with either TR 4.3 ms, TE 2.1 ms, flip angle 15°, and 1x1x1 mm³ resolution in 108 seconds per dynamic in case of the transceive setup, or TR 5.8 ms, TE 2.5 ms, flip angle 15°, 0.7x0.7x0.7 mm³ resolution, and SENSE 4x2 (left-right x feet-head) acceleration in 91 seconds per dynamic in case of the 26-channel receive setup (20). Binomial pulses in a 1-3-3-1 configuration were used to achieve water-selective excitation (21). B_1^+ maps for five coronal slices covering only part of the breast were acquired using the actual flip-angle imaging (AFI) method with TR1 50 ms, TR2 250 ms, TE 1.97 ms, flip angle 40°, and 5x5x5 mm³ resolution in 44 seconds (22).

Out of 55 patients available from the PROFILE trial, 38 were included in the DCE correction. DCE correction on the patient data was only performed using the proposed direct method, since the simulations showed that it outperformed the Haacke-based method. Reasons for exclusion of patients are outlined in Table 3.1; the most common reason was insufficient power to generate a B_1^+ map on one or both sides. The 38 included patients had a mean age of 61 years (range: 43 – 74). Based on the surgical specimens, 10 patients had a grade 1 carcinoma, 22 had a grade 2, 3 had a grade 3. Of three patients the grade could not be assessed post-surgery, because they had received neo-adjuvant chemotherapy (NAC).

Deformable image registration was performed in elastix v4.9 to correct for patient motion between DCE time points (23,24). The normalized mutual information similarity metric using 32 histogram bins was optimized with standard gradient descent (1000 iterations, 4096 randomly sampled voxels) (25). A multi-scale approach was used with three resolution levels. The b-spline transformation in the final resolution had a grid size of 15 mm.

In order to eliminate scaling differences between different subjects, histogram normalization was applied to all DCE scans. All intensity values were divided by the estimated noise level of the scan. The noise level was estimated by subtracting a 3x3x3 box-filtered precontrast image from the original precontrast image and subsequently determining the standard deviation in a glandular tissue mask. This glandular tissue mask was obtained by taking all voxels above the Otsu threshold of the original (fat-suppressed) precontrast image.

Even though B_1^+ maps were acquired in this study, they were not always acquired in the same region of the breast as the tumor. Therefore, and because B_1^+ maps are often noisy, we used the template approach developed earlier for a unilateral transmit setup to get the B_1^+ distribution in the tumor (18). It has recently been demonstrated that the template approach is also feasible for the bilateral transmit setup used in this work (26). B_1^+ template scaling was performed per breast, using the measured B_1^+ maps.

3.2.4 Evaluation of corrected patient data

As was described in Section 3.2.1, the value for ρ was estimated using either the precontrast image or a heuristic fallback strategy in case the value estimated from the precontrast image was demonstrably too low. We investigated when this fallback strategy was used and whether the values returned by the fallback strategy were in the same range as the values returned by the default strategy. To this end, colored scatter plots were created that indicate which ρ -estimation strategy was used for different template-estimated B_1^+ levels in the tumor, as well as the corresponding B_1^+ levels in the measured map and what value of ρ was returned. The B_1^+ level in the measured map was investigated because the AFI B_1^+ mapping strategy used is known to have a reliable linear range limited to 50 – 150% of the nominal angle (22).

Curves were quantified by their amount of washin, washout and peak enhancement. These metrics were calculated per voxel location and defined as follows:

$$\begin{cases} WO = \frac{S_1 - S_5}{S_1} \\ WI = \frac{S_1 - S_0}{S_0} \\ PE = \frac{\max_{i=1,\dots,5} S_i - S_0}{S_0} \end{cases} \quad (3.4)$$

where S_i is the signal intensity at time point i , with time point 0 the precontrast scan and time points 1 – 5 the postcontrast scans in chronological order.

Tumor masks were obtained semi-automatically, using the method of Alderliesten *et al.* with manually determined seed points (27). The effect of the DCE correction on the curve types was assessed in the most enhancing part of the tumor only (28). The most enhancing part of the tumor was defined as those voxels in the tumor mask that belonged to the top ten percent in terms of washin. The mean curve in those voxels was calculated and the curve shape was determined: curves that had a washout of more than 10% were designated type III; those with a washout of less than -10% were designated type I; those that fell in-between were designated type II. The occurrences of each type for both the original and corrected datasets were compared against those found by Kuhl *et al.* (3).

In order to investigate whether the DCE correction affects tumors of different grades differently, the distribution of washin, washout and peak enhancement values were calculated inside the tumor mask and plotted for each grade before and after correction. The distributions were calculated using a kernel-based probability density estimation routine.

3.3 Results

3.3.1 Simulations

The noise amplification induced by the Haacke-based method was consistently larger than that induced by the proposed direct method. Additionally, the mean of the curves corrected by the proposed method was consistently closer to the ground truth. Figure 3.4 shows this for two B_1^+ levels.

Due to the higher noise amplification at relatively low B_1^+ levels, corrected time-intensity curves at B_1^+ levels below a certain threshold had a higher RMSE with respect to the ground truth than uncorrected ones. This threshold was 36% of the nominal angle for the Haacke-based method and 20% of the nominal angle for the direct method. However, at such low B_1^+ levels, the SNR in the corrected images is very low, below 10% of the original precontrast SNR. The Haacke-based method maintained the noise level in the corrected images at the level of the original precontrast image for a B_1^+ level of at least 54% of the nominal angle. The direct method maintained this noise level until 43% of the nominal angle.

3.3.2 Patient data

As Figure 3.5A shows, the fallback ρ -estimation strategy was only used for tumors that have a minimum B_1^+ of 50% or less. The median B_1^+ level of the measured map, and by extent the reliability of those measurements, did not have an influence. Figure 3.5B shows that the estimated values for ρ by the fallback strategy are in the same range as those estimated by the default strategy.

Figure 3.6 shows an example of the effect of correction on the mean curve of the top ten percent most enhancing voxels of a grade 2 tumor with a low B_1^+ level. This example changed from a type II plateau curve to a type III washout curve. A change to a higher curve type was the most common change across the dataset: five patients went up from type II to type III, one patient went up from type I to type II, and one patient went

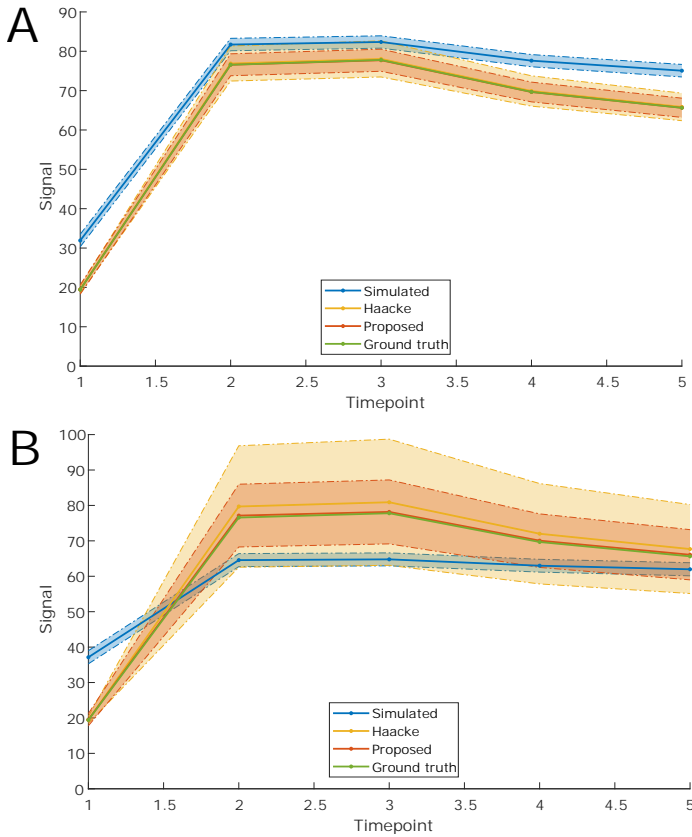


Figure 3.4: Demonstration of noise amplification in simulations at a B_1^+ level of 50% (A) or 30% (B) of the nominal angle. The time-intensity curves shown are the mean curve of all noise instances, the shaded area indicates the standard deviation. Noise amplification increases for lower B_1^+ levels for both the Haacke-based and proposed methods, but the proposed method amplifies the noise less strongly.

up two levels from type I to type III. Only two patients changed curve types to a lower type: one patient went down from type II to type I, and one patient went down from type III to type II. For the majority, 29 of the patients, the curve type did not change. Of all six cases that changed into a type III curve, four had a grade 2 tumor, one had a grade 1 tumor and in one case the patient received NAC so the tumor grade couldn't be assessed. Table 3.2 summarizes the distribution of curve types both of the original and the corrected DCE time series. The distribution of the corrected series corresponds better to the distribution found in literature (3).

Figure 3.7 shows the distribution of washout, washin and peak enhancement values per grade, both for the original and the corrected DCE time series. As expected, especially low values of washout, washin and peak enhancement are reduced. Additionally, the overlap between the distributions for grade 1 and grade 2 has been reduced.

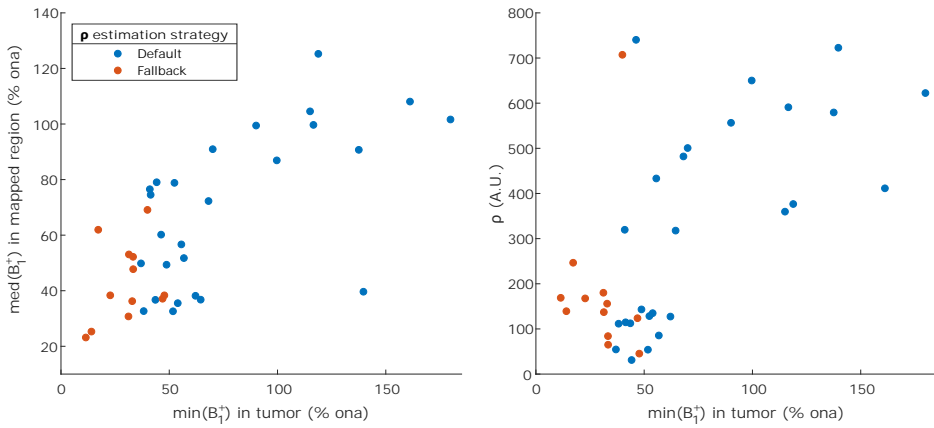


Figure 3.5: Occurrence and influence of the ρ estimation strategy. The fallback strategy is only used for low B_1^+ levels in the tumor ($< 50\%$ ona). The values estimated by the fallback strategy are in the same range as those estimated by the default strategy. Abbreviations: A.U. - Arbitrary Units, % ona - percentage of the nominal flip angle, ρ - proton density (weighted with the MR system's receive chain sensitivity).

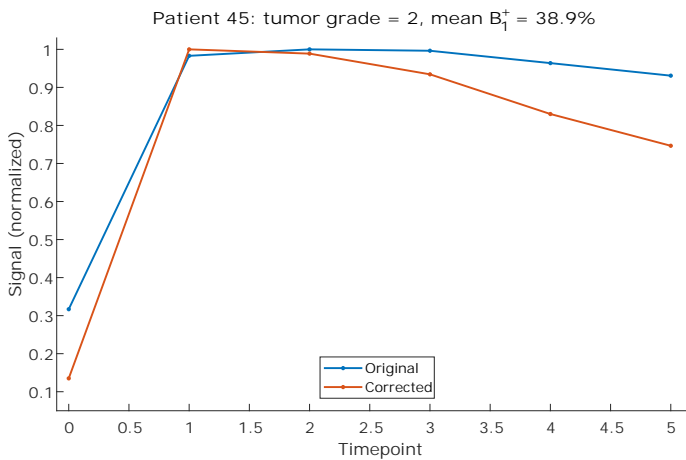


Figure 3.6: Typical example of an original vs a corrected time-intensity curve. The curves shown are the mean of the top ten percent most enhancing tumor voxels. Each curve has been normalized to its own maximum for clarity.

Table 3.2: Distribution of time-intensity curve types both before and after correction, compared against literature values (3). Abbreviation: PROFILE - Patient Risk Based on Functional MRI.

Dataset	Type I	Type II	Type III
Kuhl 1999	8,9%	33,6%	57,4%
PROFILE original	13%	47%	39%
PROFILE corrected	11%	37%	53%

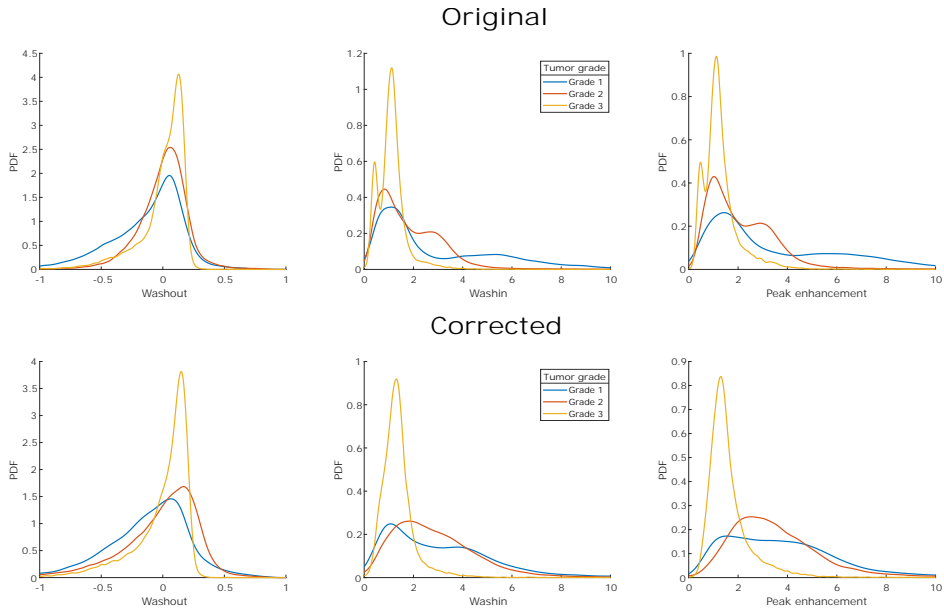


Figure 3.7: Washin, washout and peak enhancement distributions per grade, before and after DCE correction. Notice how in all distributions the number of low values are reduced by the correction, as expected. Abbreviations: DCE - Dynamic Contrast Enhanced (MRI), PDF - Probability Density Function.

3.4 Discussion

This chapter set out to investigate in which B_1^+ range DCE time series are still correctable for the B_1^+ non-uniformity effect post acquisition. The answer depends on the amount of SNR one is willing to sacrifice. In DCE-MRI, the precontrast image usually has the lowest SNR, simply because it has the lowest amount of signal. Therefore, maintaining at least that amount of SNR in the corrected postcontrast images seems like a logical choice. In that case, simulations show the lowest B_1^+ level that can be corrected for with the proposed method is 43% of the nominal angle. If one is willing to sacrifice more SNR one might go lower, but below 40% of the nominal angle the SNR dropped steeply.

The patient data showed that if one wants to prevent the fallback heuristic ρ -estimation strategy from kicking in, B_1^+ levels lower than 50% should be avoided. However, the estimated values for ρ using the heuristic approach are in the same range as the ones estimated with the default approach, so extending this range down to 43% as suggested in the previous paragraph might be justified. Both correctable ranges are too narrow to reliably correct all data gathered with the current setup used in this study, but recent results suggest that they may be compatible with the degree of homogeneity that can be achieved with a novel bilateral transmit array (13).

The effect of DCE correction on the measured time-intensity curves was as expected. The correction amplified small differences between time points such that most changes in curve type were away from the plateau type II to either type I or type III. The

same effect is seen in Figure 3.7, which shows a clear reduction of low washin, washout and peak enhancement values. The one patient that went down from type III to type II had a B_1^+ level in the tumor of higher than 100%, which explains why the change went the other way.

Although the size of the dataset is limited, it is promising to see that after correction the distribution of curve types roughly corresponds to the one found by Kuhl *et al.* (3). Since no ground truth is available for DCE time curves in vivo, this is the only kind of validation that can be performed with the current dataset. It is important to consider changes in the inclusion criteria between the patient group used in this study and the one investigated by Kuhl *et al.* Both groups only contain malignancies determined on the basis of histology, but an additional inclusion criterion for our group was eligibility for breast conserving surgery (19). Most notably, this might cause differences in tumor size, family history and patient age between the compared groups (29). A scan rescan protocol where patients are scanned both at 1.5T or 3T and 7T might give a higher evidence level, but even those studies are limited by the fact that DCE-MRI cannot be performed twice on the same day due to the slow clearance of contrast agents through the kidneys (30).

Given the promising results obtained regarding less overlap between grades in washin, washout and peak enhancement values, we additionally calculated image features related to the intensity in and heterogeneity of the tumor from both the original and corrected DCE time series (31,32). We investigated how the original and corrected features were associated to tumor grade, and if they were able to predict tumor grade. For the sum average texture feature of the washout image, the corrected values showed an increase in the area under the curve for predicting tumor grade (grade 1 versus grade 2 and 3) from 0.52 to 0.85. This increase was not significant after Bonferroni correction. As texture features are more commonly used in developing prediction models, a DCE correction could impact the performance of such models. However, the size of this dataset is such that further validation studies are needed.

This study has some limitations. First, the correctable B_1^+ range reported in this work, has only been investigated for one set of TR and flip angle. This range will change slightly depending on the TR and flip angle used. However, most DCE imaging protocols operate with parameters close to those used in this study, since these are close to the maximum sensitivity to T_1 changes (see Figure 3.2). The correctable B_1^+ range will thus also be similar. For protocols that have very different parameters, the theoretical B_1^+ range can always be inferred from simulations like in this work.

A second limitation is that a generic coil-specific B_1^+ template was the source of B_1^+ information in this work. Though this template performs well, generally as well as conventional mapping approaches, some uncertainty in the level of B_1^+ estimation is to be expected: a previous study reported a mean RMSE of 4% of the nominal angle (26). This might be one of the reasons why the proposed method switches to the default strategy only for low B_1^+ levels: an underestimation of the B_1^+ level at low levels could cause the measured signal to exceed the theoretical maximum at the wrongly estimated B_1^+ level. This issue could be solved by using a B_1^+ mapping method with a high dynamic range, but those are time consuming and not likely to be inserted into a clinical protocol. Addition-

ally, our simulations show that the noise enhancement at low B_1^+ levels is considerable, so DCE corrections will probably gain little when a B_1^+ map with a high dynamic range is added.

As proposed by Haacke *et al.*, a single, fixed value for the precontrast T_1 was used for all corrections (17). This value was based on measurements of healthy volunteers. Since most breast tumors are not visible on precontrast DCE-MRI, their T_1 is expected to be in the same range as that of healthy breast tissue. Moreover, the results of Haacke *et al.* also show that the influence of the fixed precontrast T_1 is very limited. Still, future studies might investigate if there is a benefit in estimating the precontrast T_1 on a per-patient basis.

In conclusion, our results show that correction for inhomogeneous B_1^+ is feasible at good SNR if the B_1^+ level is at least 50% of the nominal angle. This might be extended down to 43% of the nominal angle, if accurate B_1^+ maps are available at low levels. The effect of correcting a dataset with a high variability in B_1^+ was substantial: curve types changed in 25% of the patients, and the distribution of curves across curve types corresponds better with the distribution found in literature after correction. Additionally, there is an indication that correction might improve the performance of tumor grade prediction models.

References

1. Kaiser WA, Zeitler E. MR Imaging of the Breast - Fast Imaging Sequences with and without Gd-Dtpa - Preliminary-Observations. *Radiology* 1989;170(3):681-686.
2. Morris EA. Breast cancer imaging with MRI. *Radiol Clin North Am* 2002;40(3):443-466.
3. Kuhl CK, Mielcareck P, Klaschik S, Leutner C, Wardelmann E, Gieseke J, Schild HH. Dynamic breast MR imaging: Are signal intensity time course data useful for differential diagnosis of enhancing lesions? *Radiology* 1999;211(1):101-110.
4. Ladd ME, Bachert P, Meyerspeer M, Moser E, Nagel AM, Norris DG, Schmitter S, Speck O, Straub S, Zaiss M. Pros and cons of ultra-high-field MRI/MRS for human application. *Prog Nucl Mag Res Sp* 2018;109:1-50.
5. Pinker K, Bogner W, Baltzer P, Trattng S, Gruber S, Abeyakoon O, Bernathova M, Zaric O, Dubsy P, Bago-Horvath Z, Weber M, Leithner D, Helbich TH. Clinical application of bilateral high temporal and spatial resolution dynamic contrast-enhanced magnetic resonance imaging of the breast at 7 T. *Eur Radiol* 2014;24(4):913-920.
6. Stehouwer BL, Klomp DWJ, van den Bosch MAAJ, Korteweg MA, Gilhuijs KGA, Witkamp AJ, van Diest PJ, Houwert KAF, van der Kemp WJM, Luijten PR, Mali WPTM, Veldhuis WB. Dynamic contrast-enhanced and ultra-high-resolution breast MRI at 7.0 Tesla. *Eur Radiol* 2013;23(11):2961-2968.
7. Schmitz AMT, Loo CE, Wesseling J, Pijnappel RM, Gilhuijs KGA. Association between rim enhancement of breast cancer on dynamic contrast-enhanced MRI and patient outcome: impact of subtype. *Breast Cancer Res Treat* 2014;148(3):541-551.
8. Krikken E, Khlebnikov V, Zaiss M, Jibodh RA, van Diest PJ, Luijten PR, Klomp DWJ, Van Laarhoven HWM, Wijnen JP. Amide chemical exchange saturation transfer at 7 T: a possible biomarker for detecting early response to neoadjuvant chemotherapy in breast cancer patients. *Breast Cancer Res* 2018;20.
9. Krikken E, van der Kemp WJM, van Diest PJ, van Dalen T, van Laarhoven HWM, Luijten PR, Klomp DWJ, Wijnen JP. Early detection of changes in phospholipid metabolism during neoadjuvant chemotherapy in breast cancer patients using phosphorus magnetic resonance spectroscopy at 7T. *NMR Biomed* 2019:e4086.
10. Schmitz AMT, Veldhuis WB, Menke-Pluijmers MBE, van der Kemp WJM, van der Velden TA, Viergever MA, Mali WPTM, Kock MCJM, Westenend PJ, Klomp DWJ, Gilhuijs KGA. Preoperative indication for systemic therapy extended to patients with early-stage breast cancer using multiparametric 7-tesla breast MRI. *PLoS One* 2017;12(9).
11. Kuhl CK, Kooijman H, Gieseke J, Schild HH. Effect of B-1 inhomogeneity on breast imaging at 3.0 T. *Radiology* 2007;244(3):929-930.

12. Umutlu L, Maderwald S, Kraff O, Theysohn JM, Kuemmel S, Hauth EA, Forsting M, Antoch G, Ladd ME, Quick HH, Lauenstein TC. Dynamic Contrast-Enhanced Breast MRI at 7 Tesla Utilizing a Single-loop Coil: A Feasibility Trial. *Acad Radiol* 2010;17(8):1050-1056.
13. Krikken E, Steensma BR, Voogt IJ, Luijten PR, Klomp DWJ, Raaijmakers AJE, Wijnen JP. Homogeneous B-1(+) for bilateral breast imaging at 7 T using a five dipole transmit array merged with a high density receive loop array. *NMR Biomed* 2019;32(2).
14. van der Velden TA, Italiaander M, van der Kemp WJM, Raaijmakers AJE, Schmitz AMT, Luijten PR, Boer VO, Klomp DWJ. Radiofrequency Configuration to Facilitate Bilateral Breast P-31 MR Spectroscopic Imaging and High-Resolution MRI at 7 Tesla. *Magn Reson Med* 2015;74(6):1803-1810.
15. Bedair R, Graves MJ, Patterson AJ, McLean MA, Manavaki R, Wallace T, Reid S, Mendichovszky I, Griffiths J, Gilbert FJ. Effect of Radiofrequency Transmit Field Correction on Quantitative Dynamic Contrast-enhanced MR Imaging of the Breast at 3.0 T. *Radiology* 2016;279(2):368-377.
16. Tsai WC, Kao KJ, Chang KM, Hung CF, Yang Q, Lin CE, Chen CM. B1 Field Correction of T1 Estimation Should Be Considered for Breast Dynamic Contrast-enhanced MR Imaging Even at 1.5 T. *Radiology* 2017;282(1):55-62.
17. Haacke EM, Filletti CL, Gattu R, Ciulla C, Al-Bashir A, Suryanarayanan K, Li M, Latif Z, DelProposto Z, Sehgal V, Li T, Torquato V, Kanaparti R, Jiang J, Neelavalli J. New algorithm for quantifying vascular changes in dynamic contrast-enhanced MRI independent of absolute T1 values. *Magn Reson Med* 2007;58(3):463-472.
18. van Rijssel MJ, Pluim JPW, Luijten PR, Gilhuijs KGA, Raaijmakers AJE, Klomp DWJ. Estimating B-1(+) in the breast at 7T using a generic template. *NMR Biomed* 2018;31(5).
19. Schmitz AMT, Veldhuis WB, Menke-Pluijmers MBE, van der Kemp WJM, van der Velden TA, Kock MCJM, Westenend PJ, Klomp DWJ, Gilhuijs KGA. Multiparametric MRI With Dynamic Contrast Enhancement, Diffusion-Weighted Imaging, and 31-Phosphorus Spectroscopy at 7 T for Characterization of Breast Cancer. *Invest Radiol* 2015;50(11):766-771.
20. Pruessmann KP, Weiger M, Scheidegger MB, Boesiger P. SENSE: Sensitivity encoding for fast MRI. *Magn Reson Med* 1999;42(5):952-962.
21. Thomasson D, Purdy D, Finn JP. Phase-modulated binomial RF pulses for fast spectrally-selective musculoskeletal imaging. *Magn Reson Med* 1996;35(4):563-568.
22. Yarnykh VL. Actual flip-angle imaging in the pulsed steady state: A method for rapid three-dimensional mapping of the transmitted radiofrequency field. *Magn Reson Med* 2007;57(1):192-200.
23. Klein S, Staring M, Murphy K, Viergever MA, Pluim JPW. elastix: A Toolbox for Intensity-Based Medical Image Registration. *IEEE Trans Med Imaging* 2010;29(1):196-205.
24. Huizinga W, Klein S, Poot DHJ. Fast Multidimensional B-spline Interpolation Using Template Metaprogramming. In: Ourselin S, Modat M, editors. 2014; Biomedical Image Registration. WBIR 2014. Springer, Cham. p 11-20.
25. Studholme C, Hill DLG, Hawkes DJ. An overlap invariant entropy measure of 3D medical image alignment. *Pattern Recogn* 1999;32(1):71-86.
26. van den Wildenberg L, Krikken E, Wijnen JP, Pluim JPW, Klomp DWJ, van Rijssel MJ. Correcting breast MRI with a generic B-1(+) template for T-1 map calculation. *Proc Intl Soc Mag Reson Med* 2019;27:4499.
27. Alderliesten T, Schlieff A, Peterse J, Loo C, Teertstra H, Muller S, Gilhuijs K. Validation of semiautomatic measurement of the extent of breast tumors using contrast-enhanced magnetic resonance imaging. *Invest Radiol* 2007;42(1):42-49.
28. Gribbestad IS, Nilsen G, Fjosne HE, Kvinnsland S, Haugen OA, Rinck PA. Comparative Signal Intensity Measurements in Dynamic Gadolinium-Enhanced Mr Mammography. *Jmri-J Magn Reson Im* 1994;4(3):477-480.
29. Fajdic J, Djurovic D, Gotovac N, Hrgovic Z. Criteria and procedures for breast conserving surgery. *Acta informatica medica : AIM : journal of the Society for Medical Informatics of Bosnia & Herzegovina : casopis Društva za medicinsku informatiku BiH* 2013;21(1):16-19.
30. Aime S, Caravan P. Biodistribution of Gadolinium-Based Contrast Agents, Including Gadolinium Deposition. *J Magn Reson Imaging* 2009;30(6):1259-1267.
31. Gilhuijs KGA, Giger ML, Bick U. Computerized analysis of breast lesions in three dimensions using dynamic magnetic-resonance imaging. *Med Phys* 1998;25(9):1647-1654.
32. Chen W, Giger ML, Li H, Bick U, Newstead GM. Volumetric texture analysis of breast lesions on contrast-enhanced magnetic resonance images. *Magn Reson Med* 2007;58(3):562-571.



Reducing distortions in echo-planar breast imaging at ultrahigh field with high-resolution off-resonance maps



Based on:

M.J. van Rijssel, F. Zijlstra, P.R. Seevinck, P.R. Lijten, K.G.A. Gilhuijs, D.W.J. Klomp, J.P.W. Pluim; Reducing distortions in echo-planar breast imaging at ultrahigh field with high-resolution off-resonance maps, *Magnetic Resonance in Medicine* 2019, 82(1):425-435

Abstract

Purpose

Diffusion weighted imaging (DWI) is a promising modality in breast MRI, but its clinical acceptance is slow. Analysis of DWI is hampered by geometric distortion artifacts, which are caused by off-resonant spins in combination with the low phase encoding bandwidth of the echo-planar imaging (EPI) sequence used. Existing correction methods assume smooth off-resonance fields, which we show to be invalid in breast where high discontinuities arise at tissue interfaces.

Methods

We developed a distortion correction method that incorporates high-resolution off-resonance maps to better solve for severe distortions at tissue interfaces. The method was evaluated quantitatively both ex-vivo in a porcine tissue phantom and in-vivo in five healthy volunteers. The added value of high-resolution off-resonance maps was tested using a Wilcoxon signed rank test comparing the quantitative results obtained with a low-resolution off-resonance map with those obtained with a high-resolution map.

Results

Distortion correction using low-resolution off-resonance maps corrected most of the distortions, as expected. Still, all quantitative comparison metrics showed increased conformity between the corrected EPI images and a high-bandwidth reference scan for both the ex-vivo and in-vivo experiments. All metrics showed a significant improvement when a high-resolution off-resonance map was used ($p < 0.05$), in particular at tissue boundaries.

Conclusion

The use of off-resonance maps of a resolution higher than EPI scans significantly improves upon existing distortion correction techniques, specifically by superior correction at glandular tissue boundaries.

4.1 Introduction

Diffusion-weighted MRI (DWI) is an upcoming modality in breast oncology imaging. This technique, that sensitizes the MR signal for the (microscopic) motion of water molecules, has achieved promising results in recent years. Without the need for contrast agents, it potentially allows differentiation between benign and malignant lesions and prediction of response to neoadjuvant chemotherapy (1,2). Despite these promising feats, currently, dynamic contrast-enhanced MRI (DCE-MRI) is still the dominant MRI modality in breast radiology. Recent examples for the added value of tumor heterogeneity assessment include the observation that rim-enhancing tumors are a predictor for worst survival in patients with triple-negative tumors and a study that showed the value of the combination of temporal and morphological tumor characteristics in predicting treatment failure (3,4).

Given the promising results obtained in DCE-MRI, recent studies have tried to assess the added value of tumor heterogeneity on DWI. Promising results have been achieved in the improvement of benign/malignant differentiation and prediction of tumor proliferation status (5,6). In these studies, the degree of heterogeneity has been obtained either with qualitative measures or through manually drawn tumor regions on the DWI.

Analysis of heterogeneity on DWI is severely hampered by the geometric distortions that arise in most DWI acquisitions. The vast majority of DWI acquisitions uses the conventional Stejskal-Tanner approach with an echo-planar imaging (EPI) readout (7). EPI acquisitions suffer from extremely low bandwidth in the phase encode direction, which makes them prone to severe distortion artefacts due to static-field (B_0) inhomogeneities (8). Additionally, since the readout bandwidth decreases with increasing resolution, the geometric distortion artefact limits the resolution of DWI in practice. Especially at ultrahigh field, this limit is reached long before the signal-to-noise ratio (SNR) limit. Due to the geometric distortion artefact, the acquired DWI data are no longer aligned with other MRI data less prone to distortions, hampering the analysis of tumor heterogeneity on DWI data and the integration of these data with e.g. DCE-MRI data in a true multiparametric analysis of MRI.

Though several correction methods are available that attempt to recover undistorted images, all of these assume that ΔB_0 is locally smooth (9). As we will show, this assumption of locally smooth ΔB_0 is not valid in the human breast. In lipid-rich organs like the human breast, off-resonance effects are worsened by highly discontinuous static-field inhomogeneities at tissue interfaces. These discontinuities are caused by susceptibility differences between adipose tissues and aqueous glandular tissues. Though breast tumors nearly always reside in glandular tissue, most are located on these interfaces with adipose tissue (10,11). The significance of these local susceptibility-induced off-resonance effects will be demonstrated in this work. We use an ultrahigh field strength of 7T, since DWI data are affected more by this artifact with increasing field strength.

Since we cannot assume locally smooth ΔB_0 , we develop a novel EPI distortion correction technique based on an inverse-problem strategy that is free of this assumption and works with off-resonance maps of sufficiently high resolution to capture ΔB_0 discontinuities at tissue interfaces (12,13). Then, we test the hypothesis that the confor-

mity between the corrected image and a high-bandwidth reference improves using this technique.

This chapter we will show three experiments. First, in-silico simulations were performed to assess the effect of susceptibility on ΔB_0 in an otherwise perfectly homogeneous environment. Second, ex-vivo 7T MRI measurements of ΔB_0 were performed in an ex vivo porcine tissue phantom to confirm our in-silico findings. Finally, in-vivo measurements of five healthy human volunteers were performed to test our hypothesis and novel distortion correction method in a hospital setting.

4.2 Methods

4.2.1 In-silico simulations

In-silico simulations were performed to show the extent of local off-resonance effects caused solely by the susceptibility difference between glandular tissue and adipose tissue. A 3D unilateral breast model was created, based on a 7T MRI scan of a 27-year-old healthy female volunteer. The subject was scanned with a dual-echo gradient-echo Dixon acquisition (acquired resolution $1.5 \times 1.5 \times 1.5 \text{ mm}^3$, TR 5.4 ms, in-phase TE 1.48ms, out-phase TE 3.95, readout bandwidth 2278 Hz). Based on the Dixon in-phase, water and fat reconstructions, a 3D susceptibility model of the volunteer's breast was constructed, using tabulated values for air, water and fat: 0.36×10^{-6} for air, -9.05×10^{-6} for water and -7.8×10^{-6} for fat (14,15). From this 3D susceptibility model, local ΔB_0 variation in an external magnetic field of 7T was predicted, using the method outlined in (16).

4.2.2 Ex-vivo measurements

Ex-vivo high-resolution measurements of off-resonance in a porcine tissue phantom were used here as a model for breast tissue. The many muscle-fat interfaces present allowed us to investigate whether our findings in the simulations of high discontinuities in ΔB_0 could also be observed in an animal model. Additionally, since the specimen is completely stationary, this allowed us to develop a high-resolution ΔB_0 -based EPI distortion correction algorithm without having to take subject motion into account.

All experiments were performed using a unilateral breast coil setup on a 7T whole-body MR system (Achieva; Philips, Cleveland, Ohio, USA). The protocol included two fat-suppressed spin-echo EPI acquisitions with opposed phase encoding directions ($2 \times 2 \times 3 \text{ mm}^3$, bandwidth/voxel 20 Hz), a non-accelerated spin-echo acquisition with otherwise equal imaging parameters as reference, and a dual-echo ΔB_0 measurement at a higher resolution ($0.7 \times 0.7 \times 3 \text{ mm}^3$). In order to avoid lipid bias in the off-resonance measurements, the echo times at which the ΔB_0 map was measured were chosen such that a lipid model consisting of the 10 largest resonances was in phase with the water signal (17). Since high discontinuities in off-resonance might occur at tissue interfaces, we chose a gradient echo technique with short echo times to counter potential signal dropout in the ΔB_0 maps. Only at very large susceptibility differences, e.g. close to metallic implants, the ΔB_0 maps may experience intra-voxel dephasing. This is rare in the breast, as metallic implants are not common in this organ. In such cases, the EPI

Table 4.1: Summary of scan parameters per sequence. Abbreviations: EPI – Echo Planar Imaging, SE – Spin Echo, LR – Left-to-Right phase encoding, RL – Right-to-Left phase encoding, ref. – reference scan, DE – Dual Echo, GE – Gradient Echo, ΔB_0 – main magnetic field off-resonance.

	SE-EPI	SE ref.	DE GE ΔB_0
<i>Ex-vivo scans</i>			
TR (ms)	3761	3761	5.6
TE (ms)	53	53	2.92, 3.94
Resolution	2x2 mm ² 3 mm slices	2x2 mm ² 3 mm slices	0.7x0.7 mm ² 3 mm slices
Matrix size	80x80 15 slices	80x80 15 slices	224x224 15 slices
Readout bandwidth (Hz)	2807	3217	1219
EPI bandwidth (Hz)	23.7	-	-
EPI direction	LR/RL	-	-
EPI factor	80	-	-
Scan time (min:s)	0:08	5:08	0:32
<i>In-vivo scans</i>			
TR (ms)	3761	3761	7.0
TE (ms)	53	53	2.92, 3.94
Resolution	2x2 mm ² 3 mm slices	2x2 mm ² 3 mm slices	1x1 mm ² 3 mm slices
Matrix size	80x80 15 slices	80x80 15 slices	160x160 15 slices
Readout bandwidth (Hz)	2036	1696	636
EPI bandwidth (Hz)	20.1	-	-
EPI direction	LR/RL	-	-
EPI factor	80	-	-
Scan time (min:s)	0:08	5:08	0:22

scans will also suffer from signal loss, which cannot be recovered by our correction method. Detailed scan parameters for all scans can be found in Table 4.1.

EPI distortion correction was applied as described in Section 4.2.4.1 to pairs of oppositely encoded images using the ΔB_0 map measured at $0.7 \times 0.7 \times 3 \text{ mm}^3$, either down sampled to the EPI resolution ($2 \times 2 \times 3 \text{ mm}^3$) or at the native ΔB_0 map resolution ($0.7 \times 0.7 \times 3 \text{ mm}^3$) that better captures local ΔB_0 discontinuities at tissue interfaces. The resulting images were compared quantitatively to the non-accelerated reference scan as described in Section 4.2.5.

4.2.3 In-vivo measurements

All experiments conducted were in accordance with the guidelines of the local ethical committee and, prior to the examination, written informed consent was obtained from all volunteers. In-vivo measurements were performed in five healthy female volunteers (age mean: 30, range: 25 – 46 years), using the same 7T setup as described in Section 4.2.2. The in-vivo acquisition protocol was nearly identical to the ex-vivo acquisition protocol outlined above, with the exception that the ΔB_0 map resolution was slightly reduced. We acquired a ΔB_0 map at $1 \times 1 \times 3 \text{ mm}^3$, a set of opposite phase-encoded EPI images at $2 \times 2 \times 3 \text{ mm}^3$, and an undistorted reference scan at the same resolution. Other scan parameters were chosen like in the ex-vivo case, detailed scan parameters are reported in Table 4.1.

As there might be motion between the two EPI acquisitions, a motion-correction step was added before the distortion correction algorithm developed on the ex-vivo data, as described in Section 4.2.4.2. Since there might also be motion present between the corrected image and the reference spin-echo scan, a rigid registration is applied to the two before the quantitative comparison, as outlined in Section 4.2.5.

4.2.4 Distortion correction

4.2.4.1 Ex-vivo strategy

Distortion correction was performed using an inverse problem approach resembling techniques described earlier (12,13), adapted to allow for higher-resolution off-resonance maps than the measured EPI scan. In this approach, we strived to invert the EPI distortion process by first creating a forward model that describes how images are distorted under the influence of ΔB_0 . In order to iteratively approximate the inverse using the LSQR algorithm (18), the conjugate transpose of the forward model was also constructed and used in tandem with the forward model. The forward model (A) was described using fast steady state simulations, restricted to distortions in the phase encode direction. These simulations were implemented using the FORECAST method, which avoids direct calculation of the large and sparse matrix A , but allows calculation of matrix-vector products (19). This formulation allows efficient evaluation of both $A(\Delta B_0)x$ (the forward model) and $A(\Delta B_0)^H x$ (the conjugate transpose of the forward model), where A is the transformation matrix that maps undistorted to distorted space and x is the corrected image at equal or higher resolution than the measured EPI image.

The forward model was implemented for 2D slices since our acquisition is multi slice. Given that the bandwidth of the slice selective RF pulses is two orders of magnitude higher than the bandwidth in the phase encode direction, this is sufficient to explain 99% of the distortions. Distortions were modeled by considering that each k-space point is affected differently by off-resonance effects depending on its sampling time. Sampling time was defined as the time difference of the acquisition of the k-space point with respect to the center of the refocused echo. Thus, the acquired k-space signal S can be described by:

$$S(k_x(t'), k_y(t')) = \int_x \int_y \left(\rho(x, y) \cdot e^{i \cdot t' \cdot 2\pi\gamma \cdot \Delta B_0(x, y)} \cdot e^{-i2\pi(k_x(t')x + k_y(t')y)} \right) \quad (4.1)$$

with S the measured k-space signal distorted by off-resonance effects, ρ the effective (encoded) spin density, i the imaginary unit number, t' the sampling time for the current k-space point, γ the gyromagnetic ratio and ΔB_0 the off-resonance map for the entire slice. x and y respectively denote the frequency and phase encode directions, k_x and k_y are their Fourier counterparts. For computational efficiency, and to be able to apply the FORECAST model, we neglected time accrual along the frequency-encode direction and assumed a constant sampling time for each k-space line. This limits distortions to the phase encode direction only. Thus, the forward model is defined as follows:

$$S(k_x, k_y(t')) = \sum_x \sum_y \left(\rho(x, y) \cdot e^{i \cdot t' \cdot 2\pi\gamma \cdot \Delta B_0(x, y)} \cdot e^{-i2\pi(k_x x + k_y(t') y)} \right) \quad (4.2)$$

Since the dependency of k_x on t' is dropped, Equation 4.2 can be efficiently evaluated by using a fast Fourier transform (FFT) for every k_y :

$$\begin{aligned} S(k_x, k_y(t')) &= \sum_x \left(e^{-i2\pi k_x x} \sum_y \left(\rho(x, y) \cdot e^{i \cdot t' \cdot 2\pi\gamma \cdot \Delta B_0(x, y)} \cdot e^{-i2\pi k_y(t') y} \right) \right) \\ &= \mathcal{F}_x \sum_y \left(\rho(x, y) \cdot e^{i \cdot t' \cdot 2\pi\gamma \cdot \Delta B_0(x, y)} \cdot e^{-i2\pi k_y(t') y} \right) \end{aligned} \quad (4.3)$$

with \mathcal{F}_x the FFT along the frequency encode dimension. To allow evaluation of the model with off-resonance maps of higher resolution than the EPI image, S was subsequently cropped symmetrically around the center to the same resolution as the EPI.

The conjugate transpose model can be calculated in a similar fashion, by taking the conjugate transpose operation of the steps of the forward model and performing them in inverse order on a k-space that belongs to a deformed image. The conjugate transpose operation of Equation 4.3 was calculated by:

$$\hat{\rho}(x, y) = \sum_{t'} \left(\mathcal{F}_x^{-1}(\hat{S}(k_x, k_y(t'))) \cdot e^{i2\pi k_y(t') y} \cdot e^{-i \cdot t' \cdot 2\pi\gamma \cdot \Delta B_0(x, y)} \right) \quad (4.4)$$

with \mathcal{F}_x^{-1} the inverse FFT along the frequency encode dimension, \hat{S} a measured and zero-padded 2D EPI k-space and $\hat{\rho}$ the result of applying the conjugate transpose model to the measured slice. Note that the summation over t' implicitly sums over k_y ,

because k_y is a function of t' . Centered and symmetric zero-padding was applied to up-scale the measured EPI k-space to the resolution of the off-resonance map.

The inverse problem was then formulated as a damped least squares problem:

$$y = \underset{x}{\operatorname{argmin}} \left\| \begin{bmatrix} A \\ \lambda I \end{bmatrix} x - \begin{bmatrix} b \\ 0 \end{bmatrix} \right\|_2 \quad (4.5)$$

with y the corrected image, b the measured EPI data, I the identity matrix, and the regularization parameter λ . A range of values between 0.1 and 100 was tested for the regularization parameter λ ; the value that maximized the Pearson correlation between the corrected ex-vivo image and the undistorted reference ex-vivo image was chosen for both the ex-vivo specimen and all in-vivo subjects (see below). The inverse problem was solved using the LSQR algorithm where the matrix-vector products Ax and A^Hx were respectively described by the forward model and conjugate transpose model as described above (18).

4.2.4.2 In-vivo strategy

The in-vivo distortion correction strategy was identical to the ex-vivo strategy, but a motion correction step was added to account for subject motion between the acquisitions of the opposite phase encoded EPI images. Motion correction was applied by (arbitrarily) choosing the EPI image with LR phase encoding as reference frame and estimating rigid transformation parameters for both the other EPI image and the ΔB_0 map, such that they align with the first EPI image. Due to the severe geometric distortions that present themselves differently in both EPI images, regular registration strategies are unsuited for this problem. Therefore, we estimated the 12 parameters describing the two rigid transformations by minimizing the same error metric that was used in the distortion correction step. This was implemented using a Nelder-Mead simplex search that minimizes the residual of the LSQR EPI distortion correction algorithm's result (20). Preliminary experiments showed that two iterations of the LSQR algorithm sufficed for this estimation. The two sets of rigid transformation parameters that are obtained from the Nelder-Mead search, are used in the final EPI distortion correction where the LSQR algorithm is run until convergence.

4.2.5 Distortion correction evaluation

Quantitative evaluation between the corrected and non-distorted images was performed with six comparative metrics: Dice, Pearson correlation on the entire image and Pearson correlation on border pixels only. For Dice and border-only Pearson correlation a mask of the 'foreground' or glandular tissue pixels was needed in both the corrected and the reference image. This mask was obtained by thresholding using Otsu's method (21). The Dice coefficient was calculated directly on these two masks. Border-only Pearson correlation was calculated on the border pixels of the mask only, these were selected using MATLAB R2017b's implementation of the Moore-Neighbor tracing algorithm (22). Finally, a paired one-sided Wilcoxon signed rank test was performed on all quantitative metrics, comparing the values obtained with a low-res ΔB_0 map with the values obtained with a high-res ΔB_0 map, both with motion correction.

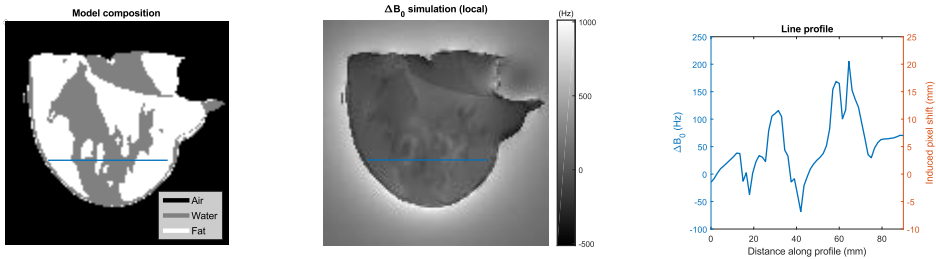


Figure 4.1: In-silico experiment. Left: breast model composition based on a Dixon acquisition; gray values indicate the location of air (black), water (gray) and fat (white). Middle: simulation result of local ΔB_0 effects caused solely by susceptibility differences between tissue types at a field strength of 7T. Right: line profile corresponding to the blue line drawn in the middle panel. The y-axis is marked in both off-resonance (unit: Hz) and induced pixel shift (unit: mm) for convenience. Abbreviation: ΔB_0 – main magnetic field off-resonance.

In the in-vivo scans, motion may be present between the acquisition of the first EPI image (arbitrarily chosen as reference for the correction algorithm and thus of the corrected image) and the acquisition of the reference scan. Therefore, an alignment of the corrected image to the spin-echo reference was applied to allow quantitative evaluation. Rigid registration was performed using a single-resolution approach and a normalized correlation error metric using Elastix (23).

4.3 Results

Figure 4.1 shows the influence of susceptibility on ΔB_0 in the breast, based on our in-silico experiment. Susceptibility differences between water and fat were sufficient to cause locally highly discontinuous transitions in ΔB_0 , leading to discontinuities of more than 100 Hz over distances as small as 5 mm at 7T. Note that discontinuities at tissue boundaries are especially substantial compared to the global gradient caused by the tissue-air boundary.

The ex-vivo results are presented in Figures 4.2 through 4.5. The processing time of the EPI distortion correction method was roughly 5 minutes for all 15 slices using the high-resolution ΔB_0 map. Figure 4.2 demonstrates that local discontinuities in ΔB_0 can also be found in a porcine tissue phantom model at fat-muscle interfaces and that they are easily missed in low-resolution acquisitions. The value for λ that maximized the correlation between the corrected image and the reference image was 1.7. This value was used for both the ex-vivo and in-vivo cases. Figure 4.3 shows a plot of the correlation values for λ values in the range of 0.5 to 5. Note that λ has a limited influence on the correlation and, by extent, on the corrected image in this range. For values below 0.5, the correlation dropped steeply. Figure 4.4 shows the improvement gained by using a higher resolution ΔB_0 map during EPI distortion correction for a single slice. The image corrected with a high-resolution ΔB_0 map has less noise and more accurately depicts small features present in the reference image. Quantitative metrics are shown in Figure 4.5 for no correction, correction with a low-resolution ΔB_0 map and correction with a high-resolution ΔB_0 map respectively. All metrics improved with increasing ΔB_0 map resolutions.

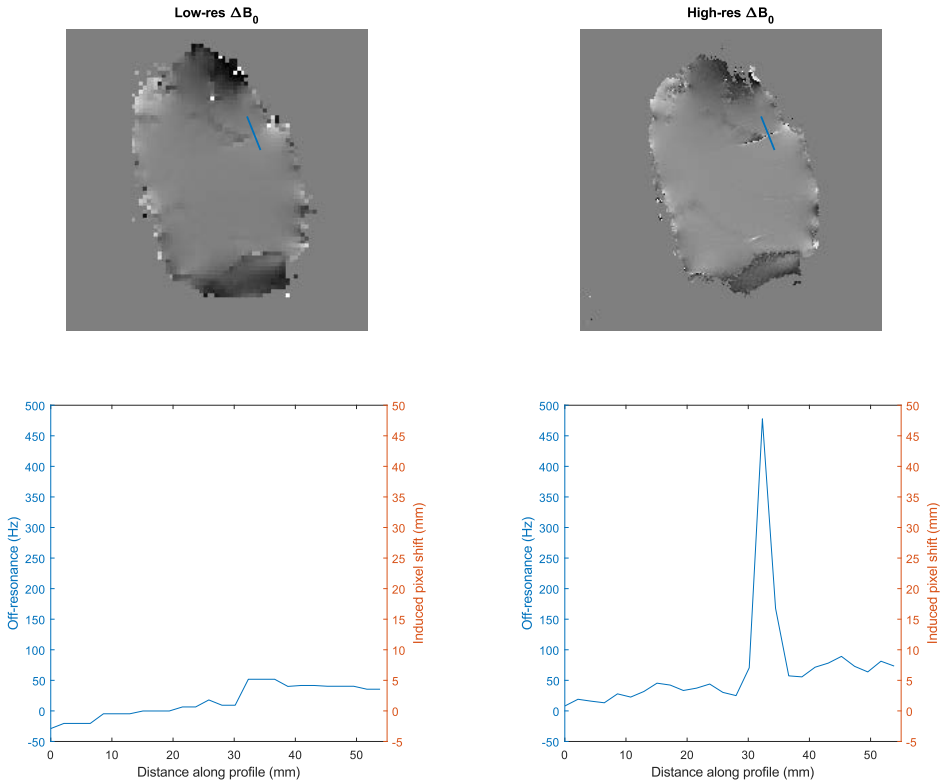


Figure 4.2: Off-resonance maps of a porcine tissue phantom acquired at different resolutions; left: 2×2 mm in plane, right: 0.7×0.7 mm in plane. The slice thickness was 3 mm in both cases. Notice how sharp and high discontinuities at tissue interfaces are missed in the low-resolution acquisition. The plots at the bottom indicate line profiles corresponding to the blue line drawn in the images at the top. The y-axis is marked in both off-resonance (unit: Hz) and induced pixel shift (unit: mm) for convenience. Abbreviation: ΔB_0 - main magnetic field off-resonance.

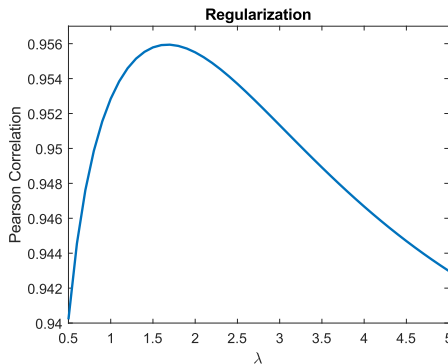


Figure 4.3: Influence of the choice of the regularization parameter λ on the Pearson correlation between the corrected and reference images in the ex-vivo experiment. The maximum is located at $\lambda = 1.7$. Note the limited range of the y-axis.

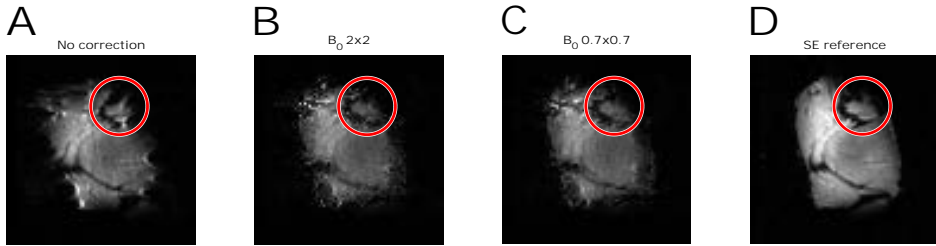


Figure 4.4: Ex-vivo experiment: Uncorrected EPI (A), EPI acquisition corrected for distortion (B & C) next to an undistorted reference image (D). Image B was corrected using a ΔB_0 map at the same resolution as the EPI acquisition (2x2 mm in plane), image C was corrected using a ΔB_0 map at a higher resolution (0.7x0.7 mm in plane). Notice how the corrected image C follows the anatomy of the sample more closely, especially in the red circle. Also notice the amount of signal pile-up directly left of the circle is reduced in image C with respect to image B. Abbreviations: EPI - Echo Planar Imaging, SE - Spin Echo, ΔB_0 - main magnetic field off-resonance.

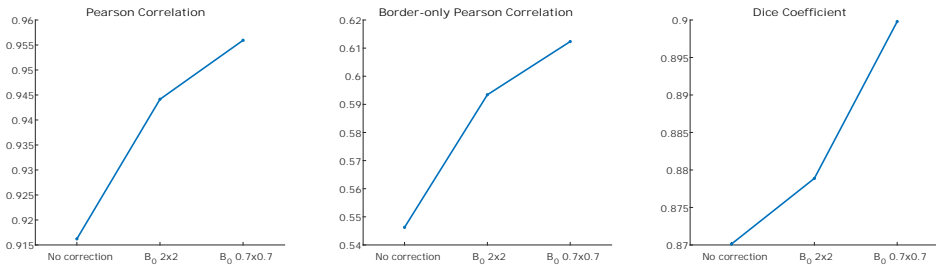


Figure 4.5: Ex-vivo results of quantitative comparisons between corrected EPI images and SE references. The x-axis indicates increasing levels of sophistication for correction strategies, starting with no correction at all, then low-resolution off-resonance maps and finally high-resolution off-resonance maps. Abbreviations: EPI - Echo Planar Imaging, SE - Spin Echo, ΔB_0 - main magnetic field off-resonance.

The in-vivo results are presented in Figures 4.6 through 4.8. The processing time for the in-vivo datasets varied between the volunteers, but was typically around 15 minutes per dataset (15 slices) for our combined motion and distortion correction strategy using the high-resolution ΔB_0 map. Figure 4.6 shows a side-by-side comparison of high-resolution and low-resolution ΔB_0 maps in-vivo for volunteer 3. Similar to what was found in the simulations and the ex-vivo scan, local discontinuities were present at tissue interfaces, which were missed in the low-resolution map. Figure 4.7 shows the improvement gained by using both motion correction and a higher-resolution ΔB_0 map for a single slice for volunteer 3. The difference with respect to the reference scan decreased with increasing ΔB_0 map resolution. Figure 4.8 shows the results of quantitative comparisons between corrected images and high-bandwidth references. Comparisons with the reference were made for non-corrected images, images corrected without motion correction and a low-resolution ΔB_0 map, images corrected with motion correction and a low-resolution ΔB_0 map, and images corrected with motion correction and a high-resolution ΔB_0 map respectively. The p-values that are reported resulted from a Wilcoxon signed rank test between the values obtained with a low-res ΔB_0 map and with a high-res ΔB_0 map, both with motion correction.

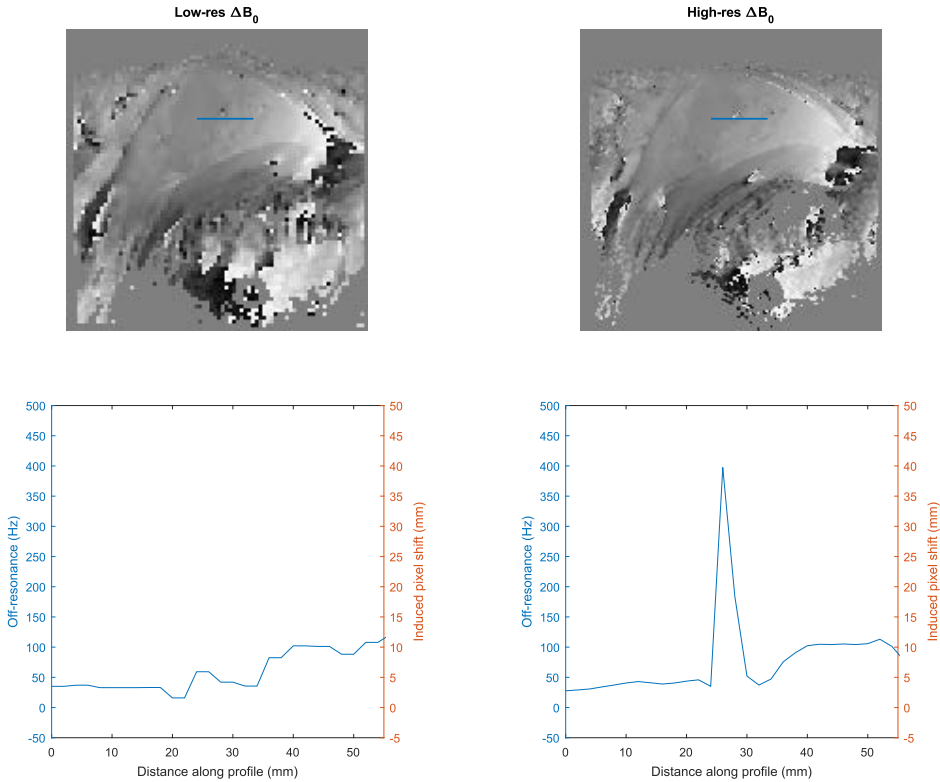


Figure 4.6: Off-resonance maps of a healthy volunteer at different resolutions; left: 2x2 mm in plane, right: 1x1 mm in plane. The slice thickness was 3 mm in both cases. Notice how sharp and high discontinuities at tissue interfaces are missed in the low-resolution acquisition. The plots at the bottom indicate line profiles corresponding to the blue line drawn in the images at the top. The y-axis is marked in both off-resonance (unit: Hz) and induced pixel shift (unit: mm) for convenience. Abbreviation: ΔB_0 – main magnetic field off-resonance.

4.4 Discussion

In this study, we aimed to improve the conformity between EPI images of the breast and other MRI images less prone to distortions, such as the standard DCE-MRI. We showed that existing distortion correction methods assuming a smooth off-resonance field are inadequate, due to severe field inhomogeneities that arise at tissue interfaces between aqueous and adipose tissues in the human breast. We proposed a distortion correction technique that doesn't assume a smooth off-resonance field and demonstrated that it performs better with increasing ΔB_0 spatial resolutions.

Our in-silico results show that, even due to susceptibility alone, sizable discontinuities in off-resonance can arise at tissue interfaces between adipose and glandular tissues, making these areas prone to high distortions on EPI-based diffusion weighted imaging. Since this is also where most breast tumors grow, it appears that many tumors would be affected by this (10,11).

Like in the in-silico simulations, highly local and sizable (up to several hundreds of Hz)

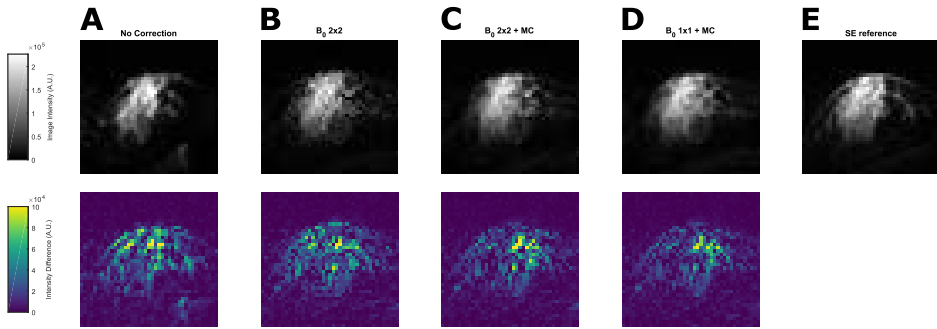


Figure 4.7: Top row: Uncorrected EPI (A), EPI acquisition corrected for distortion (B, C & D) next to an undistorted reference image (E). Image B was corrected using a ΔB_0 map at the same resolution as the EPI acquisition (2x2 mm in plane), image C was corrected using the same ΔB_0 map, but motion correction was applied prior to distortion correction, image D was corrected using a ΔB_0 map at a higher resolution (1x1 mm in plane) and motion correction. The bottom row shows the difference between the each corrected image and the reference image on a different color scale. Abbreviations: EPI - Echo Planar Imaging, MC - Motion Correction, SE - Spin Echo, ΔB_0 - main magnetic field off-resonance.

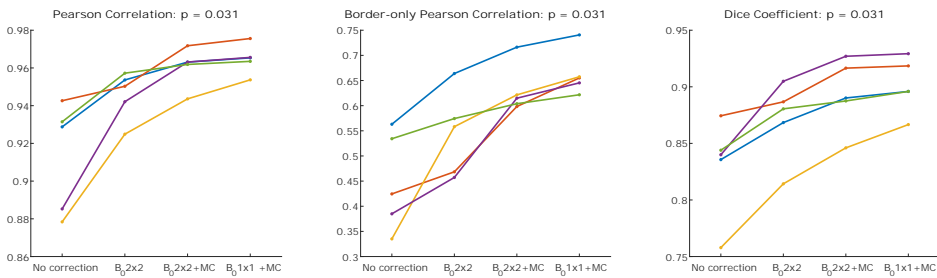


Figure 4.8: In-vivo results of quantitative comparisons between corrected EPI images and SE references. The x-axis indicates increasing levels of sophistication for correction strategies, starting with no correction at all, through low-resolution off-resonance maps without and with motion correction until high-resolution off-resonance maps with motion correction. P-values indicated are obtained with a paired Wilcoxon signed rank test between the values obtained with a low-res ΔB_0 map and with a high-res ΔB_0 map, both with motion correction. Abbreviations: EPI - Echo Planar Imaging, MC - Motion Correction, SE - Spin Echo, ΔB_0 - main magnetic field off-resonance.

discontinuities have been found both in high-resolution ex-vivo scans of a porcine tissue phantom and in high-resolution in-vivo scans of healthy volunteers. These discontinuities were missed in the low-resolution scans. In traditional DWI scans, such discontinuities coincide with pixel displacements in the order of 10 cm. In fact, the ex-vivo discontinuities seem to be even bigger than in our in-silico results, which might be explained by the fact that muscle tissue in a porcine tissue phantom has a larger susceptibility difference with fat than human breast glandular tissue due to a higher iron content. In the simulations a tabulated value for water susceptibility is used, which may not be correct for glandular tissue, but since in all distortion correction experiments measured ΔB_0 maps are used, this has not influenced our results beyond the in-silico simulation.

We developed a method that corrects distortion artifacts in EPI acquisitions using ΔB_0

maps at a resolution higher than the EPI images and taking subject motion into account. Both ex-vivo and in-vivo results demonstrate a benefit of using high-resolution ΔB_0 maps in EPI distortion correction. Though distortion correction using low-resolution ΔB_0 maps will already correct most of the distortions (observe for instance that the Pearson correlation is higher than 0.92 for all cases with low-resolution distortion correction with motion correction in Figure 4.8), alignment at the edges of glandular tissue can still greatly benefit from high-resolution distortion correction. This is best demonstrated by the improvements in border-only Pearson correlation in Figure 4.8.

The developed method requires high-resolution ΔB_0 maps. Acquiring a high-resolution off-resonance map may be time-consuming and could be undesirable in a clinical protocol. However, in this study we managed to limit the added time to less than 30 s, which may still be acceptable in a clinical setting. In most protocols a ΔB_0 map is already acquired for shimming purposes, simply acquiring this map with a higher resolution will satisfy the requirements of the developed method. Additionally, several techniques exist that allow the derivation of a high-resolution ΔB_0 map from clinically relevant image sources, such as Dixon techniques in DCE MRI, which are standard in many multiparametric cancer protocols. Alternatively, a merger of low-resolution ΔB_0 maps with high-resolution simulations based on segmentations, like we performed in the first part of this work, might be a feasible solution to avoid the extra time needed for obtaining high resolution ΔB_0 maps.

Techniques exist that estimate the ΔB_0 map directly from opposed phase encoded data (13). However, these methods need to assume a smooth ΔB_0 field in order to reduce the parameter space. They also ignore the resonance and susceptibility offsets between aqueous and adipose substances. Although these assumptions are valid in e.g. the brain, we have demonstrated they are not true in the breast, justifying the development of more sophisticated methods, as we have done here. The development of a method that estimates a high-resolution ΔB_0 map from opposite phase-encoded data without the assumption of a smooth ΔB_0 field could be viable and scan time efficient solution which should be investigated in future work.

Others go beyond field map estimation and try to estimate sub-voxel ΔB_0 gradients in order to account for signal dephasing (24). In order to be able to estimate these sub-voxel effects, they designed an acquisition scheme with multiple echo's and compensation gradients in the slice selection direction, which requires extra scan time. Validation was limited to computerized phantoms. Our forward model takes signal dephasing into account for the frequency and phase encode directions, by simulating a model that has a higher resolution than the returned image. It might be possible to extend our forward model to include dephasing in the slice selection direction as well by simulating several thinner slices at the same time. This is beyond the scope of this chapter. Additionally, the ΔB_0 map would need to be acquired with thinner slices, which increases the required scan time.

An alternative approach for EPI distortion correction is non-rigid registration to a non-distorted or less-distorted target image, e.g. the DCE MRI (25). Some authors have proposed to combine such image registration-based methods with field-based methods, with promising results (26,27). It is possible to extend our method in this direction,

for example by introducing non-rigid registration after the EPI distortion correction or by interleaving these two steps. When using non-rigid registration techniques, there is always a risk of contaminating the corrected image with information from the target image. For example, tumor heterogeneities in the target image that are absent in the source EPI may be propagated into the corrected image or, inversely, heterogeneities present in the source EPI but absent in target image may be removed. Since one of the main motivations of this work is to enable assessment of tumor heterogeneity in both DCE MRI and DWI accurately and independently, we have chosen not to pursue such an approach.

There is a linear relationship between field strength and the amount of off-resonance generated by magnetic susceptibility differences. Therefore, the induced distortions will also be lower at lower field strengths and the added benefit of our method will be less noticeable. Nevertheless, as Figure 4.6 demonstrates, severe discontinuities of up to 400 Hz have been found in-vivo, translating into 40 mm pixel shifts with our current protocol. At 1.5 T, this discontinuity would have been 86 Hz (3/14th part of 400 Hz), which would translate into a 9 mm pixel shift. At voxel sizes of roughly 2x2 mm in-plane, which are common for this kind of protocol, this is still not within acceptable limits. Therefore, we believe high-resolution ΔB_0 field information may merit distortion correction in DWI of the breast, even at more conventional field strengths.

Limitations of this study include the simplification in our distortion model to describe the phase-encode direction only. Since the readout bandwidth is roughly two orders of magnitude higher than the phase encode bandwidth of our sequence (see Table 4.1), we believe this simplification is justified since including the readout direction in the model would hardly improve distortion prediction and correction. A second limitation is the rigid motion-correction step that was implemented to test our method in in-vivo cases. Several non-rigid techniques exist, however these techniques could potentially correct for geometric distortion artefacts left uncorrected by our method and hide errors that our method made. In order to have a clean evaluation of our method's performance, we chose to limit our motion-correction step to rigid registration only. In terms of optimization, our method uses the LSQR method with L2 regularization. We considered these an appropriate choice, however they can be replaced by other optimizers and regularization strategies. Other optimizers might be more efficient in solving the inverse problem and other regularizers might improve the corrected images. Lastly, we cannot specify a minimum resolution for the ΔB_0 map that our method requires, since we have not tested different resolution levels. Future studies might focus on this, but we would like to stress that an increase with a factor 2x2 in plane as we have done for the in-vivo data already brings a significant improvement in distortion correction. As can be seen in Figure 4.2 for in-vivo and in Figure 4.6 for ex-vivo data, a small increase in resolution already allows the detection of severe local field inhomogeneities that are otherwise missed.

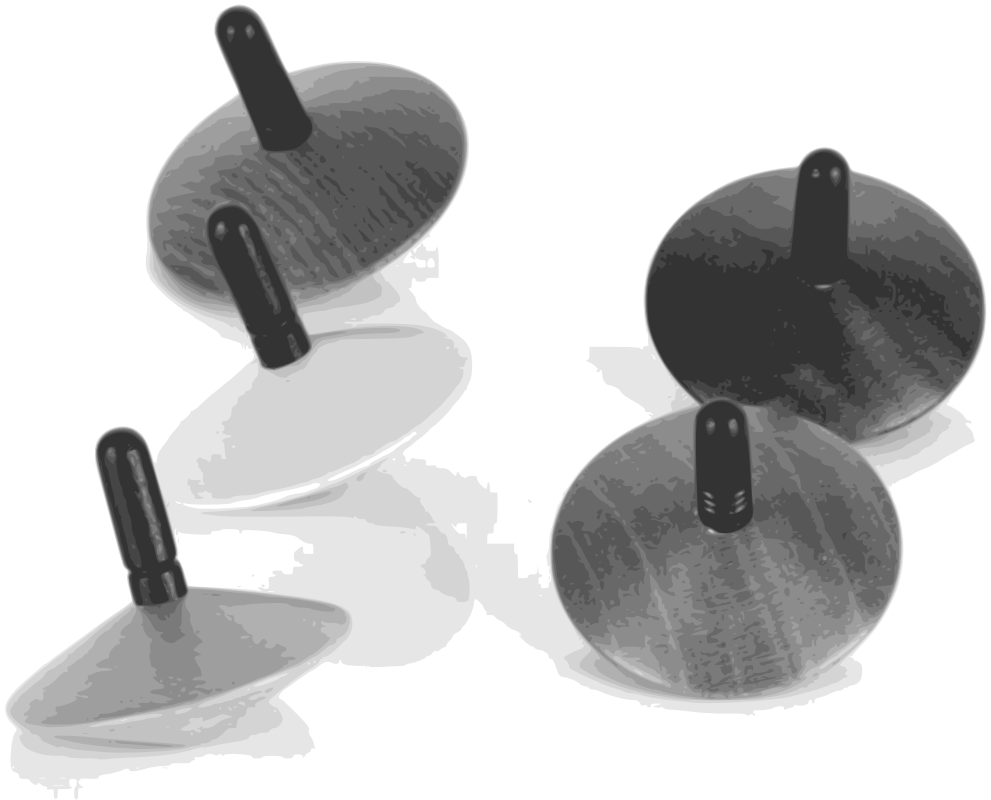
In conclusion, highly local and sizable (up to several hundreds of Hz) discontinuities in off-resonance have been found in the human breast at ultrahigh field, making the diffusion-weighted imaging of these regions, where most breast tumors grow, exceptionally challenging. A high-resolution off-resonance map allows integration of local

ΔB_0 discontinuities at tissue interfaces to better describe image distortion at those interfaces. Though distortion correction using low-resolution off-resonance maps corrects most of the distortions, alignment at the edges of glandular tissue greatly benefits from high-resolution distortion correction. Consequently, using off-resonance maps of a resolution higher than the measured EPI scans improves the conformity between images corrected for EPI distortions and a high-bandwidth reference. This ensures distortion-corrected DWI scans spatially match to clinical DCE images, which facilitates multi-parametric heterogeneity assessment.

References

1. Woodhams R, Matsunaga K, Kan S, Hata H, Ozaki M, Iwabuchi K, Kuranami M, Watanabe M, Hayakawa K. ADC mapping of benign and malignant breast tumors. *Magn Reson Med Sci* 2005;4(1):35-42.
2. Sharma U, Danishad KKA, Seenu V, Jagannathan NR. Longitudinal study of the assessment by MRI and diffusion-weighted imaging of tumor response in patients with locally advanced breast cancer undergoing neoadjuvant chemotherapy. *NMR Biomed* 2009;22(1):104-113.
3. Schmitz AMT, Loo CE, Wesseling J, Pijnappel RM, Gilhuijs KGA. Association between rim enhancement of breast cancer on dynamic contrast-enhanced MRI and patient outcome: impact of subtype. *Breast Cancer Res Treat* 2014;148(3):541-551.
4. Chan HM, van der Velden BHM, Loo CE, Gilhuijs KGA. Eigentumors for prediction of treatment failure in patients with early-stage breast cancer using dynamic contrast-enhanced MRI: a feasibility study. *Phys Med Biol* 2017;62(16):6467-6485.
5. An YY, Kim SH, Kang BJ. Differentiation of malignant and benign breast lesions: Added value of the qualitative analysis of breast lesions on diffusion weighted imaging (DWI) using readout segmented echo-planar imaging at 3.0 T. *PLoS One* 2017;12(3).
6. Fan M, He T, Zhang P, Zhang J, Li LH. Heterogeneity of Diffusion-Weighted Imaging in Tumours and the Surrounding Stroma for Prediction of Ki-67 Proliferation Status in Breast Cancer. *Sci Rep* 2017;7.
7. Stejskal EO, Tanner JE. Spin Diffusion Measurements: Spin Echoes in the Presence of a Time-Dependent Field Gradient. *J Chem Phys* 1965;42(1):288-+.
8. Jezzard P, Balaban RS. Correction for Geometric Distortion in Echo-Planar Images from B-0 Field Variations. *Magn Reson Med* 1995;34(1):65-73.
9. Hancu I, Lee SK, Hulsey K, Lenkinski R, Holland D, Sperl JI, Tan ET. Distortion correction in diffusion-weighted imaging of the breast: Performance assessment of prospective, retrospective, and combined (prospective plus retrospective) approaches. *Magn Reson Med* 2017;78(1):247-253.
10. Stacey-Clear A, McCarthy KA, Hall DA, Pile-Spellman E, White G, Hulka CA, Whitman GJ, Halpern EF, Kopans DB. Mammographically detected breast cancer: location in women under 50 years old. *Radiology* 1993;186(3):677-680.
11. Kim WH, Li M, Han W, Ryu HS, Moon WK. The Spatial Relationship of Malignant and Benign Breast Lesions with Respect to the Fat-Gland Interface on Magnetic Resonance Imaging. *Sci Rep* 2016;6.
12. Munger P, Crelier GR, Peters TM, Pike GB. An inverse problem approach to the correction of distortion in EPI images. *IEEE Trans Med Imaging* 2000;19(7):681-689.
13. Andersson JLR, Skare S, Ashburner J. How to correct susceptibility distortions in spin-echo echo-planar images: application to diffusion tensor imaging. *Neuroimage* 2003;20(2):870-888.
14. Schenck JF. The role of magnetic susceptibility in magnetic resonance imaging: MRI magnetic compatibility of the first and second kinds. *Med Phys* 1996;23(6):815-850.
15. Hopkins JA, Wehrli FW. Magnetic susceptibility measurement of insoluble solids by NMR: Magnetic susceptibility of bone. *Magn Reson Med* 1997;37(4):494-500.
16. Bouwman JG, Bakker CJG. Alias subtraction more efficient than conventional zero-padding in the Fourier-based calculation of the susceptibility induced perturbation of the magnetic field in MR. *Magn Reson Med* 2012;68(2):621-630.
17. Boer VO, Luttje MP, Luijten PR, Klomp DWJ. Requirements for static and dynamic higher order B0 shimming of the human breast at 7 T. *NMR Biomed* 2014;27(6):625-631.
18. Paige CC, Saunders MA. LSQR: An Algorithm for Sparse Linear Equations and Sparse Least Squares. *Acm T Math Software* 1982;8(1):43-71.
19. Zijlstra F, Bouwman JG, Braskute I, Viergever MA, Seevinck PR. Fast Fourier-based simulation of off-resonance artifacts in steady-state gradient echo MRI applied to metal object localization. *Magn Reson Med* 2017;78(5):2035-2041.

20. Lagarias JC, Reeds JA, Wright MH, Wright PE. Convergence properties of the Nelder-Mead simplex method in low dimensions. *Siam J Optimiz* 1998;9(1):112-147.
21. Otsu N. A threshold selection method from gray-level histograms. *IEEE transactions on systems, man, and cybernetics* 1979;9(1):62-66.
22. Gonzalez RC, Woods RE, Eddins SL. *Digital Image Processing Using MATLAB*. New Jersey: Pearson Prentice Hall; 2004.
23. Klein S, Staring M, Murphy K, Viergever MA, Pluim JPW. elastix: A Toolbox for Intensity-Based Medical Image Registration. *IEEE Trans Med Imaging* 2010;29(1):196-205.
24. Dagher JC, Meyer FG. A joint acquisition-reconstruction paradigm for correcting inhomogeneity artifacts in MR echo planar imaging. *Conf Proc IEEE Eng Med Biol Soc* 2011;2011:3744-3750.
25. Mendez CA, Pizzorni Ferrarese F, Summers P, Petralia G, Menegaz G. DCE-MRI and DWI Integration for Breast Lesions Assessment and Heterogeneity Quantification. *International journal of biomedical imaging* 2012;2012:676808.
26. Gholipour A, Kehtarnavaz N, Scherrer B, Warfield SK. On the accuracy of unwarping techniques for the correction of susceptibility-induced geometric distortion in magnetic resonance Echo-planar images. *Conf Proc IEEE Eng Med Biol Soc* 2011;2011:6997-7000.
27. Irfanoglu MO, Walker L, Sammet S, Pierpaoli C, Machiraju R. Susceptibility distortion correction for echo planar images with non-uniform B-spline grid sampling: a diffusion tensor image study. *Med Image Comput Comput Assist Interv* 2011;14(Pt 2):174-181.



Untangling the diffusion signal using the phasor transform



Based on:

M.J. van Rijssel, M. Froeling, A.L.H.M.W. van Lier, J.J.C. Verhoeff, J.P.W. Pluim; Untangling the diffusion signal using the phasor transform, *submitted*

Abstract

Purpose

The phasor technique, which was recently proposed as a new approach in quantitative MRI, can discern different components of diffusion within one voxel. This enables exploration of its content for clinical insight. In this study we investigate the added value of this technique for fixed-diffusivity unmixing and fitting of the intravoxel incoherent motion (IVIM) model.

Methods

Images of a digital diffusion phantom were simulated at signal-to-noise ratios of 30, 50, 100 and infinity. Influence of wrong diffusivity values and the number of b-values on fixed-diffusivity unmixing was investigated and compared against a linear least squares (LLS) fit. Phasor-based IVIM fitting was compared against non-linear least squares and segmented methods in terms of accuracy and precision. The distributions of the parameter estimates of simulated data were compared against those obtained in-vivo (volunteer and glioblastoma patient).

Results

LLS with fixed-diffusivity unmixing slightly outperformed phasor unmixing in all tested scenarios. Phasor-based IVIM fitting resulted in more stable fits for IVIM parameters f and D : the precision was higher than those obtained with non-linear fits and the accuracy was comparable. The precision of the phasor-based maps was better than maps calculated with the segmented method for a lower amount of b-values.

Conclusion

Although using a phasor-based approach for fixed-diffusivity unmixing does not yield more stable estimates, there can be a benefit for IVIM fitting. By using the geometrical properties of phasor space as additional knowledge, the IVIM fitting routine developed in this work produced more stable parameter maps than traditional methods.

5.1 Introduction

An exponential signal decay is characterized by its lifetime, the rate at which the signal decays. Such a decay curve can be represented by a phasor representation, which was developed in the field of optical microscopy for ingenious separation of fluorescent dyes with different lifetimes (1-3). Recently, Vergeldt *et al.* proposed the use of phasor representation for multi-component separation of decaying signals in quantitative MRI (4). In general, the phasor representation shows the position of an exponential decay curve in phasor space, which is determined by its lifetime, or a combination of lifetimes. Mono-exponential decay curves are represented on a semicircle, with components possessing a short lifetime on the right and components with a long lifetime on the left of this semicircle. Inversely, from the position in phasor space the lifetime of components can be estimated.

Multi-exponential decay curves, which can be regarded as mixtures of mono-exponential decay curves, are represented in the area enclosed by the single-exponential semicircle in phasor space. Bi-exponential decay curves are found on the line segment connecting their two base components, the position on this line is determined by the weighting between the components. For triple-exponential decay curves are found inside the triangle defined by their three base components, etc. These mixed signals can be 'unmixed' from the sum signal into fractional contributions up to a maximum of three components while fixing the lifetimes for those components across the dataset (5). This kind of analysis has been shown to have superior signal-to-noise characteristics when compared to conventional fitting approaches (6).

The decay signal from diffusion weighted scans has been intensively studied and consequently the field has come up with a plethora of models to describe it, ranging from complex models based on physical descriptions of diffusing water molecules to relatively simple mathematical descriptions of the measured signal (7). In most diffusion datasets there will be more than three components or even a (semi-)continuous distribution of decay rates underlying the measured signal (8,9). Projection of a diffusion dataset into phasor space provides a two-dimensional visualization of the decay components present, without assuming a model to describe the data. While this is a limited and qualitative way of visualizing a rich dataset, it provides a global overview and may be useful in detecting anomalies, potentially related to pathology, in a fast way.

Vergeldt *et al.* applied the phasor representation and signal unmixing to an in-vivo diffusion dataset of the human brain, with promising results (4). The fraction maps generated with phasor unmixing may be valuable in a clinical setting or as a starting point or input data for complex biophysical models. Though the phasor approach to unmixing of diffusion signals is simple and fast, it only allows for the unmixing of at most three signals with known diffusion values. The same fraction maps can be obtained by a simple linear system inversion, but since the phasor transform effectively involves a noise reduction step by selecting the lowest non-zero frequency, the generated maps are expected to have a higher signal-to-noise ratio (SNR). Currently, the robustness of both methods against noise and misplacement of the base vertices is unknown.

The phasor space may also be of use when fitting a more complex model. Recent works have shown that the use of intravoxel incoherent motion (IVIM) model fitting is valu-

able for brain tumor characterization or when discerning brain tumor progression from pseudoprogession or radionecrosis (10-13). The IVIM model is a bi-exponential model with a diffusion component and a pseudodiffusion or perfusion component (14). Estimation of this model is often challenging, since different combinations of parameters can yield model fits of comparable quality (15). A popular approach to circumvent this instability is a two-stage linear approach, often referred to as segmented fitting (16). This method, however, is prone to bias in parameter estimates (17). Since the IVIM model is bi-exponential, the phasor transform might be of use in fitting this model, more explicitly by exploiting the property that bi-exponential curves end up on the line connecting the two base components. This allows reduction of the number of free parameters by two, which might yield more stable fitting results.

The present work investigates the usefulness of the phasor transform for both a global visualization of the decay rates in a diffusion dataset and for fitting decay models. We test the hypothesis that using the phasor transform yields more stable fraction and parameter maps in both fixed-diffusivity unmixing and IVIM model fitting. The influence of noise, component misplacement and sampling on the accuracy of phasor unmixing are tested in a digital phantom. The performance of phasor unmixing is compared against that of linear unmixing as a benchmark. A phasor-based IVIM fitting routine is developed and compared against both classical nonlinear fitting and linear segmented fitting in terms of accuracy and precision. The results of these simulations are compared to those obtained in a healthy volunteer. As a proof-of-principle, both the global visualization and IVIM fitting results are demonstrated in a biopsy-proven glioblastoma patient.

5.2 Theory

5.2.1 Phasor transform and decay rate estimation

In this section we will provide a brief overview of the phasor representation. Additionally, since non-equidistant sampling across b-values is very common in diffusion datasets, we will add an analytical description of phasor unmixing in case of non-equidistant sampling (1-3). This improves the general applicability of the phasor toolkit.

The phasor transform \mathcal{P} is defined by taking the Fourier transform of a signal s and dividing it by the sum of the same signal for normalization: $\mathcal{P}(s(t)) = \frac{\mathcal{F}(s(t))}{\int s(t)dt}$. If the input is an exponential function of time t with lifetime τ , $s(t) = e^{-t/\tau}$, the Fourier transform at frequency ω is the Lorentz function: $S(\omega) = \frac{1}{1+j\omega\tau}$, with j the unit imaginary number. Plotting the real part of this function against the imaginary part for a fixed frequency ω for all possible lifetimes τ produces a semicircle with radius 0.5 and center (0.5, 0). Inversely, the decay rate of a signal can be estimated from its position in phasor space by inverting the Lorentz function: $\tau = \frac{j(S-1)}{S\omega}$.

In the case of discrete equidistant sampling, the sampling rate will influence the appearance of the single-exponential semi-circle, deforming it into a semi-ellipse. This phenomenon has been described by Fereidouni *et al.* for retrospectively binned exponential decay in the context of optical microscopy (18). They provide an analytical

description of this ellipse as a function of frequency, ω , and the number of measured samples or bins, U :

$$S(\omega, U) = \frac{\sum_{u=0}^{U-1} (e^{-\frac{u}{\tau} \frac{T}{U}} (1 - e^{-\frac{1}{\tau} \frac{T}{U}}) \tau) e^{jn\omega(u+\frac{1}{2})\frac{T}{U}}}{\sum_{u=0}^{U-1} e^{-\frac{u}{\tau} \frac{T}{U}} (1 - e^{-\frac{1}{\tau} \frac{T}{U}}) \tau} = \frac{e^{\frac{jnT\omega}{2U}} (e^{\frac{T}{U\tau}} - 1)}{e^{\frac{T}{U\tau}} - e^{\frac{jnT\omega}{U}}} = \frac{\sinh(\frac{T}{2U\tau})}{\sinh(\frac{1-jn\omega T}{2U\tau})} \quad (5.1)$$

with u the bin index, n the harmonic number, and T the total sampling duration. They also describe a rotation of the deformed semi-circle with decreasing U , which is due to their choice of the zero time point. For their case each bin runs from $t=(n-1)T$ to $t=nT$, which is a useful choice since photons are sampled continuously and retrospectively binned. In diffusion MRI, diffusion decay is only sampled at the chosen b -values and not in between. Consequently, we simply consider a discrete Fourier transform of a discretely sampled exponential decay divided by the discrete sum of the same signal, i.e. the discrete phasor transform:

$$S(\omega, U) = \frac{\sum_{u=0}^{U-1} e^{-\frac{u}{\tau} \frac{T}{U}} e^{jn\omega u \frac{T}{U}}}{\sum_{u=0}^{U-1} e^{-\frac{u}{\tau} \frac{T}{U}}} = \frac{e^{\frac{T}{U\tau}} - 1}{e^{\frac{T}{U\tau}} - e^{\frac{jnT\omega}{U}}} \quad (5.2)$$

This describes a semi-ellipse like in the work of Fereidouni *et al.*, but the rotation is no longer observed. An example of ellipse deformation due to discrete sampling can be seen in Figure 5.1B, which schematically shows the phasor plot of the single-exponential discretely sampled signals shown in Figure 5.1A. Since we know the analytical description of the single-exponential semi-ellipse, the decay rate can be found from the position in phasor space by inversion:

$$\tau = \frac{T}{U(2j\pi + \ln\left(\frac{Se^{\frac{jnT\omega}{U}} - 1}{S-1}\right))} \quad (5.3)$$

Additionally, Figure 5.1B shows the influence of diffusion kurtosis on the representation of a signal phasor space (19). Since signals that have nonzero kurtosis are not single-exponentials, they are not represented on the semi-ellipse. Instead, signals with positive kurtosis are represented in the area enclosed by the semi-ellipse, while signals with negative kurtosis are represented above it.

When sampling is discrete and non-equidistant, as is often the case for b -values in diffusion datasets, the single-exponential semi-ellipse will deform in an irregular way defined by the sampling pattern. This is not of concern when transforming data into phasor space or when determining the position of a decay rate on the circle, since one can simply apply the phasor transform as defined. Though estimating the decay rate of a non-equidistantly sampled signal based on its position in phasor space has become nontrivial, this can be accounted for numerically.

5.2.2 Signal mixing in phasor space

When applying the continuous phasor transform to a mixture m of single exponentials:

$$m(t) = \sum_{p=1}^P a_p e^{\frac{-t}{\tau_p}} = \sum_{p=1}^P a_p s(\tau_p, t) \quad (5.4)$$

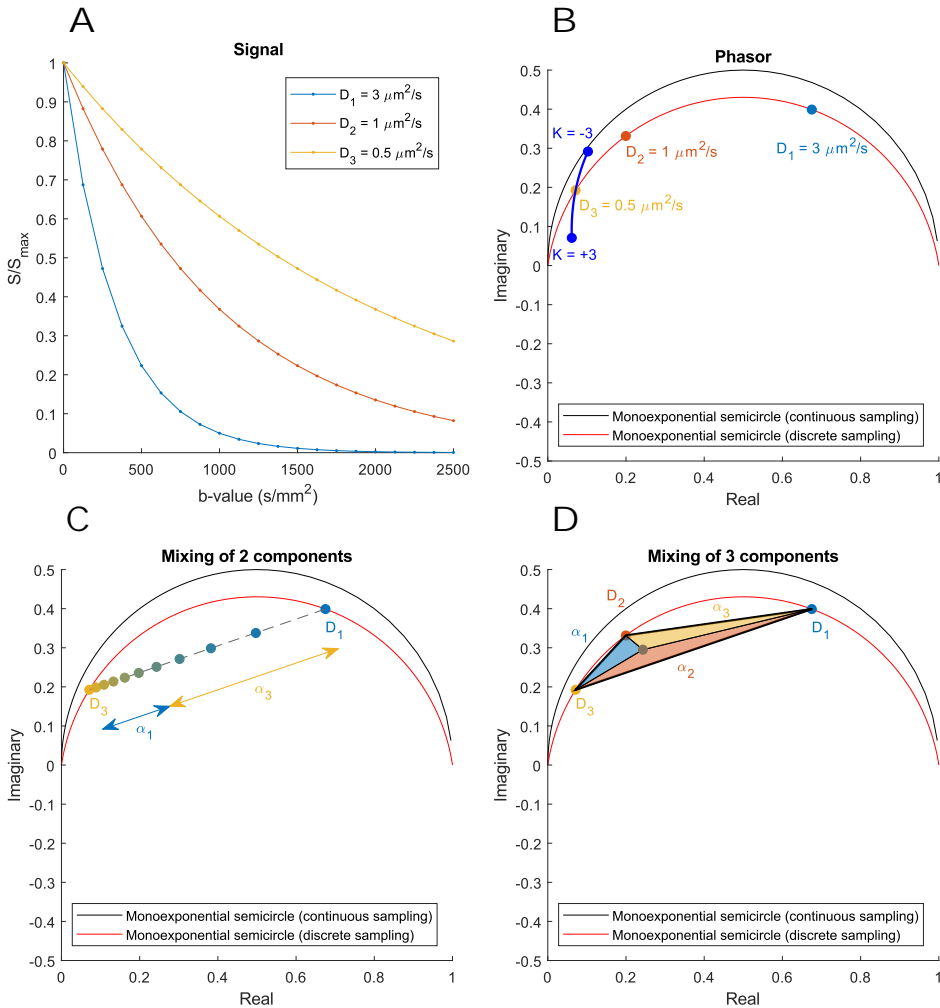


Figure 5.1: A: Simulated signal curves for three diffusivity values D , acquired using 21 equally spaced b -values between 0 and 2500 s/mm^2 . B: Schematic phasor plot that indicates the position in phasor space of each of the curves in A using the same color scheme. The influence of diffusion kurtosis K was added using numerical simulations. C: Schematic phasor plot that shows the principle of 2-component mixing. The position of bi-exponential decay curves in phasor space is on the line connecting the positions of the two pure components. The dots on the line indicate fraction increments of 10%. The colored arrows indicate phasor fraction α for a mixed signal with 60% component 1 and 40% component 2. D: Schematic phasor plot that shows the principle of 3-component mixing. The position of triple-exponential decay curves in phasor space is inside the triangle connecting the positions of the three pure components. The colored triangles indicate phasor fractions α for a mixed signal with 40% component 1, 40% component 2 and 20% component 3.

with τ_p the lifetime of the p-th component contributing to the total signal with fraction a_p , the transformed signal can be described as a combination of the phasor transform of each single exponential:

$$M(\omega) = \sum_{p=1}^P \alpha_p S(\tau_p, \omega) \quad (5.5)$$

with M the phasor transform of the multi-exponential signal m and the weighting of the p-th component in phasor space, α_p , depending on the weights of all components in the time domain, a , and their associated decay rates, τ :

$$\alpha_p = \frac{a_p \tau_p}{\sum_{p'=1}^P a_{p'} \tau_{p'}} \quad (5.6)$$

Graphically, this means that a mixed signal containing two components (i.e. bi-exponential decay) is located on a line connecting the locations of the two pure components in phasor space (20). The location of the signal on the line is determined by the weight α_p . Analogously, mixtures of more components are located inside a polygon defined by the pure component vertices. An example of this process is shown in Figures 5.1C and 5.1D for two and three components respectively. Note that this useful property of phasor space enables unmixing into the original signal fractions.

In case of discrete sampling the mixing properties above still hold, but the weights of the components in phasor space now depend on the sampling pattern:

$$\alpha_p = \frac{a_p \sum_{u=0}^{U-1} e^{-\frac{t_u}{\tau_p}}}{\sum_{p'=1}^P a_{p'} \sum_{u=0}^{U-1} e^{-\frac{t_u}{\tau_{p'}}}} \quad (5.7)$$

with u the sample index, U the total number of samples, t_u the time at which the u -th sample was measured, τ_p the lifetime of the p-th component, a_p the signal fraction of the p-th component and P the total number of single-exponential components. This is a very general description that holds for all possible sampling strategies. For equidistant sampling, i.e. $t_u = \frac{uT}{U}$, with T the total sampling duration, the expression for the weights in phasor space can be simplified, since the sum over all sampling points can be analytically evaluated:

$$\sum_{u=0}^{U-1} e^{-\frac{uT}{U\tau}} = \frac{e^{-\frac{T}{\tau}}(e^{\frac{T}{\tau}} - 1)}{1 - e^{-\frac{T}{\tau}}} \quad (5.8)$$

It can also be seen that when $U \rightarrow \infty$, the expression for the weights converges to the case of continuous sampling (Equation 5.6):

$$\alpha_p = \lim_{U \rightarrow \infty} \frac{a_p \sum_{u=0}^{U-1} e^{-\frac{uT}{U\tau_p}}}{\sum_{p'=1}^P a_{p'} \sum_{u=0}^{U-1} e^{-\frac{uT}{U\tau_{p'}}}} = \lim_{U \rightarrow \infty} \frac{a_p e^{\frac{T}{U\tau_p}}}{(e^{\frac{T}{U\tau_p}} - 1) \sum_{p'=1}^P \frac{a_{p'} e^{\frac{T}{U\tau_{p'}}}}{(e^{\frac{T}{U\tau_{p'}}} - 1)}} = \frac{\alpha_p \tau_p}{\sum_{p'=1}^P \alpha_{p'} \tau_{p'}} \quad (5.9)$$

5.2.3 Phasor unmixing

Mixtures of signals containing up to three components can be unmixed using phasor unmixing (5). Treating the real and imaginary axes separately and enforcing that the sum of all components is 1, unmixing three components can be achieved by first solving:

$$\begin{cases} \text{Re}(M) = \alpha_1 \text{Re}(S_1) + \alpha_2 \text{Re}(S_2) + \alpha_3 \text{Re}(S_3) \\ \text{Im}(M) = \alpha_1 \text{Im}(S_1) + \alpha_2 \text{Im}(S_2) + \alpha_3 \text{Im}(S_3) \\ \alpha_1 + \alpha_2 + \alpha_3 = 1 \end{cases} \quad (5.10)$$

with S_p the phasor transform (i.e. phasor coordinates) of signal s_p with corresponding phasor fraction α_p and M the phasor transform of the mixed signal. The solution of Equation 5.10 can be written in the form:

$$\begin{cases} \alpha_1 = \frac{\text{Im}(M)(\text{Re}(S_2)-\text{Re}(S_3))+\text{Im}(S_2)(\text{Re}(S_3)-\text{Re}(M))+\text{Im}(S_3)(\text{Re}(M)-\text{Re}(S_2))}{\text{Im}(S_1)(\text{Re}(S_2)-\text{Re}(S_3))+\text{Im}(S_2)(\text{Re}(S_3)-\text{Re}(S_1))+\text{Im}(S_3)(\text{Re}(S_1)-\text{Re}(S_2))} \\ \alpha_2 = \frac{\text{Im}(M)(\text{Re}(S_1)-\text{Re}(S_3))+\text{Im}(S_1)(\text{Re}(S_3)-\text{Re}(M))+\text{Im}(S_3)(\text{Re}(M)-\text{Re}(S_1))}{\text{Im}(S_1)(\text{Re}(S_2)-\text{Re}(S_3))+\text{Im}(S_2)(\text{Re}(S_3)-\text{Re}(S_1))+\text{Im}(S_3)(\text{Re}(S_1)-\text{Re}(S_2))} \\ \alpha_3 = \frac{\text{Im}(M)(\text{Re}(S_1)-\text{Re}(S_2))+\text{Im}(S_1)(\text{Re}(S_2)-\text{Re}(M))+\text{Im}(S_2)(\text{Re}(M)-\text{Re}(S_1))}{\text{Im}(S_1)(\text{Re}(S_2)-\text{Re}(S_3))+\text{Im}(S_2)(\text{Re}(S_3)-\text{Re}(S_1))+\text{Im}(S_3)(\text{Re}(S_1)-\text{Re}(S_2))} \end{cases} \quad (5.11)$$

which provides the phasor fraction, α_p , for each component. To solve for signal fractions, a_p , we have to invert Equation 5.7 for three components ($P=3$):

$$\begin{cases} a_1 = \frac{\alpha_1 E_2 E_3}{E_1 E_2 + \alpha_1 (E_2 E_3 - E_1 E_2) + \alpha_2 (E_1 E_3 - E_1 E_2)} \\ a_2 = \frac{\alpha_2 E_1 E_3}{E_1 E_2 + \alpha_1 (E_2 E_3 - E_1 E_2) + \alpha_2 (E_1 E_3 - E_1 E_2)} \\ a_3 = 1 - a_1 - a_2 \end{cases} \quad (5.12)$$

with E_p defined as:

$$E_p = \sum_{u=0}^{U-1} e^{-\frac{t_u}{T_p}} \quad (5.13)$$

Note that though the sum of all components is set to be 1 in Equation 5.10, each individual component is not restricted. Consequently, solutions for both a_p and α_p outside the range $[0, 1]$ can be returned.

5.2.4 Phasor-based IVIM fitting

The geometric properties of phasor space can be exploited to reduce the number of free parameters when fitting an IVIM model. The IVIM model assumes a sum of two single -exponential signal components (14):

$$S(b) = S_0((1 - f) e^{-bD} + f e^{-bD^*}) \quad (5.14)$$

with S the measured signal, b the b -value, S_0 the baseline MR signal, D the diffusion coefficient, D^* the pseudodiffusion coefficient and f its associated fraction. In a classical non-linear least squares fitting strategy, one has to estimate values for all four parameters of the model: S_0 , D , D^* and f .

By exploiting the geometric properties of bi-exponential signals in phasor space, the number of free parameters can be reduced to one, either D or D^* . As outlined in the beginning of this section, estimating S_0 is bypassed by transforming the data into phasor space, since the phasor transform is normalized by definition. As is shown in Figure 5.1C, all bi-exponential signals are located on a line connecting the locations of the two pure components in phasor space. Consequently, if one of the pure diffusivities (D or D^*) is chosen as the free parameter and estimated using an iterative approach, the other diffusivity (D^* or D) and the fraction (f) can be deduced using this property and a projection onto the single-component semi-ellipse. Assume, without loss of generality, that the free parameter is D^* . The other diffusivity (D) and the fraction (f) can be found by drawing a straight line from the location of D^* on the semi-ellipse through the location of measured signal (L) in phasor space. The intersection of this line with the semi-ellipse on the other side of L gives us D . Subsequently, f can be found by unmixing as detailed in the previous section.

5.3 Methods

5.3.1 Phasor and unmixing

5.3.1.1 Transforming data into phasor space

Phasor transformation of diffusion datasets was performed in MATLAB R2017b (The MathWorks, Natick, Massachusetts, USA). First, data was sorted such that for every voxel location a sequence of data points with increasing diffusion weighting originated. Second, these sequences were transformed by applying a 1D inverse discrete Fourier transform using a fast Fourier transform algorithm (MATLAB's `ifft` function) along the diffusion-encoding dimension. The resulting spectrum was divided by the sum signal for normalization. The phasor coordinates of each voxel were then determined by the real and imaginary components of the result at the lowest positive and non-zero frequency (i.e. the lowest harmonic).

5.3.1.2 Phasor unmixing

As outlined in the Theory section, the fractions of each pure component determines a voxel's coordinates in phasor space. Given the coordinates of these base components (component vertices) in phasor space, the relative signal fractions of up to three components can be estimated using phasor unmixing. A phasor unmixing routine was implemented in MATLAB that provides estimates for each fraction on a voxel-wise basis, by taking each voxel's coordinates in phasor space and the coordinates of the component vertices and applying Equations 5.11-5.13 (see also Figure 5.1D).

5.3.1.3 Linear unmixing

Phasor unmixing was compared against the benchmark of linear unmixing. In linear unmixing, the fractions are calculated by directly solving the system of linear equations presented in Equation 5.4 for all fractions a_p , while keeping all associated exponentials fixed. The linear system was solved using MATLAB's `mldivide` function.

5.3.2 IVIM model fitting

Three different algorithms to fit the IVIM model (Equation 5.14) parameters D , D^* and f were compared: nonlinear fitting, segmented fitting and phasor-based fitting. The

nonlinear fitting was performed twice; once with and once without constraints on the fraction f .

5.3.2.1 Nonlinear fitting

Nonlinear IVIM fitting was implemented using MATLAB's implementation of a trust-region-reflective least squares method. S_0 , D , D^* and f were estimated using this solver and initialized at $0.1 \mu\text{m}^2/\text{s}$, $15 \mu\text{m}^2/\text{s}$ and 0.5 . D was constrained to be nonnegative, D^* was constrained to be larger than or equal to $2.5 \mu\text{m}^2/\text{s}$, f was either unconstrained or constrained to be between 0 and 1 . Additionally, D was constrained to be smaller than D^* ; the values of the parameters were switched in case the algorithm returned a result where $D > D^*$ and the value for f was adjusted accordingly.

5.3.2.2 Segmented fitting

In segmented fitting, estimation was done in two steps (16). In both steps, the fitted function was linearized by applying a log transform to the measured data. First, a single exponential was fitted to all data points from b -values higher than $300 \text{ s}/\text{mm}^2$. The perfusion component was considered to be negligible at b -values higher than this threshold, so D was estimated directly from this fit. Next, the fit from the previous step was subtracted from the entire measured signal (using all datapoints) and D^* was estimated by fitting a single exponential to the result. Finally, the fraction f was estimated from the difference between the measured signal and the fit at $b = 0$, sidestepping the need to fit S_0 .

5.3.2.3 Phasor-based fitting

Phasor-based IVIM fitting was implemented using the projection technique described in the Theory section. D^* was estimated iteratively, using MATLAB's implementation of a trust-region-reflective least squares method (21,22). D was deduced from phasor-based symmetry and projection, as outlined in the Theory section. An estimate for f was obtained by phasor unmixing. Estimating S_0 is bypassed since the phasor transform includes a signal normalization step (see Theory section). D^* was initialized at $15 \mu\text{m}^2/\text{s}$ and constrained to be nonnegative. As in the nonlinear fitting method, D was constrained to be smaller than D^* . A penalty term was added to the cost function to favor low fractions f (i.e. mono-exponential fits) for points close to the semicircle:

$$\text{cost} = \begin{cases} (\hat{y} - y)^2 + (\lambda f \left(1 - \frac{L}{L_0}\right))^2 & \text{for } L \leq L_0 \\ (\hat{y} - y)^2 & \text{otherwise} \end{cases} \quad (5.15)$$

with \hat{y} the current model prediction, y the measured signal normalized to the signal at $b=0$, f the IVIM pseudo diffusion fraction, L the Euclidian distance to the semicircle, L_0 the cutoff distance beyond which the extra penalty is zero and the scaling parameter λ . λ and L_0 were empirically set to $0.05 \text{ mm}^2/\text{s}$.

5.3.3 Digital phantom studies

5.3.3.1 Unmixing analysis

A digital phantom was constructed, consisting of three diffusivity values loosely based on values generally found in the human brain (23): 2.9 , 0.85 and $0.18 \mu\text{m}^2/\text{s}$ for D_1 , D_2

and D3 respectively. The phantom contains increasing fractions for each component, consisting of 11 discrete steps increasing from 0 to 1 in steps of 0.1. Since the sum of all fractions must be 1, 66 unique combinations of fractions are simulated in this way. Each combination was simulated 10.000 times for different noise instances.

Diffusion weighted images were simulated with 21 b-values equally spaced between 0 and 2500 s/mm². Gaussian noise was added to the complex signal resulting in four SNR levels of 30, 50, 100 and infinity (no noise added), where SNR is defined as average over standard deviation in the b = 0 image. Subsequently the magnitude of the signal was taken, leading to a Rician noise distribution (24).

The distribution of all simulated data in phasor space was visualized by creating two-dimensional histograms. These histograms divided phasor space into square bins of 1/300 by 1/300 mm⁴/s² and a color code was used to indicate the amount of voxels present in each bin. To improve visibility, a logarithmic color code scale was used.

To investigate the dependency on noise, phasor unmixing was performed and the generated reconstructions were compared to the ground truth fractions. To investigate the influence of misplacement of base-components on the semicircle, in the presence and in the absence of noise, the base-components were systematically misplaced. Each of three base components was varied such that the diffusivity values used during unmixing varied from 0.75*D_{true} - 1.25*D_{true} in steps of 0.05*D_{true}. For every offset, the median error as well as the 5%, 25%, 75% and 95% quartiles were calculated.

The dependency on b-value sampling was investigated by varying the number of b-values from 3 to 99. This experiment was only performed with an SNR of 30, since this is a more realistic number in clinical practice (25).

5.3.3.2 IVIM analysis

Numerical simulations were conducted to generate signals with D set to 0.7 and D* set to 10 μm²/s. 101 fractions f in the range 0 - 1 were simulated. Each fraction was repeated 5000 times with different Rician noise realizations at an SNR level of 30 at the b=0 image. We tested two different b-value sampling schemes ranging from 0 to 1000 s/mm², based on our in-vivo acquisition (see below). The full range of 15 simulated b-values was 0, 10, 20, 30, 40, 60, 100, 150, 200, 250, 300, 400, 600, 800, and 1000 s/mm². To investigate the influence of subsampling, the same simulations were performed with a subset of 6 b-values: 0, 30, 100, 250, 600, and 1000 s/mm².

The performances of the nonlinear, segmented and phasor-based fitting algorithms described above were compared on the simulated data. For every simulated fraction, the median error as well as the 25% and 75% percentiles in the estimated parameters were calculated. Additionally, to facilitate comparison with our in-vivo data, kernel-density estimated probability density functions (PDF) were calculated for parameters D and f at fraction levels closest to the levels that were found in the in-vivo data: 0.07 for gray matter and 0.05 for white matter. These PDFs indicate the distribution of parameter estimates around the true value.

Table 5.1: Overview of scan parameters per sequence. For every non-zero b-value, three orthogonal directions were acquired. Abbreviations: 3D – Three dimensional acquisition, T_1w – T_1 weighted, UGE – Ultrafast Gradient Echo, SENSE – Sensitivity Encoding, DW – Diffusion Weighted, SE – Spin Echo, EPI – Echo Planar Imaging.

Sequence	Healthy volunteer		Patient volunteer
	3D T_1w UGE	DW SE-EPI	DW SE-EPI
TR (ms)	8	8000	4378
TE (ms)	1.27	117	117
Resolution (mm ³)	1.0x1.0x1.0	2.5x2.5x2.5	2.5x2.5x2.5
b-values (s/mm ²)	-	0, 10, 20, 30, 40, 60, 100, 150, 200, 250, 300, 400, 600, 800, 1000, 1250, 1500, 1750, 2000, 2250, 2500	0, 10, 20, 30, 40, 60, 100, 150, 200, 250, 300, 400, 600, 800, 1000, 1250, 1500, 1750, 2000, 2250, 2500
Scan time (min)		10	5
Acceleration	UGE factor: 120 SENSE: 2 AP + 2 RL	EPI factor: 39 SENSE: 2.5 AP	EPI factor: 39 SENSE: 2.5 AP

5.3.4 In-vivo studies

5.3.4.1 Scanning protocol & initial processing

All experiments conducted were in accordance with the guidelines of the local ethical committee and, prior to the exams, informed consent was obtained from all volunteers. A brain scan was obtained from one healthy male volunteer, aged 29 years, using a 3T whole-body MR system (Ingenia; Philips, Best, The Netherlands). The scan protocol contained a T_1w ultrafast gradient echo as well as a diffusion scans with three orthogonal diffusion encoding directions and 21 b-values ranging from 0 to 2500 s/mm². The total acquisition time for the diffusion scan was around 10 minutes. A comparable diffusion weighted protocol with three orthogonal directions was added to the standard clinical protocol for one male biopsy-proven glioblastoma patient, aged 83, in the context of imaging for radiotherapy planning, but with a reduced feet-head coverage of 30 2.5 mm slices around the tumor to limit the scan time to approximately 5 minutes. Eight baseline scans with no diffusion weighting were acquired at regular intervals in between diffusion weighted scans to allow signal drift correction (26). Scan parameters per sequence are reported in Table 5.1. Additionally, from the standard clinical protocol the fluid attenuated inversion recovery (FLAIR) and late gadolinium enhancement (LGE) images were obtained.

Linear signal drift correction and correction for subject motion, eddy currents and echo-planar imaging (EPI) distortion was applied to all diffusion weighted scans using available routines in ExploreDTI v4.8.6 (27). Motion and distortion correction was

achieved by registering all diffusion scans to the T_1w scan, down sampled to the resolution of the diffusion weighted scans. Registration involved affine registration in all directions for motion correction and b-spline registration in the EPI direction for distortion correction using ExploreDTI's standard set of parameters. Probability masks based on the T_1w image for gray matter, white matter and cerebrospinal fluid (CSF) as well as a label image indicating tissue types were obtained from SPM's Computational Anatomy Toolbox segmentation tool v12.1 and subsequently down sampled to the resolution of the diffusion weighted scans (28). A brain mask was derived from the label image by selecting all voxels with a label corresponding to either CSF, white matter or gray matter. The brain mask was applied to all diffusion images prior to further analysis. For the healthy volunteer, masks of each tissue type were created from the probability maps by selecting voxels with a probability higher than 0.99. Finally, geometric averaging was applied to all diffusion scans.

5.3.4.2 Data analysis healthy volunteer

The nonlinear, segmented and phasor-based IVIM fitting algorithms described above were applied to the acquired data of the healthy volunteer. Only b-values of 1000 s/mm^2 and below were selected for the IVIM analysis. To compare the healthy in-vivo data with our simulations, kernel-density estimated PDFs were calculated for fitted parameters D and f inside the obtained gray and white matter masks. Parameter maps for all IVIM parameters were calculated for all fitting strategies. These maps were calculated using either all 15 b-values of 1000 s/mm^2 and below (0, 10, 20, 30, 40, 60, 100, 150, 200, 250, 300, 400, 600, 800, and 1000 s/mm^2) or a subset of 6 b-values (0, 30, 100, 250, 600, and 1000 s/mm^2).

5.3.4.3 Data analysis patient volunteer

Phasor analysis was performed on the data acquired from the glioblastoma patient, both on a reduced dataset containing all 15 b-values of 1000 s/mm^2 and below (c.f. healthy volunteer in previous section) and on the full dataset. On the phasor plot created using the full range of acquired b-values (0 – 2500 s/mm^2), a cluster of points was visible that was not seen on similar plots of healthy volunteers. This cluster was crudely delineated and the corresponding voxels were obtained.

5.4 Results

5.4.1 Unmixing

The phasor representation of the phantom data for the four simulated noise levels is shown in Figure 5.2 on a logarithmic color scale. Note that each of the 66 fraction combinations ended up in a unique location in phasor space. The spacing between increments in fraction was nonlinear and the effect of noise differed per component.

Due to an efficient implementation using fast Fourier transforms, applying the phasor transform and unmixing an entire simulation dataset containing 1.210.000 voxels and 21 b-values took less than 0.5 seconds on a desktop computer with a 3.50 GHz Intel Xeon E5-1620 v3 central processing unit and 32 gigabytes of random access memory. Linear unmixing was slightly faster in just over 0.3 seconds.

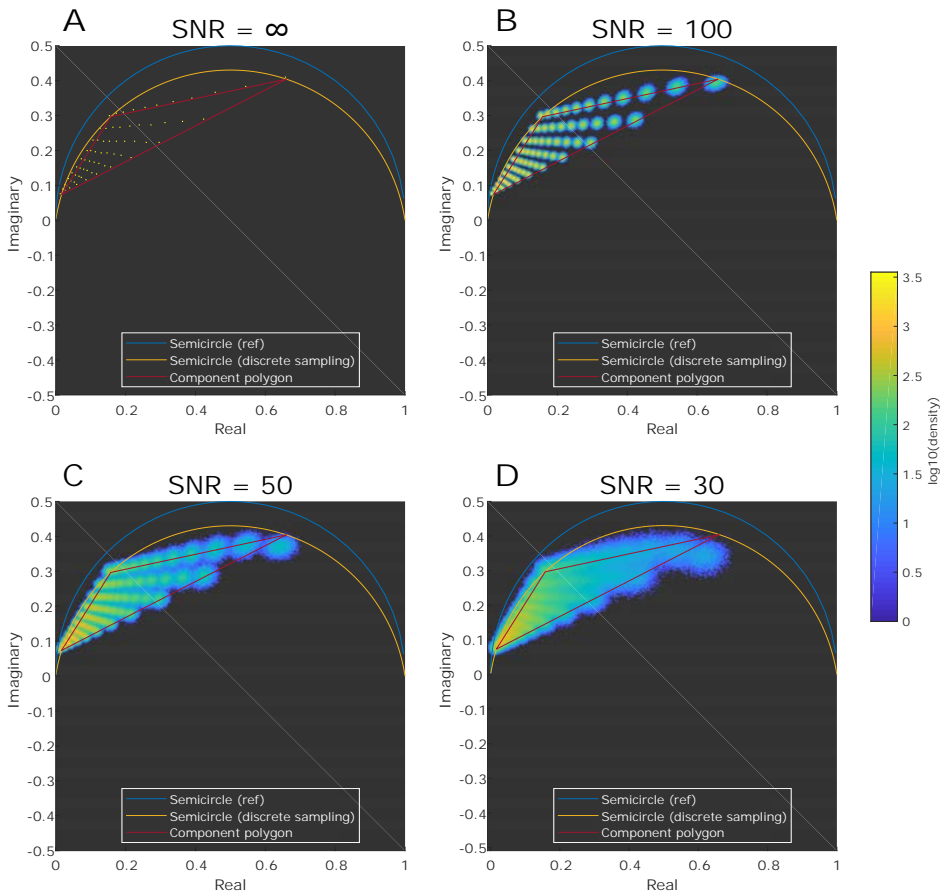


Figure 5.2: A: Phasor representation of simulated diffusion weighted images of a digital phantom consisting of three components with diffusivity values: $D_1 = 2.9$, $D_2 = 0.85$, $D_3 = 0.18 \mu\text{m}^2/\text{s}$. Each yellow dot corresponds to one of the 66 unique combinations of D_1 , D_2 and D_3 . B-D: Phasor representation of the same phantom, but each of the 66 combinations was simulated with 10,000 unique noise realizations such that the SNR in the simulated $b = 0$ image was 100, 50 or 30 as indicated. Abbreviation: SNR - Signal-to-Noise Ratio.

Figure 5.3A shows the accuracy and precision in the estimated signal fractions due to component misestimation for both phasor unmixing and linear unmixing. The noise-induced bias at SNR level 30 for components 1, 2 and 3 respectively was 0.016, -0.042 and 0.026 for phasor unmixing and 0.012, -0.039 and 0.027 for linear unmixing. Bias induced by component misestimation varied strongly depending on the misplaced component. The maximum interquartile range due to a 10% error in diffusivity at infinite SNR was 0.045. The maximum interquartile range due to noise without misplacement error was larger for SNR 50 and below (0.081 at SNR 50).

Figure 5.3B shows linear unmixing slightly outperforms phasor unmixing across the entire range when the number of b -values is varied. Both unmixing methods showed increased precision when the number of b -values is increased, especially when the number of b -values is low.

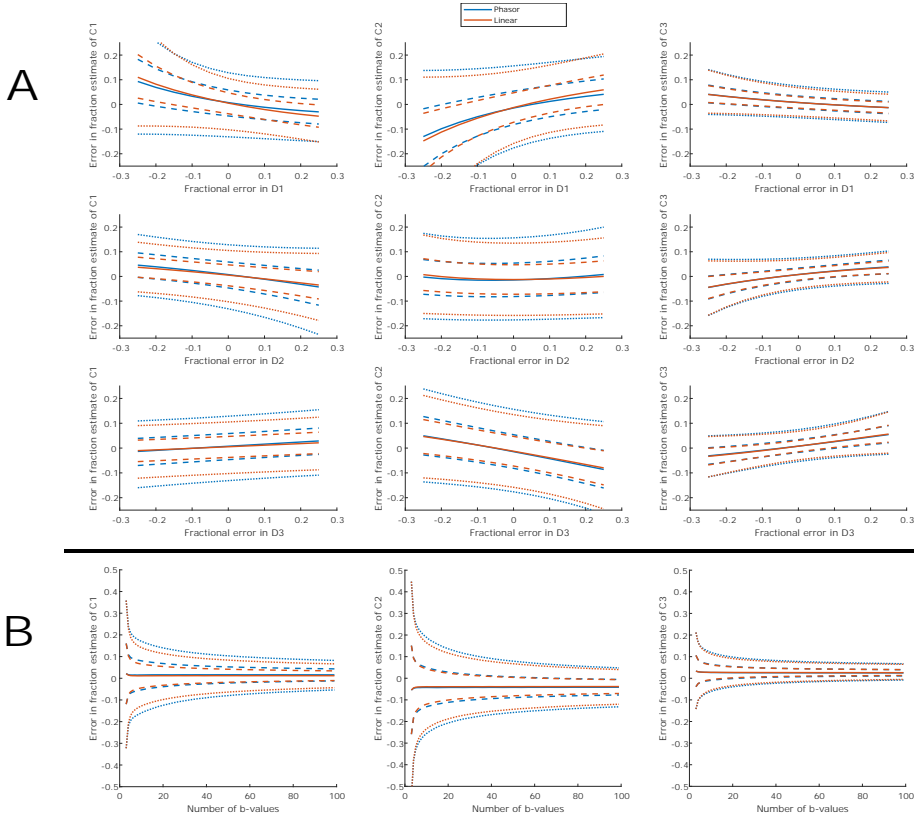


Figure 5.3: A: Influence of component vertex misplacement on the fraction estimation by both phasor unmixing and linear unmixing in a simulated dataset with SNR 30. For every row, the influence of the misplacement of one component's diffusivity ($D_1 - D_3$) on the fraction estimate of all components ($C_1 - C_3$) is investigated. The solid lines represent the median error, the dashed lines the 25% and 75% quantiles and the dotted lines the 5% and 95% quantiles. B: Influence of the number of b-values on the fraction estimation by both phasor unmixing and linear unmixing at an SNR-level of 30. Abbreviation: SNR - Signal-to-Noise Ratio.

5.4.2 IVIM fitting

The comparison of the nonlinear, segmented and phasor-based IVIM fitting methods on simulated data is presented in Figure 5.4 and the left panel of Figure 5.5. Figure 5.4 shows that for fractions f below 0.25 the phasor-based method had the highest precision for estimates of f and D : the interquartile range was roughly halved with respect to that of the segmented method, which was second-best. Accurately estimating D^* at low fractions f proved difficult for all methods.

Figure 5.5 shows the PDF of estimated values for f , D and D^* for both simulated and measured white matter and gray matter. Note that all simulation parameters were constant, so the distribution of estimated values is caused entirely by the added Rician noise. The simulation results for f and D showed that phasor-based fitting had a higher precision than both nonlinear and segmented methods. For the low number of b-values (6 instead of 15, dashed lines in Figure 5.5), the precision of the phasor-based

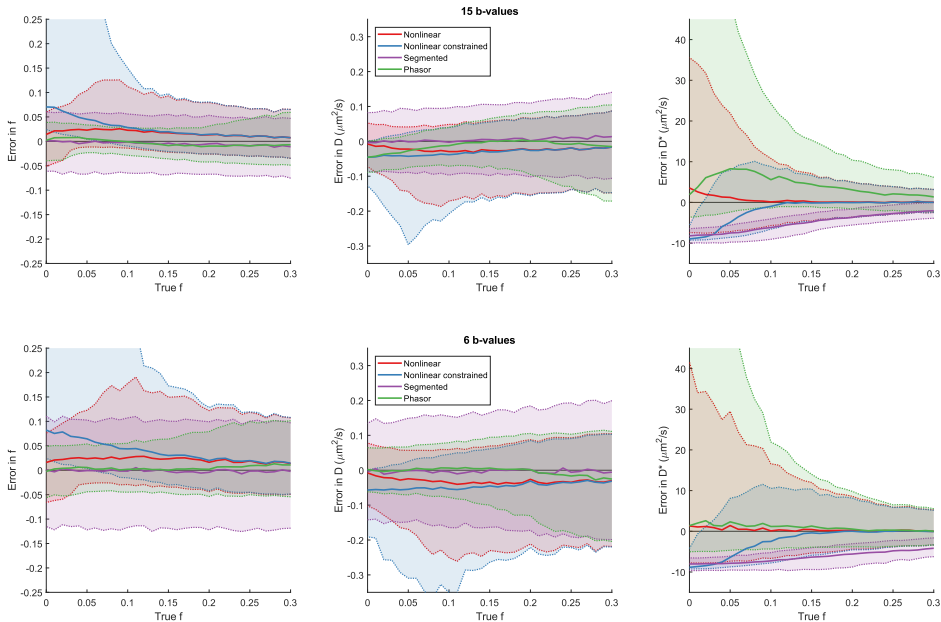


Figure 5.4: Comparison of IVIM fitting techniques on simulated data: non-linear least squares (red), constrained non-linear least squares (blue), segmented linear least square (purple) and phasor-based non-linear least square (green). The SNR level was 30, and the b-value sampling range was 0 - 1000 s/mm² for both experiments, but the number of b-values was varied: 15 b-values in the top panel and 6 b-values in the bottom panel. The solid lines represent the median error and the dotted lines the 5% and 95% quantiles. Shading was added to facilitate comparison of the spread in the errors. Abbreviations: IVIM - Intravoxel Incoherent Motion, SNR - Signal-to-Noise Ratio.

method was higher than that of the segmented method. In terms of accuracy, none of the tested methods was consistently the best, although both phasor and segmented outperformed the classical methods by avoiding a local minimum with f around 0.7 and an unfeasibly low value for D . The accuracies of the phasor-based and segmented methods were comparable. The simulation results for D^* showed that although the phasor-based method has the highest spread, it introduces the lowest amount of bias.

5.4.3 In-vivo results

The in-vivo results in Figure 5.5 show a similar distribution as the simulation results, although all distributions were slightly wider, most likely due to physiological variations in the imaged tissue included by the masks. The accuracy of the methods in-vivo is hard to assess since no gold standard is available, but similar shifts in peak positions between different fitting strategies were observed for the in-vivo results compared to the simulations. The phasor estimates had the lowest spread for all parameters, except for D in gray matter. A notable difference between the in-vivo and simulation results was the reduced influence of the amount of sampled b-values on the estimates of D .

Figure 5.6 shows parameter maps for all IVIM parameters of the healthy volunteer, comparing those calculated with 15 b-values to those calculated with 6 b-values. All

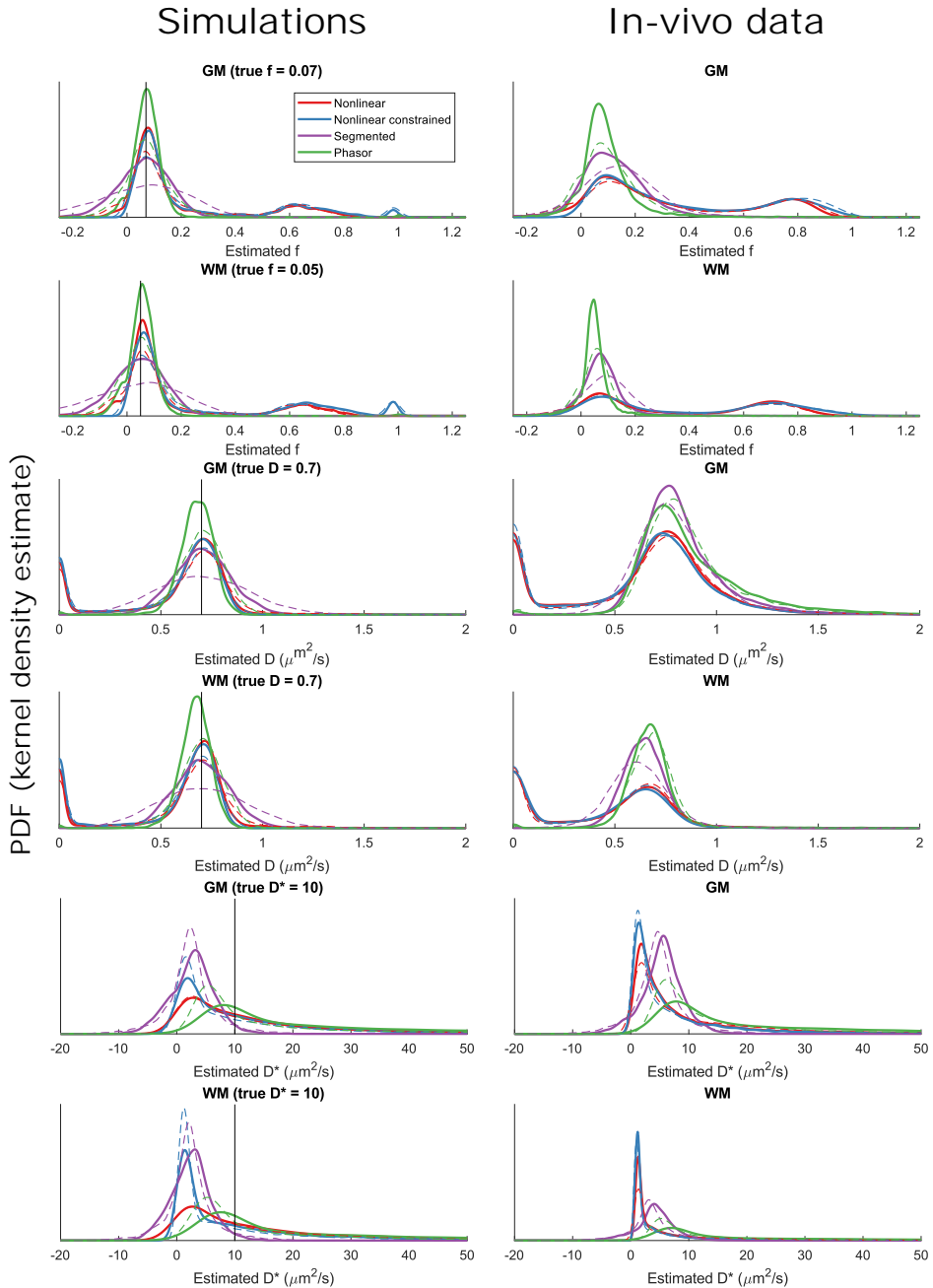


Figure 5.5: Probability density functions of estimated IVIM parameters f , D and D^* for all tested fitting techniques in both simulated and in-vivo measured white and gray matter. In the simulations the vertical lines indicate the true value of the estimated parameter. Solid lines are the results obtained using all measured 15 b -values, dashed lines are the results with a subset of 6 b -values. Abbreviations: GM - gray matter, WM - white matter.

f maps showed an increase in the number of physically implausible negative values when decreasing the number of b-values, except the map calculated with the nonlinear method constrained to the 0 – 1 range. These negative values were observed most often in central brain regions in white matter. The segmented method was the only method that returned negative values for D or D*. The D maps calculated with both nonlinear methods contained a lot of implausible low values that were not present in the maps calculated with the segmented or phasor-based method. The D map calculated with the segmented method and only 6 b-values contained a higher amount of noise than the same map calculated with the phasor method.

Figure 5.7 shows results obtained from the glioblastoma patient. In the phasor space corresponding to the full dataset (0 – 2500 s/mm²), a cluster of points, encircled in green, was observed that was not seen in healthy volunteers. The pixels corresponding to that cluster are indicated in green in the bottom left panel and roughly corresponded to hyperintense regions on the FLAIR image of the same patient. For reference, the Gross Tumor Volume (GTV) and Clinical Target Volume (CTV) are overlaid on the observed cluster, FLAIR and LGE images.

5.5 Discussion

5

This chapter aimed to investigate the benefit of using the phasor transform for both a global visualization of the decay rates present in a diffusion dataset and for fitting decay models. Global visualization allowed the fast identification of a cluster of voxels that roughly corresponded to the hyperintense region on the FLAIR image of a glioblastoma patient. Though the phasor transformation and unmixing allowed fast (sub-second) estimation of signal component fractions, there was no clear benefit of phasor unmixing when compared to linear unmixing in terms of accuracy or precision. Both methods were found to behave similarly with regard to the number of sampled b-values, noise levels and component misestimation. IVIM model fitting seemed to benefit from a phasor-based approach: it featured a better precision than nonlinear fitting methods and the number of sampled b-values influenced the outcome less than with segmented fitting.

Both component misestimation and the addition of Rician noise seem to cause a systematic bias in fixed-diffusivity unmixing. The number of b-values on the other hand, hardly influences the accuracy. The effect of Rician noise is most apparent for high fractions of D₁. Since D₁ corresponds to the fastest decay (the highest diffusivity) in the simulation corresponding to free water, this signal is the fastest to reach the noise floor, where due to the Rician noise distribution the average signal is offset from zero. In phasor space, this leads to an offset from the expected position. This effect can be appreciated in the right top corners of Figures 5.2 B-D, where the group of pixels corresponding to a pure D₁ signal deviates from its expected position on the semicircle. Note that this effect increases for decreasing SNR levels. The overall effect of Rician noise on the bias in fraction estimation is quite low, the absolute bias was always below 0.05. Additionally, as reported in Figure 5.3A, the bias induced by component misestimation was larger than the bias induced by Rician noise, even at small fractional errors and the lowest SNR level 30.

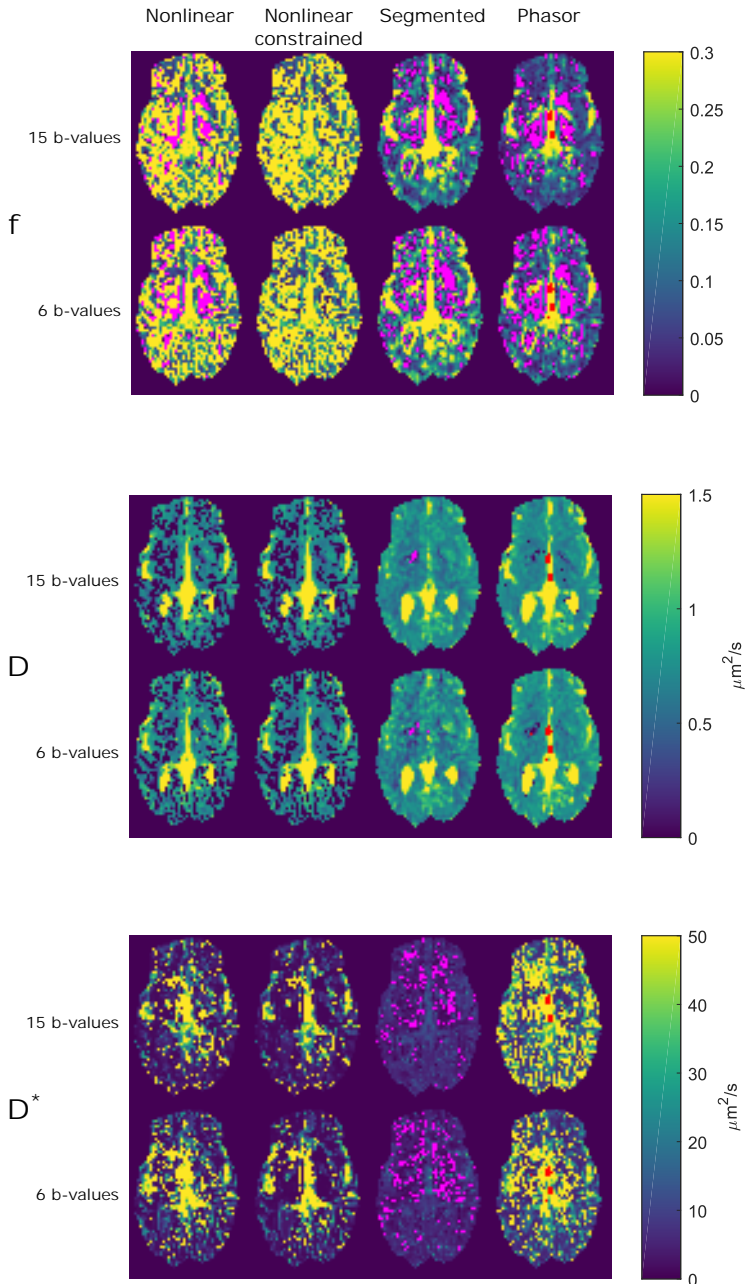


Figure 5.6: Comparison of IVIM fitting techniques on a diffusion dataset of a healthy volunteer with b-values between 0 and 1000 s/mm². For every parameter there are two rows of maps: the top row shows maps calculated with all 15 b-values, the bottom row shows maps calculated with a subset of 6 b-values. Red voxels indicate locations where the algorithm failed to find a solution. Magenta voxels indicate locations where the algorithm returned physically implausible negative values. Abbreviation: IVIM - Intravoxel Incoherent Motion.

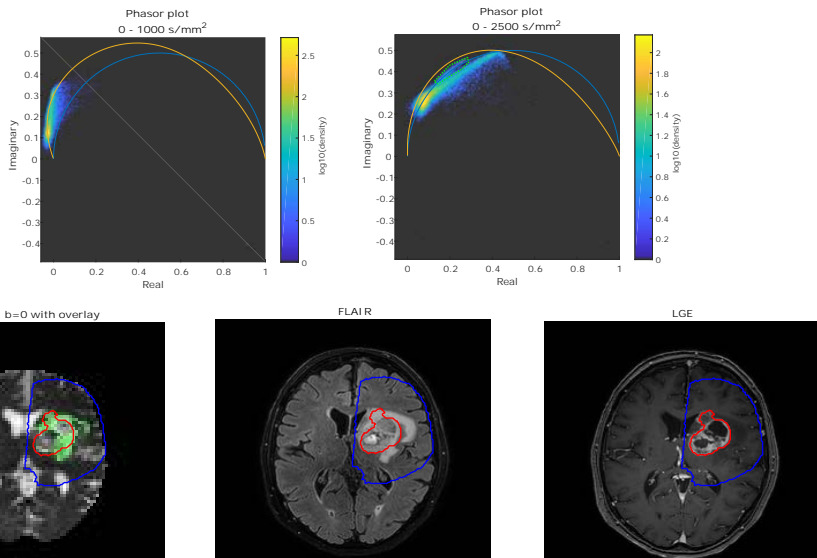


Figure 5.7: Phasor plots for 0 – 1000 and 0 – 2500 s/mm^2 as well as $b=0$ DWI, FLAIR and LGE images of a glioblastoma patient. A cluster of points (encircled in green) is visible on the phasor plot of 0 – 2500 s/mm^2 that was not seen in healthy volunteers. The corresponding voxels are indicated in the bottom left plot in green on top of the $b=0$ DWI. The region seems to correspond roughly to a hyperintense region on the FLAIR image (bottom middle). For reference, the GTV and CTV are overlaid on the DWI, FLAIR and LGE images. Abbreviations: CTV - Clinical Target Volume, DWI - Diffusion Weighted Imaging, FLAIR - Fluid Attenuated Inversion Recovery, GTV - Gross Tumor Volume, LGE - Late Gadolinium Enhancement

5

The precision of fraction estimation was affected mainly by the SNR level and the number of b -values. Component misestimation has a much smaller effect on precision of the fraction estimate: a 10% relative error in diffusivity caused a smaller interquartile error range, than adding Rician noise with an SNR of 50 or less. An increase in the amount of b -values causes an increase in estimation precision. As can be inferred from Figure 5.3B, this increase is most dramatic when the number of b -values is low. Though the interquartile range decreases monotonically with increasing number of b -values, the improvements are very small from 10 b -values and up.

Since both phasor unmixing and linear unmixing showed very similar accuracy and precision for all tested cases, we can conclude that there is no intrinsic SNR benefit in applying the phasor transform. The benefit of using this technique for multi-component separation does not exceed that of a linear unmixing method. This leads us to conclude that the observed SNR benefit in fraction estimates using phasor unmixing is due to the fact that the diffusivities are fixed (6). The transform itself does not contribute to the SNR benefit observed by Vergeldt *et al.* (4).

Using the phasor transform can still be beneficial since the transformed location of a signal provides additional knowledge due geometric properties of phasor space. The developed phasor-based IVIM fitting technique serves as an example of this principle. Using the geometric properties of phasor space in a line-projection strategy allowed a reduction of the number of free parameters to one. Additionally, proximity of a phasor-

transformed curve to the (deformed) semi-circle is an indicator of mono-exponential decay, which allowed a regularization based on the IVIM fraction and distance to the semi-circle. This combination resulted in more stable fitting results, where phasor-based fitting consistently produced the highest precision for f and D in a limited set of simulations, as presented in Figures 5.4 and 5.5. In terms of accuracy, there was no clear winner since either phasor-based fitting or segmented fitting performed best depending on the simulated tissue, the evaluated parameter and the number of b -values.

The PDFs of estimated IVIM parameters f and D are largely similar between the simulated and measured in-vivo data, when comparing the distributions in Figure 5.5. Since all variation in parameter estimation in the simulation can only stem from the added Rician noise and given the observation that the distributions in-vivo are only slightly wider, we conclude that noise is the dominant factor causing variations in IVIM parameter estimation in-vivo.

The parameter maps of the healthy volunteer in Figure 5.6 show that the most plausible D parameter maps are generated by the segmented and phasor-based method; the maps generated by the non-linear methods contain many areas with implausibly low values. At those locations, the non-linear fits converge to a local minimum with a very low D^* value and a very high f . This tendency can also be observed in Figure 5.5, where the small peak for estimated f around 0.7 corresponds with a peak for estimated D at very low values. Both phasor-based and segmented methods avoid this local minimum. Based on our experiment with either 15 or 6 b -values, the D map generated by phasor seems to be more robust against a low number of sampling points. Likely because in the phasor-based fit all data points are used to estimate D , while in the segmented fit only data points above the threshold are included in this estimate. A lower number of required b -values may be a valuable advantage in the clinic, since acquiring less b -values saves scan time.

All methods struggled to estimate D^* accurately and precisely. Since the segmented method is a linear method, the segmented method is also the only method that is unconstrained for D^* and frequently returns negative values, even if the value for D is positive. This is likely due to noise and the fact that D^* is very hard to estimate. Additionally, the data points that are used for estimating D are more heavily influenced by the Rician nature of the noise since these are the data points corresponding to the highest b -values and consequently the lowest amount of signal. An error in the estimate for D will propagate into the estimate for D^* , which is estimated in the last step of the segmented method. This might be an explanation for the negative D^* values found by the segmented method.

All methods, except the constrained non-linear fit, returned negative values in the parameter maps. These values were more frequent in central areas of the brain, mostly in white matter where the fractions are expected to be lower. Furthermore, in these central areas the SNR of the MR signal is lower due to a lower radiofrequency receive efficiency in these areas. Therefore, these slightly negative values most likely arise due to noise. Even though constraining f between 0 and 1 prevented negative estimates, it did not improve the nonlinear methods performance much. Instead, Figure 5.5 shows

the number of estimates where f was just below 1 increased. An f of almost 1 is a highly implausible result in-vivo.

In Figure 5.7, the phasor plot of b -values up to 2500 s/mm^2 contains a cluster of voxels that roughly corresponds to a hyperintense region on the FLAIR image of a glioblastoma patient. Since the same cluster is not clearly visible in the plot of b -values up to 1000 s/mm^2 , this separation might indicate a change in diffusion kurtosis. This is in agreement with recent studies which have shown that glioma's have altered kurtosis parameters compared to normal appearing white matter and that measurements of mean kurtosis can distinguish low-grade from high-grade glioma's (29,30). Including FLAIR hyperintensities into the CTV for radiotherapy planning is a matter of debate, since these regions can represent either residual tumor or edema (31). Current guidelines still recommend segmenting the GTV using a T_1w contrast-enhanced image and adding an isotropic 20 mm margin to define the CTV. A more refined definition of radiotherapy targets may lead to better local control and less side effects. Future studies might focus on whether the observed cluster has its basis in diffusion kurtosis and whether it can aid in achieving a more direct estimation of the CTV volume by distinguishing between edema and residual tumor.

A limitation of this study is that the IVIM fit was tested only on simulated data and data of one healthy volunteer and one glioblastoma patient. A limited set of model parameters was tested and the simulated data contains only two components, while in in-vivo data multiple components can be present. Most notably, free water was omitted from the simulations. The influence of three or more components on the IVIM fitting techniques was not investigated. However, the results in a healthy volunteer suggest that the influence of extra components is similar for the nonlinear and phasor IVIM techniques. The influence of a wider range of brain pathologies on the calculated parameter maps might be of interest in a clinical setting. The aim of the present work however, was to assess the added value of the phasor transformation in component separation techniques. The presented phasor IVIM fitting technique serves as an example of the possible benefit to be gained from this transformation, more optimal fitting strategies that take additional phasor-based information into account might achieve better results. Future work may need to focus on improvements of phasor-based fitting and rigorous evaluation of such a technique in a wide range of clinical cases.

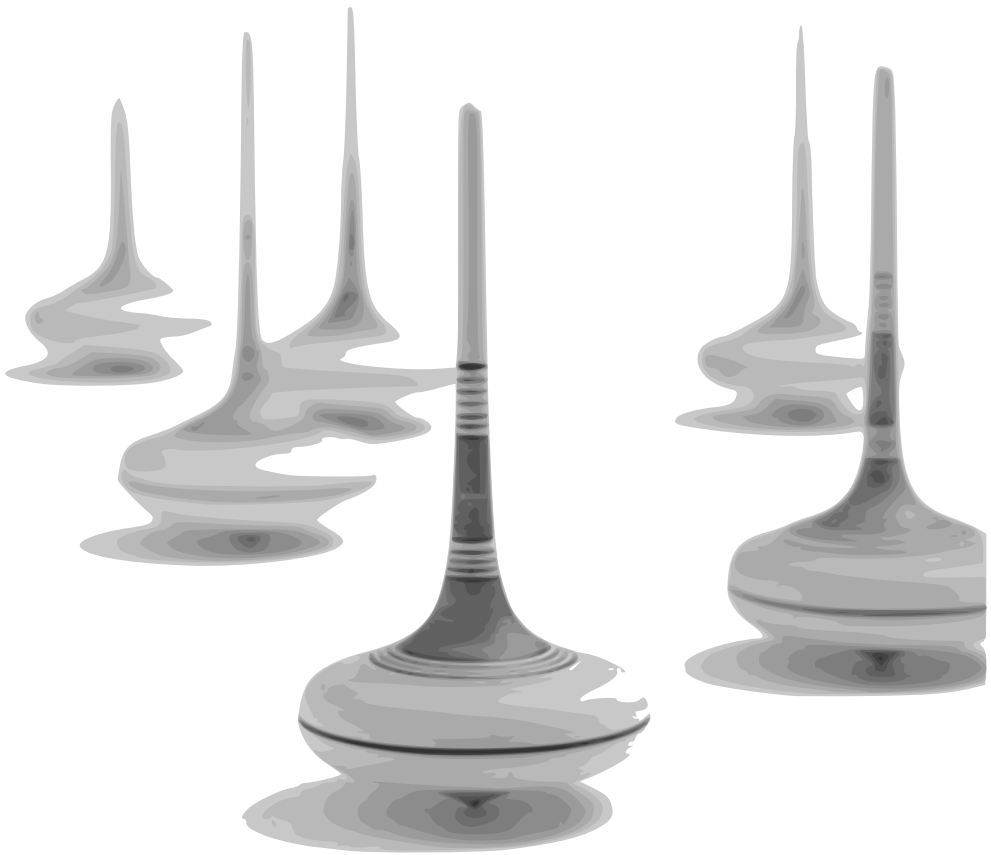
In conclusion, although use of the phasor transform does not yield more stable fraction estimates in fixed-diffusivity unmixing, a phasor-based IVIM fitting routine yielded more stable parameter maps with a higher precision than standard nonlinear methods. Though there is no intrinsic noise benefit from using the phasor transform, the additional knowledge gained from the geometrical configuration of phasor space can aid fitting routines, e.g. the IVIM fitting routine presented in this chapter.

References

1. Clayton AHA, Hanley QS, Verveer PJ. Graphical representation and multicomponent analysis of single-frequency fluorescence lifetime imaging microscopy data. *J Microsc-Oxford* 2004;213:1-5.
2. Redford GI, Clegg RM. Polar plot representation for frequency-domain analysis of fluorescence lifetimes. *J Fluoresc* 2005;15(5):805-815.

3. Digman MA, Caiolfa VR, Zamai M, Gratton E. The phasor approach to fluorescence lifetime imaging analysis. *Biophys J* 2008;94(2):L14-L16.
4. Vergeldt FJ, Prusova A, Fereidouni F, van Amerongen H, van As H, Scheenen TWJ, Bader AN. Multi-component quantitative magnetic resonance imaging by phasor representation. *Sci Rep* 2017;7.
5. Fereidouni F, Bader AN, Gerritsen HC. Spectral phasor analysis allows rapid and reliable unmixing of fluorescence microscopy spectral images. *Opt Express* 2012;20(12):12729-12741.
6. Verveer PJ, Squire A, Bastiaens PIH. Global analysis of fluorescence lifetime imaging microscopy data. *Biophys J* 2000;78(4):2127-2137.
7. Tax CMW. Data Modelling and Feature Extraction. *Less Confusion in Diffusion MRI*. Utrecht: Utrecht University; 2016. p 23-32.
8. Keil VC, Madler B, Gielen GH, Pintea B, Hiththetiya K, Gaspranova AR, Gieseke J, Simon M, Schild HH, Hadzizadeh DR. Intravoxel Incoherent Motion MRI in the Brain: Impact of the Fitting Model on Perfusion Fraction and Lesion Differentiability. *J Magn Reson Imaging* 2017;46(4):1187-1199.
9. de Luca A, Leemans A, Bertoldo A, Arrigoni F, Froeling M. A robust deconvolution method to disentangle multiple water pools in diffusion MRI. *NMR Biomed* 2018;in press.
10. Federau C, O'Brien K, Meuli R, Hagmann P, Maeder P. Measuring brain perfusion with intravoxel incoherent motion (IVIM): Initial clinical experience. *J Magn Reson Imaging* 2014;39(3):624-632.
11. Hu YC, Yan LF, Wu L, Du P, Chen BY, Wang L, Wang SM, Han Y, Tian Q, Yu Y, Xu TY, Wang W, Cui GB. Intravoxel incoherent motion diffusion-weighted MR imaging of gliomas: efficacy in preoperative grading. *Sci Rep* 2014;4.
12. Catanese A, Malacario F, Cirillo L, Toni F, Zenesini C, Casolino D, Bacci A, Agati R. Application of intravoxel incoherent motion (IVIM) magnetic resonance imaging in the evaluation of primitive brain tumours. *Neuroradiol J* 2018;31(1).
13. Thust SC, van den Bent MJ, Smits M. Pseudoprogression of brain tumors. *J Magn Reson Imaging* 2018.
14. Le Bihan D, Breton E, Lallemand D, Grenier P, Cabanis E, Lavaljeantet M. Mr Imaging of Intravoxel Incoherent Motions - Application to Diffusion and Perfusion in Neurologic Disorders. *Radiology* 1986;161(2):401-407.
15. Lemke A, Stieltjes B, Schad LR, Laun FB. Toward an optimal distribution of b values for intravoxel incoherent motion imaging. *Magn Reson Imaging* 2011;29(6):766-776.
16. Pekar J, Moonen CTW, van Zijl PCM. On the Precision of Diffusion/Perfusion Imaging by Gradient Sensitization. *Magn Reson Med* 1992;23(1):122-129.
17. Cho GY, Moy L, Zhang JL, Baete S, Lattanzi R, Moccaldi M, Babb JS, Kim S, Sodickson DK, Sigmund EE. Comparison of Fitting Methods and b-Value Sampling Strategies for Intravoxel Incoherent Motion in Breast Cancer. *Magn Reson Med* 2015;74(4):1077-1085.
18. Fereidouni F, Esposito A, Blab GA, Gerritsen HC. A modified phasor approach for analyzing time-gated fluorescence lifetime images. *J Microsc* 2011;244(3):248-258.
19. Jensen JH, Helpert JA, Ramani A, Lu HZ, Kaczynski K. Diffusional kurtosis imaging: The quantification of non-Gaussian water diffusion by means of magnetic resonance imaging. *Magn Reson Med* 2005;53(6):1432-1440.
20. Grecco HE, Roda-Navarro P, Verveer PJ. Global analysis of time correlated single photon counting FRET-FLIM data. *Opt Express* 2009;17(8):6493-6508.
21. Coleman TF, Li Y. On the convergence of interior-reflective Newton methods for nonlinear minimization subject to bounds. *Mathematical Programming* 1994;67(1):189-224.
22. Coleman TF, Li Y. An interior trust region approach for nonlinear minimization subject to bounds. *Siam J Optimiz* 1996;6(2):418-445.
23. LeBihan D. Molecular diffusion, tissue microdynamics and microstructure. *NMR Biomed* 1995;8(7-8):375-386.
24. Gudbjartsson H, Patz S. The Rician Distribution of Noisy Mri Data. *Magn Reson Med* 1995;34(6):910-914.
25. Froeling M, Tax CMW, Vos SB, Luijten PR, Leemans A. "MASSIVE" brain dataset: Multiple acquisitions for standardization of structural imaging validation and evaluation. *Magn Reson Med* 2017;77(5):1797-1809.
26. Vos SB, Tax CMW, Luijten PR, Ourselin S, Leemans A, Froeling M. The importance of correcting for signal drift in diffusion MRI. *Magn Reson Med* 2017;77(1):285-299.
27. Leemans A, Jeurissen B, Sijbers J, Jones D. ExploreDTI: a graphical toolbox for processing, analyzing, and visualizing diffusion MR data. *Proc Intl Soc Mag Reson Med* 2009;17:3537.
28. Gaser C. CAT - A Computational Anatomy Toolbox for SPM. v12.1. <http://www.neuro.uni-jena.de/cat> 2017.

29. Qi C, Yang S, Meng LX, Chen HY, Li ZL, Wang SJ, Jiang T, Li SW. Evaluation of cerebral glioma using 3T diffusion kurtosis tensor imaging and the relationship between diffusion kurtosis metrics and tumor cellularity. *J Int Med Res* 2017;45(4):1347-1358.
30. Qi XX, Shi DF, Ren SX, Zhang SY, Li L, Li QC, Guan LM. Histogram analysis of diffusion kurtosis imaging derived maps may distinguish between low and high grade gliomas before surgery. *Eur Radiol* 2018;28(4):1748-1755.
31. Niyazi M, Brada M, Chalmers AJ, Combs SE, Erridge SC, Fiorentino A, Grosu AL, Lagerwaard FJ, Minniti G, Mirimanoff RO, Ricardi U, Short SC, Weber DC, Belka C. ESTRO-ACROP guideline "target delineation of glioblastomas". *Radiother Oncol* 2016;118(1):35-42.



Summary & General Discussion



6.1 Summary

This thesis investigates artifact correction and signal quantification in high field breast MRI. We focus on dynamic contrast-enhanced MRI (DCE-MRI) and diffusion-weighted imaging (DWI). DCE-MRI, the focus of the first part of this thesis, is sensitive to inhomogeneities in the radiofrequency transmit (B_1^+) field. **Chapter 2** investigates B_1^+ field characterization and **Chapter 3** explores the possibilities of correcting DCE-MRI for the related contrast artifact. The second part of this thesis focuses on DWI, which is prone to spatial distortion artifacts due to inhomogeneities in the static magnetic (B_0) field. In **Chapter 4** we propose a new way to better correct for these distortions, specifically in the breast. **Chapter 5** focuses on better quantification of the diffusion signal measured in DWI.

6.1.1 DCE-MRI

The course of time-intensity curves in DCE-MRI changes in case of imperfect B_1^+ : a low B_1^+ level induces curve flattening. As a first step in correcting for this effect, **Chapter 2** proposes a fast and noise-free way to estimate the B_1^+ distribution when using local transmit coils at 7 T. Based on finite difference time domain simulations in 4 anatomically varying in-silico models, intersubject differences in local transmit B_1^+ fields of the breast were found to be comparable to the accuracy of B_1^+ mapping methods. Therefore, a generic template was proposed and tested in 15 healthy volunteers with a wide range of breast anatomies. In a subset of three volunteers, the agreement between the proposed template approach and a B_1^+ mapping method was compared against the agreement between two consecutive acquisitions using the same mapping protocol. Repeated measurements had an error of up to 15% of the nominal angle; this error range increased slightly by approximately 6% when using a B_1^+ template. Consequently, a single generic B_1^+ template suits subjects over a wide range of breast anatomies, eliminating the need for a time-consuming and noise-prone B_1^+ mapping protocol.

In **Chapter 3** we use the template approach developed in **Chapter 2** as a basis for DCE contrast correction. Using the template as a source of B_1^+ information, we investigated the correctable B_1^+ range post acquisition. A direct mapping from measured to true signal intensities was devised to limit noise amplification during correction. Simulations showed that the correctable B_1^+ range extends down to 43% of the nominal angle. The distribution of curve types in a 7 T patient dataset with a wide range of B_1^+ levels corresponded better to those reported in literature after correction. DCE corrections influenced the performance of grade prediction models, but this conclusion warrants further investigation due to the limited size of the dataset.

6.1.2 DWI

DWI is usually acquired using an echo-planar imaging (EPI) readout, which is highly susceptible to geometrical distortions caused by B_0 inhomogeneities, due to its low readout bandwidth. **Chapter 4** shows that the B_0 field in breast has high discontinuities at gland-fat tissue interfaces. Therefore, we developed a distortion correction method that incorporates high-resolution off-resonance maps to better solve severe distortions at tissue interfaces. Quantitative comparisons showed an increase in conformity between corrected EPI images and a non-EPI high-bandwidth reference scan, both ex-vivo and in-vivo. All metrics showed a significant improvement when a high-resolution

off-resonance map was used, in particular at tissue boundaries. It is this improvement at tissue interfaces, which is due to the use of high-resolution off-resonance maps that gives our method the advantage over existing distortion correction techniques.

Quantification of the mixed signals measured in DWI can be quite challenging, as increasingly complicated signal models produce increasingly unstable fits. **Chapter 5** explores whether the phasor transform can aid in producing more stable parameter maps; first in the context of fixed-diffusivity fraction estimation and second in the context of fitting the intravoxel incoherent motion (IVIM) model. While the phasor-based approach for fixed-diffusivity fraction estimation didn't improve upon simply solving a linear system, phasor-based IVIM fitting did produce more stable parameter maps for two parameters (the pseudodiffusion fraction f , and the diffusion constant D) compared to nonlinear fitting and segmented fitting.

6.2 General Discussion

Since the introduction of breast MRI into the clinic, the field strength of the magnets used has steadily increased (1). The tendency to increase the field strength was mainly driven by its promise of higher intrinsic signal-to-noise ratio (SNR), which would enable better spatial resolutions or faster scanning (2). Additionally, the increase in chemical shift enables a better separation of chemical species using spectroscopy techniques (3). At the time of writing, breast MRI examinations using field strengths up to 3 T are routinely performed in clinics worldwide, while 7 T breast MRI is actively used in clinical trials. Efforts are underway to get human examinations at field strengths up to 14 T.

As field strengths increase, the homogeneity of the magnetic fields decreases (3). This causes an increase in severity for a variety of artifacts in the images, two of which are studied in this thesis. The first is the radiofrequency inhomogeneity artifact, which causes changes in the course of DCE time-intensity curves. The second is the static field inhomogeneity artifact which causes geometrical distortions in DWI. This thesis has focused on correction strategies for both artifacts.

There are many strategies available for artifact compensation during acquisition, many of which are part of standard clinical protocols at 3 T. Examples include static shims to improve static field homogeneity and dual transmit to improve homogeneity of the excitation field (4-6). With increasing field strengths, the inhomogeneities grow more severe and complex. As a consequence, these techniques are no longer sufficient. Therefore, sophisticated compensation techniques during acquisition have recently been developed, such as higher order shimming and multi-channel parallel transmission (7-9). At the same time, sophisticated coil designs facilitate improvements in RF homogeneity (10,11). RF distributions can, to some extent, be customized with the use of dielectric pads, which allow steering of the available RF power to desired regions (12).

However, artifact compensation during acquisition is always limited. Not only by the laws of physics and hardware limitations, but also by the anatomy and physiology of the human body as well as time constraints. Therefore, post-acquisition corrections can often improve upon data that has already been acquired with state-of-the-art com-

pensation strategies (13-15). In this thesis, post-acquisition correction and quantification techniques are developed for field inhomogeneity artifacts in DCE-MRI and DWI at 7 T. At the same time, post-acquisition correction is limited as well, by the data that has already been acquired and the way in which it was acquired. Consequently, strategies combining artifact compensation during acquisition with artifact correction after acquisition use the best of both worlds in order to achieve the best possible result.

Alternatively, MR imaging sequences can be devised that are less prone to field inhomogeneities. DWI can be performed with a fast spin echo (FSE) readout instead of an EPI readout (16,17). This has allowed essentially distortion-free imaging in several anatomical regions, including the oral cavity where B_0 field inhomogeneities are especially severe (18-20). This technique is difficult to translate to higher fields, since an FSE sequence uses many inversion pulses in rapid succession. Due to the high RF demand of such a sequence, the safety limits for RF power deposition in the human body are quickly reached, unless the time between consecutive pulses is increased. This reduces scan time efficiency and limits the resolution that can be achieved in an acceptable time frame.

T_1 -weighted images that are less prone to bias introduced by B_1^+ inhomogeneity can be acquired using a pulse sequence named MP2RAGE (21). After an inversion pulse, two sets of gradient echoes are acquired at different inversion times. From these echoes, a T_1 -weighted image with reduced B_1^+ bias, as well as a quantitative estimate for T_1 can be obtained. Though this method is robust and widely used in high field MRI, it is not usually considered for DCE imaging due to the time required to acquire the extra set of echoes. Since in breast DCE-MRI the recommended maximum acquisition time for one 3D volume is 90 seconds, this would severely limit the resolution that can be achieved with this technique (22). Furthermore, some residual B_1^+ contrast remains in the acquired images, which can only be removed post-acquisition if a B_1^+ map is available (23).

Chapter 2 of this thesis proposes a template approach to calculate B_1^+ maps in case of local transmit breast coils at 7 T. Compared to conventional B_1^+ mapping methods, this method saves scan time and has better noise characteristics. As this chapter shows, inter-individual differences in B_1^+ distributions across volunteers with a large variation in breast anatomy are within the accuracy range of conventional mapping methods. This justifies the use of a generic template. Additionally, since the template is constructed from computer simulation, it is essentially noise free.

An alternative method to estimate B_1^+ in the breast that does not require extra scan time is the reference-region variable flip angle (RR-VFA) method (24,25). This method estimates B_1^+ in fat from T_1 -weighted gradient echo images acquired with different flip angles, by assuming a constant T_1 value for fat throughout the breast. The B_1^+ in glandular tissue is subsequently interpolated from the measured values in fat. Therefore, this method will likely be less accurate in dense breasts and is not suitable for fat-suppressed images. Pineda *et al.* postulate that the RR-VFA approach does not require extra scan time, since the variable flip angle images are required for T_1 mapping of glandular tissue prior to contrast injection (25). However, Haacke *et al.* have shown that the precontrast T_1 has a very limited effect on contrast estimates and suggest omitting T_1 measurements altogether (26).

Chapter 3 of this thesis proposes a correction method for B_1^+ inhomogeneities in DCE-MRI based on a direct mapping of measured signal intensities to true signal intensities. B_1^+ correction of DCE-MRI data is not typically performed in this manner, existing methods quantify underlying tissue parameters instead. They do this either sequentially by first calculating a B_1^+ -corrected estimate for T_1 at each time point and calculating other parameters of interest next (13,15), or directly by finding an approximate relationship between parameter estimates at imperfect B_1^+ levels and the true parameters (27). As **Chapter 3** shows, the proposed direct signal-intensity mapping approach has clear noise amplification benefits. Additionally, this low-level correction potentially allows a high degree of compatibility with existing clinical workflows and automated analysis techniques, such as computer-aided diagnosis (28).

Chapter 4 shows that the B_0 field distribution in the breast is very irregular, possibly due to susceptibility differences between adipose and glandular tissue. The DWI distortion correction technique proposed in this chapter resembles inverse problem approaches that have been described earlier (29,30). However, contrary to these and other techniques used in breast (14), the proposed method takes the irregularity of the B_0 field into account by solving the inverse problem at a spatial resolution higher than the acquired EPI data. This allows incorporation of high resolution B_0 maps that better capture the B_0 irregularities in the breast. This approach achieves better distortion correction, especially at tissue boundaries where B_0 inhomogeneity is worst.

The diffusion signal in-vivo is often quantified using the intravoxel incoherent motion (IVIM) model (31). Since this model is a biexponential model, fitting results are often unstable in the presence of noise (32). In **Chapter 5** we propose to fit this model in phasor space instead of signal space (33). Phasor-based IVIM fitting resulted in more stable fits for IVIM parameters f and D : the precision was higher compared to nonlinear fitting and segmented fitting (34). This was achieved by using geometrical properties of phasor space as prior knowledge in the fitting strategy. It allowed for both a reduction in the number of free parameters and a novel regularization strategy in phasor space. In future work, similar strategies may be devised for other signal models (35). Additionally, the precision of the phasor-based maps was better than that of maps calculated with other methods for a lower number of b-values. This might allow the generation of parameter maps in shorter scan times, since fewer b-values need to be acquired.

The correction techniques of **Chapters 3** and **4** are developed for and tested at 7 T. Since both techniques are based on MR physics principles that do not change between field strengths, they are expected to work at other field strengths as well, though it is important to make some considerations. The correctable B_1^+ range reported in **Chapter 3** might change, since the T_1 range measured during DCE examinations depends on field strength (36-38). Whether the template technique, developed in **Chapter 2** for B_1^+ characterization in the breast at 7 T, is sufficient for the increased inhomogeneity at higher field strengths will have to be investigated. The benefit of using a high-resolution off-resonance map for distortion correction, as suggested in **Chapter 4**, will likely increase with field strength. Although for higher fields a higher resolution off-resonance map may be required. Additionally, the off-resonance map may need to be acquired using thinner slices to account for signal loss due to higher B_0 gradients.

Sometimes it is better to omit artifact correction altogether. **Chapter 5** describes a signal quantification technique for DWI that implicitly achieves artifact correction. Even though the source images are affected by the RF inhomogeneity artifact, the calculated parameter maps are not. This is due to the fact that this artifact affects all source images equally and fitted parameters are not affected by it. Of note: the images in this chapter were still corrected for the static field distortion artifact.

Another reason to omit artifact correction or quantification might be a possible drop in SNR, since many correction and quantification methods are hampered by noise amplification. In order to produce a clinically usable correction or quantification method, it is important to undertake steps to reduce the amount of noise amplification. **Chapters 4 and 5** do so using different kinds of regularization, while **Chapter 3** avoids an intermediate image ratio calculation and performs a direct mapping from measured to corrected signals instead. Reducing noise amplification might also save scan time. As an example, in **Chapter 5** we were able to produce parameter maps of the same quality as conventional methods using less b-values.

One could argue that DWI images might also benefit from B_1^+ correction. And, vice versa, that DCE images might benefit from B_0 correction. Yet, this thesis pursues neither direction. B_0 distortions of gradient echo images, such as DCE images, are a well-researched field and the physics are very similar to those described in **Chapter 4** (39,40). However, due to the relatively high readout bandwidth used in these sequences, the tolerance against inhomogeneities in B_0 is much higher than that of the EPI sequences used in DWI. This kind of artifact therefore only becomes noticeable when metallic implants are in or near the field of view (41). On the other hand, DWI sequences are prone to RF inhomogeneity artifacts, even though they are implicitly sidestepped in signal quantification efforts such as those in **Chapter 5**. Correcting DWI images for B_1^+ might benefit interpretation the images themselves, but will not impact calculated parameter maps.

The techniques developed in this manuscript could be developed further or be made less reliant on external sources of information about field distributions. For example, in **Chapter 2** we introduced a generic template that is individually and linearly scaled using information from the power optimization phase. Better results might be obtained by performing a more complex scaling based on more predictors, such as breast or glandular tissue volume. An alternative strategy might be to generate a B_1^+ simulation library for a large number of volunteers (42). Individual B_1^+ predictions can then be obtained by interpolating between those volunteers in the library that are most similar to the scanned individual. DCE corrections might even be performed without B_1^+ information altogether. If enough data is available, a machine learning method could be trained to generate corrected images from corrupted measured data. Since it is impractical to acquire artifact-free data, such a method would have to resort to simulations to generate training data.

Once all inhomogeneities are either compensated, corrected or side stepped, patients can fully benefit from all the advantages that high field MRI has to offer. This includes not only high-resolution DCE-MRI and DWI, but also spectroscopy techniques which measure tumor metabolism. Measurements of this kind may be able to predict the re-

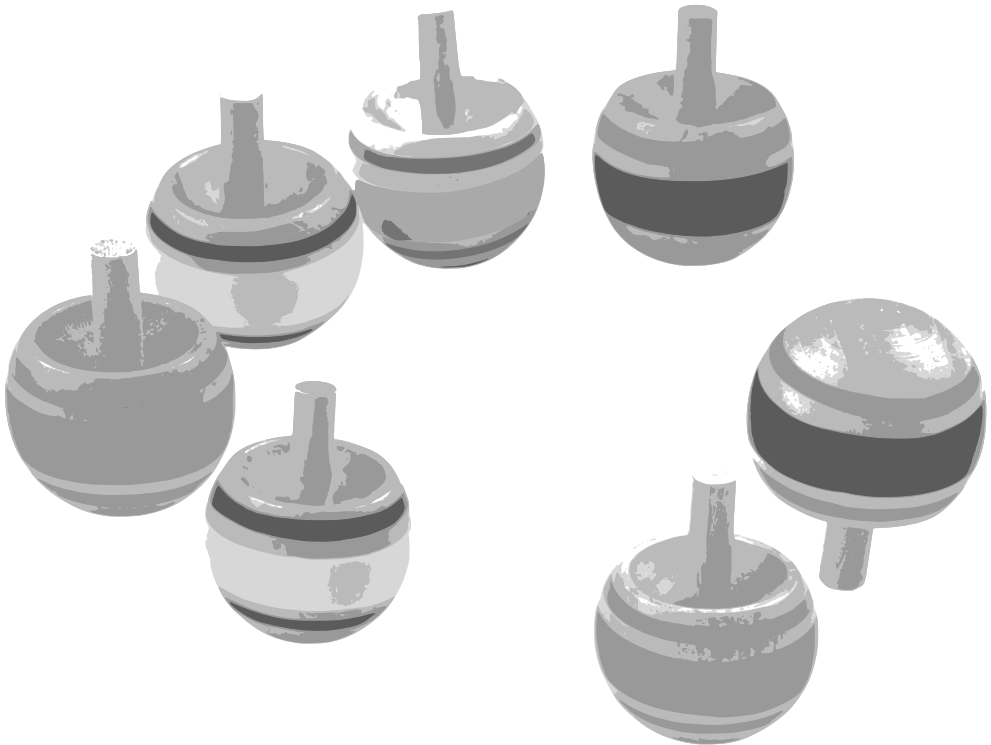
sponse to neoadjuvant therapy in an early stage of treatment (43,44). Multiparametric analyses combining phosphorous spectroscopy with DCE-MRI for prediction of systemic therapy response have achieved better agreement with postoperative findings than the conventional preoperative workup (45). Higher resolution scans not only permit detection of smaller lesions, they also improves assessment of the heterogeneity of contrast uptake, such as rim enhancement, which is associated with worse survival in triple negative breast cancers (46). Currently, these advancements in breast MRI are not yet available to patients outside of clinical trials. The artifact correction and signal quantification techniques presented in this thesis are a necessary step towards clinical integration of high field breast MRI.

References

1. Norris DG. High field human imaging. *J Magn Reson Imaging* 2003;18(5):519-529.
2. Hoult DI, Chen CN, Sank VJ. The Field-Dependence of Nmr Imaging .2. Arguments Concerning an Optimal Field-Strength. *Magn Reson Med* 1986;3(5):730-746.
3. Ladd ME, Bachert P, Meyerspeer M, Moser E, Nagel AM, Norris DG, Schmitter S, Speck O, Straub S, Zaiss M. Pros and cons of ultra-high-field MRI/MRS for human application. *Prog Nucl Mag Res Sp* 2018;109:1-50.
4. Gruetter R. Automatic, Localized In vivo Adjustment of All 1st-Order and 2nd-Order Shim Coils. *Magn Reson Med* 1993;29(6):804-811.
5. Willinek WA, Gieseke J, Kukuk GM, Nelles M, Konig R, Morakkabati-Spitz N, Traber F, Thomas D, Kuhl CK, Schild HH. Dual-Source Parallel Radiofrequency Excitation Body MR Imaging Compared with Standard MR Imaging at 3.0 T: Initial Clinical Experience. *Radiology* 2010;256(3):966-975.
6. Rahbar H, Partridge SC, DeMartini WB, Gutierrez RL, Parsian S, Lehman CD. Improved B1 homogeneity of 3 tesla breast MRI using dual-source parallel radiofrequency excitation. *J Magn Reson Imaging* 2012;35(5):1222-1226.
7. Boer VO, Luttje MP, Luijten PR, Klomp DWJ. Requirements for static and dynamic higher order B0 shimming of the human breast at 7 T. *NMR Biomed* 2014;27(6):625-631.
8. Katscher U, Bornert P. Parallel RF transmission in MRI. *NMR Biomed* 2006;19(3):393-400.
9. Padormo F, Beqiri A, Hajnal JV, Malik SJ. Parallel transmission for ultrahigh-field imaging. *NMR Biomed* 2016;29(9):1145-1161.
10. Krikken E, Steensma BR, Voogt IJ, Luijten PR, Klomp DWJ, Raaijmakers AJE, Wijnen JP. Homogeneous B-1(+) for bilateral breast imaging at 7 T using a five dipole transmit array merged with a high density receive loop array. *NMR Biomed* 2019;32(2).
11. van der Velden TA, Italiaander M, van der Kemp WJM, Raaijmakers AJE, Schmitz AMT, Luijten PR, Boer VO, Klomp DWJ. Radiofrequency Configuration to Facilitate Bilateral Breast P-31 MR Spectroscopic Imaging and High-Resolution MRI at 7 Tesla. *Magn Reson Med* 2015;74(6):1803-1810.
12. Brink WM, van der Jagt AMA, Versluis MJ, Verbist BM, Webb AG. High Permittivity Dielectric Pads Improve High Spatial Resolution Magnetic Resonance Imaging of the Inner Ear at 7 T. *Invest Radiol* 2014;49(5):271-277.
13. Bedair R, Graves MJ, Patterson AJ, McLean MA, Manavaki R, Wallace T, Reid S, Mendichovszky I, Griffiths J, Gilbert FJ. Effect of Radiofrequency Transmit Field Correction on Quantitative Dynamic Contrast-enhanced MR Imaging of the Breast at 3.0 T. *Radiology* 2016;279(2):368-377.
14. Hancu I, Lee SK, Hulsev K, Lenkinski R, Holland D, Sperl JI, Tan ET. Distortion correction in diffusion-weighted imaging of the breast: Performance assessment of prospective, retrospective, and combined (prospective plus retrospective) approaches. *Magn Reson Med* 2017;78(1):247-253.
15. Tsai WC, Kao KJ, Chang KM, Hung CF, Yang Q, Lin CE, Chen CM. B1 Field Correction of T1 Estimation Should Be Considered for Breast Dynamic Contrast-enhanced MR Imaging Even at 1.5 T. *Radiology* 2017;282(1):55-62.
16. Hennig J, Nauerth A, Friedburg H. Rare Imaging - a Fast Imaging Method for Clinical Mr. *Magn Reson Med* 1986;3(6):823-833.
17. Norris DG, Bornert P, Reese T, Leibfritz D. On the Application of Ultra-Fast Rare Experiments. *Magn Reson Med* 1992;27(1):142-164.
18. Kozlowski P, Chang SD, Goldenberg SL. Diffusion-weighted MRI in prostate cancer - comparison between single-shot fast spin echo and echo planar imaging sequences. *Magn Reson Imaging* 2008;26(1):72-76.

19. Hilbert F, Wech T, Neubauer H, Veldhoen S, Bley TA, Kostler H. Comparison of Turbo Spin Echo and Echo Planar Imaging for intravoxel incoherent motion and diffusion tensor imaging of the kidney at 3 Tesla. *Z Med Phys* 2017;27(3):193-201.
20. Hirata K, Nakaura T, Okuaki T, Kidoh M, Oda S, Utsunomiya D, Namimoto T, Kitajima M, Nakayama H, Yamashita Y. Comparison of the image quality of turbo spin echo- and echo-planar diffusion-weighted images of the oral cavity. *Medicine* 2018;97(19).
21. Marques JP, Kober T, Krueger G, van der Zwaag W, Van de Moortele PF, Gruetter R. MP2RAGE, a self bias-field corrected sequence for improved segmentation and T-1-mapping at high field. *Neuroimage* 2010;49(2):1271-1281.
22. American College of Radiology Practice Parameter for the Performance of Contrast-Enhanced Magnetic Resonance Imaging (MRI) of the Breast. Available from: <https://www.acr.org/-/media/ACR/Files/Practice-Parameters/MR-Contrast-Breast.pdf>. Accessed on: May 28, 2019.
23. Marques JP, Gruetter R. New Developments and Applications of the MP2RAGE Sequence - Focusing the Contrast and High Spatial Resolution R-1 Mapping. *PLoS One* 2013;8(7).
24. Sung K, Saranathan M, Daniel BL, Hargreaves BA. Simultaneous T-1 and B-1(+) Mapping Using Reference Region Variable Flip Angle Imaging. *Magn Reson Med* 2013;70(4):954-961.
25. Pineda FD, Medved M, Fan XB, Karczmar GS. B-1 and T-1 Mapping of the Breast with a Reference Tissue Method. *Magn Reson Med* 2016;75(4):1565-1573.
26. Haacke EM, Filletti CL, Gattu R, Ciulla C, Al-Bashir A, Suryanarayanan K, Li M, Latif Z, DelProposto Z, Sehgal V, Li T, Torquato V, Kanaparti R, Jiang J, Neelavalli J. New algorithm for quantifying vascular changes in dynamic contrast-enhanced MRI independent of absolute T1 values. *Magn Reson Med* 2007;58(3):463-472.
27. Zhong XR, Martin T, Wu HH, Nayak KS, Sung K. Prostate DCE-MRI with B-1(+) correction using an approximated analytical approach. *Magn Reson Med* 2018;80(6):2525-2537.
28. Gilhuijs KGA, Giger ML, Bick U. Computerized analysis of breast lesions in three dimensions using dynamic magnetic-resonance imaging. *Med Phys* 1998;25(9):1647-1654.
29. Munger P, Crelief GR, Peters TM, Pike GB. An inverse problem approach to the correction of distortion in EPI images. *IEEE Trans Med Imaging* 2000;19(7):681-689.
30. Andersson JLR, Skare S, Ashburner J. How to correct susceptibility distortions in spin-echo echo-planar images: application to diffusion tensor imaging. *Neuroimage* 2003;20(2):870-888.
31. Le Bihan D, Breton E, Lallemand D, Grenier P, Cabanis E, Lavaljeantet M. Mr Imaging of Intravoxel Incoherent Motions - Application to Diffusion and Perfusion in Neurologic Disorders. *Radiology* 1986;161(2):401-407.
32. Lemke A, Stieltjes B, Schad LR, Laun FB. Toward an optimal distribution of b values for intravoxel incoherent motion imaging. *Magn Reson Imaging* 2011;29(6):766-776.
33. Vergeldt FJ, Prusova A, Fereidouni F, van Amerongen H, van As H, Scheenen TWJ, Bader AN. Multi-component quantitative magnetic resonance imaging by phasor representation. *Sci Rep* 2017;7.
34. Pekar J, Moonen CTW, van Zijl PCM. On the Precision of Diffusion/Perfusion Imaging by Gradient Sensitization. *Magn Reson Med* 1992;23(1):122-129.
35. Tax CMW. Data Modelling and Feature Extraction. *Less Confusion in Diffusion MRI*. Utrecht: Utrecht University; 2016. p 23-32.
36. Bottomley PA, Foster TH, Argersinger RE, Pfeifer LM. A Review of Normal Tissue Hydrogen Nmr Relaxation-Times and Relaxation Mechanisms from 1-100 Mhz - Dependence on Tissue-Type, Nmr Frequency, Temperature, Species, Excision, and Age. *Med Phys* 1984;11(4):425-448.
37. Caravan P, Farrar CT, Frullano L, Uppal R. Influence of molecular parameters and increasing magnetic field strength on relaxivity of gadolinium- and manganese-based T(1) contrast agents. *Contrast Media Mol I* 2009;4(2):89-100.
38. Koenig SH, Baglin C, Brown RD. Magnetic-Field Dependence of Solvent Proton Relaxation Induced by Gd3+ and Mn2+ Complexes. *Magn Reson Med* 1984;1(4):496-501.
39. Lüdeke KM, Röschmann P, Tischler R. Susceptibility artifacts in NMR imaging. *Magn Reson Imaging* 1985;3(4):329-343.
40. Zijlstra F, Bouwman JG, Brskute I, Viergever MA, Seevinck PR. Fast Fourier-based simulation of off-resonance artifacts in steady-state gradient echo MRI applied to metal object localization. *Magn Reson Med* 2017;78(5):2035-2041.
41. Koch KM, Hargreaves BA, Pauly KB, Chen W, Gold GE, King KF. Magnetic Resonance Imaging Near Metal Implants. *J Magn Reson Imaging* 2010;32(4):773-787.
42. Homann H, Bornert P, Eggers H, Nehrke K, Dossel O, Graesslin I. Toward Individualized SAR Models and In Vivo Validation. *Magn Reson Med* 2011;66(6):1767-1776.

43. Krikken E, Khlebnikov V, Zaiss M, Jibodh RA, van Diest PJ, Luijten PR, Klomp DWJ, Van Laarhoven HWM, Wijnen JP. Amide chemical exchange saturation transfer at 7 T: a possible biomarker for detecting early response to neoadjuvant chemotherapy in breast cancer patients. *Breast Cancer Res* 2018;20.
44. Krikken E, van der Kemp WJM, van Diest PJ, van Dalen T, van Laarhoven HWM, Luijten PR, Klomp DWJ, Wijnen JP. Early detection of changes in phospholipid metabolism during neoadjuvant chemotherapy in breast cancer patients using phosphorus magnetic resonance spectroscopy at 7T. *NMR Biomed* 2019:e4086.
45. Schmitz AMT, Veldhuis WB, Menke-Pluijmers MBE, van der Kemp WJM, van der Velden TA, Viergever MA, Mali WPTM, Kock MCJM, Westenend PJ, Klomp DWJ, Gilhuijs KGA. Preoperative indication for systemic therapy extended to patients with early-stage breast cancer using multiparametric 7-tesla breast MRI. *PLoS One* 2017;12(9).
46. Schmitz AMT, Loo CE, Wesseling J, Pijnappel RM, Gilhuijs KGA. Association between rim enhancement of breast cancer on dynamic contrast-enhanced MRI and patient outcome: impact of subtype. *Breast Cancer Res Treat* 2014;148(3):541-551.



Appendix



Nederlandse samenvatting

Glow in the dark sterren

Dit proefschrift gaat over beeldvorming met magnetische resonantie (MRI), maar voordat we daarin duiken, moeten we het even hebben over glow in the dark sterren. Het soort sterren die misschien wel op het plafond van je kinderkamer zaten geplakt. (Als jouw kamer toevallig sterrenloos was, had je misschien wel een horloge met lichtgevende wijzerplaten?) Een bijzonder nieuwsgierig kind, zoals de auteur van dit werk, zou zich kunnen afvragen hoe het kan dat die sterren licht blijven geven, zelfs nadat het licht in de kamer al lang uit is. Het antwoord is dat een chemisch proces, fosforescentie, elektronen in de verf van de glow in the dark sterren naar een hogere energietoestand brengt. Deze energie wordt geabsorbeerd uit licht, dat in feite de ster 'oplaadt', en vervolgens langzaam weer afgegeven. Dit zorgt ervoor dat de sterren nog uren kunnen blijven nagloeien nadat het licht in de kamer is uitgegaan.

Het maken van een MRI-scan heeft veel weg van het maken van een foto van lichtgevende glow in the dark sterren in een donkere kamer. In beide gevallen wordt er een opname gemaakt van een object dat elektromagnetische golven uitstraalt. In beide gevallen wordt deze opname pas gemaakt nadat de originele bron van elektromagnetische energie die het object heeft opgeladen is uitgeschakeld. Natuurlijk zijn er ook verschillen. In het geval van MRI is het object dat in beeld wordt gebracht meestal een mens. En de elektromagnetische straling die wordt gebruikt zit niet in het zichtbare spectrum maar in het megahertz-bereik, welbekend van FM-radio en tv-uitzendingen via de (ultra)korte golf.

Hoewel het een versimpeling is, is de analogie van de glow in the dark sterren nuttig voor het begrip van een belangrijk concept in MRI: het object dat we willen meten moeten we eerst exciteren voordat we een signaal kunnen meten. Met andere woorden, we moeten eerst het licht in de kamer aanzetten om onze sterren op te laden, voordat we er in het donker een foto van kunnen nemen. De analogie helpt ook om intuïtief te begrijpen wat er gebeurt als deze excitatie niet gelijk verdeeld is over het gebied dat in beeld wordt gebracht. De gemeten signaalintensiteit verandert in gebieden waar de excitatie onvoldoende is, zoals een glow in the dark ster in een donker hoekje van de kamer minder straalt in het donker.

Dit soort ongelijkmatigheden kunnen een negatieve invloed hebben op de diagnostische kwaliteit van MRI-beelden. Dit proefschrift onderzoekt hoe ongelijkmatigheden in de gebruikte magneetvelden, zoals het excitatieveld, het beste in kaart kunnen worden gebracht en kunnen worden gecorrigeerd, met name in het kader van MRI van de borst op hoog magneetveld. Voor een goed begrip van de veldongelijkmatigheden die in dit proefschrift worden behandeld en de beeldfouten die zij veroorzaken in MRI-scans van de borst, is de eenvoudige glow in the dark analogie niet meer afdoende. De volgende sectie zal daarom een aantal belangrijke begrippen uit de MR-fysica die van belang zijn in dit proefschrift bondig introduceren. De rest van dit hoofdstuk zet de probleemstellingen van dit proefschrift uiteen, en eindigt met een opsomming van de belangrijkste bevindingen.

De natuurkunde van MRI in vogelvlucht

Resonantie

MRI-scanners werken met zeer sterke magnetische velden, meestal in de orde grootte van 0,5 tot 3 Tesla (T). Als je een diamagnetisch object, zoals een glas water, een stuk fruit of zelfs een vrijwilliger of patiënt in zo'n sterk magneetveld plaatst, zullen de magnetische velden van waterstofatomen (of protonspins) in dat object zich oriënteren naar het magnetisch veld van de scanner, het externe magneetveld. Daarnaast zullen de protonspins gaan tolleren met een frequentie die wordt bepaald door de sterkte van het externe magneetveld. Zoals windmolens harder gaan draaien bij sterkere wind, zo gaan de protonspins sneller tolleren bij sterkere externe magneetvelden. Dit fenomeen wordt kernspinresonantie genoemd en de frequentie hiervan heet de Larmorfrequentie.

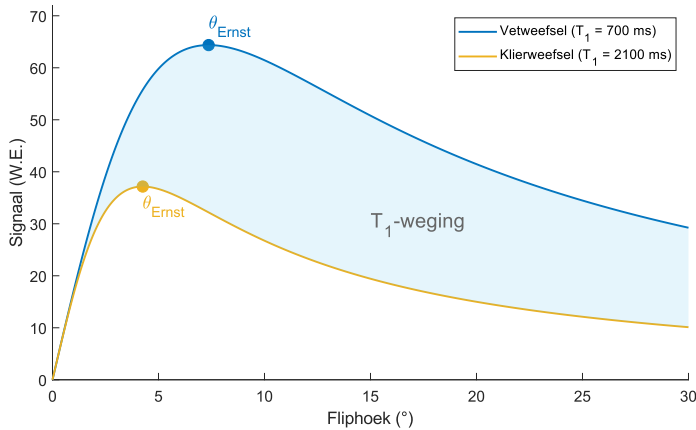
Signalen opwekken

Door de persoon of het object in een magnetisch veld te zetten zullen de protonspins zich naar het veld oriënteren en resoneren, maar hiermee is nog geen MRI-sigitaal opgewekt. Om dit voor elkaar te krijgen, moeten we de spins draaien zodat ze loodrecht op het externe magneetveld staan. Door een radiogolf met de hierboven beschreven Larmorfrequentie uit te zenden, is het mogelijk de spins te draaien. Aangezien deze radiogolf meestal erg kort duurt, slechts een paar milliseconden, noemen we deze meestal een radiofrequentie (RF) excitatiepuls.

We kunnen kiezen hoe ver we de spins ten opzichte van het externe veld willen laten draaien door de sterkte van de RF-puls te veranderen. Een MRI-scanner kun je instellen zodat hij de gewenste rotatie (of fliphoek) uitvoert. Hierbij geldt (tot op zekere hoogte) dat een hogere fliphoek zorgt voor een hoger signaal. Door het uitvoeren van een fliphoek neemt de magnetisatie van het object langs het externe magneetveld, de longitudinale magnetisatie, af. Dit is tijdelijk, de longitudinale magnetisatie groeit langzaam terug naar de beginstand. De tijd die het deze magnetisatie kost om te herstellen wordt de T_1 -relaxatietijd genoemd, deze is meestal enkele seconden. Als we nog een signaal opwekken voordat de longitudinale magnetisatie volledig hersteld is, zal dit tweede signaal lager zijn dan het eerste signaal. Aangezien we tijdens het maken van een MRI-scan veel signalen moeten opwekken voordat we een volledig beeld hebben opgenomen (de reden hiervoor wordt duidelijk in de paragraaf over positiecodering), is het belangrijk om te beschouwen wat er gebeurt als we veel RF-excitatiepulsen kort na elkaar afspelen.

T_1 -weging

Zoals beschreven is de T_1 -relaxatietijd meestal enkele seconden lang. De T_1 van klierweefsel in de borst is bijvoorbeeld zo'n 2 seconden bij een magneetveldsterkte van 7 T. Het meest gebruikte MRI-scanprotocol in de borst heeft een repetitietijd (TR) van 5 à 15 milliseconden. Dit betekent dat we iedere 5 tot 15 milliseconden een RF-puls afspelen om wat signaal op te wekken. Aan het begin van de scan, voordat we beginnen met de excitatiepulsen, is de longitudinale magnetisatie op zijn maximum en met de eerste fliphoek wordt een grote hoeveelheid signaal opgewekt. Deze hoeveelheid signaal zal echter met iedere herhaling afnemen, aangezien de longitudinale magnetisatie onvoldoende tijd heeft om volledig terug te groeien. Dit blijft zo doorgaan, totdat



Figuur 1: Het opgewekte signaal in de evenwichtstoestand als functie van fliphoek voor zowel vetweefsel (blauw, $T_1 = 700$ ms) als klierweefsel (geel, $T_1 = 2100$ ms) in de borst. Hogere fliphoeken vergroten het relatieve verschil in signaalintensiteit tussen deze twee weefsels. Afkorting: W.E. - Willekeurige Eenheid.

de vermindering van de magnetisatie als gevolg van de excitatiepuls even groot is als het herstel tussen twee opeenvolgende pulsen. Op dat moment is er een evenwichtstoestand bereikt. Op de kaft van dit boekje staan een paar spins in een evenwichtstoestand.

De hoeveelheid longitudinale magnetisatie in de evenwichtstoestand en de grootte van het opgewekte signaal hangen af van de T_1 van het weefsel, en van de ingestelde fliphoek en TR. Aangezien de T_1 de tijd meet die het de longitudinale magnetisatie kost om te herstellen, hebben weefsels met een kortere T_1 een hoger signaal. Scans met een langere TR geven ook een hoger signaal. De invloed van de fliphoek is iets ingewikkelder. Een fliphoek van 0 (oftewel geen fliphoek) wekt uiteraard helemaal geen signaal op. Een heel hoge fliphoek zal heel weinig signaal opwekken aangezien de hoeveelheid longitudinale magnetisatie in de evenwichtstoestand heel laag zal zijn. Tussen deze twee extremen is er een fliphoek waarbij het maximale signaal wordt opgewekt, de zogenaamde Ernsthoek. Figuur 1 zet de hoeveelheid opgewekt signaal uit tegen de fliphoek voor twee weefsels met verschillende T_1 relaxatietijden. Hogere fliphoeken zorgen ervoor dat het relatieve verschil tussen signalen van deze weefsels groter wordt. Dit concept heet T_1 -weging en maakt het mogelijk beter onderscheid te maken tussen verschillende weefseltypes met MRI.

Positiecodering

Om een beeld te kunnen maken met magnetische resonantie, moeten we achterhalen waar de opgewekte signalen vandaan komen. Zoals hierboven is besproken, resoneren protonspins in een magneetveld met de Larmorfrequentie. De signalen die we opwekken hebben dezelfde frequentie. In een MRI-scanner met een perfect homogeen magneetveld resoneren alle spins met exact dezelfde frequentie en is het onmogelijk ze van elkaar te onderscheiden. Als er echter kleine verschillen in het magneetveld zijn, zorgen die ervoor dat de resonantiefrequenties subtiel verschuiven. In dat geval kun-

nen we verschillende groepen signalen onderscheiden die worden uitgezonden door groepen protonen die op verschillende frequenties signalen uitzenden.

Om dit fenomeen in te kunnen zetten voor positiecodering, brengen we bewust en op een systematische manier verschillen aan in het magneetveld. We zetten een extra magneetveld aan, een gradiëntveld, dat lineair toeneemt van de ene kant van de scanner naar de andere kant. Bijvoorbeeld de x-gradiënt die lineair toeneemt van links naar rechts. Nu zenden alle protonen aan de linkerkant signalen uit op een lagere frequentie dan die aan de rechterkant. Om erachter te komen hoeveel protonen signalen uitzenden vanaf iedere positie, hoeven we alleen maar te bepalen hoe veel signaal we ontvangen op iedere frequentie. Door dit terug te relateren aan de posities die bij iedere frequentie horen, kunnen we een ééndimensionaal beeld van het object in de scanner maken.

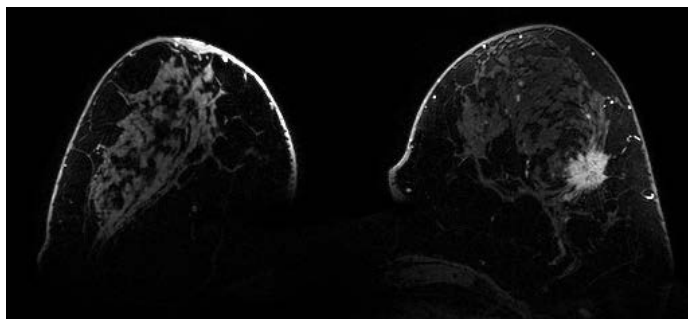
MRI-scanners hebben gradiëntspoelen in drie onderling loodrechte richtingen, waardoor we driedimensionale beelden kunnen maken. Dit gebeurt meestal door lijn-voorlijn positiegecodeerde frequenties te meten. Om het gehele object in de scanner te meten, zijn daarom vaak veel herhalingen (veel lijnen) nodig. Daarom duurt een klinische MRI-scan meestal enkele seconden tot minuten, afhankelijk van onder andere de beeldresolutie en de grootte van het beeld.

MRI van de borst op hoog magneetveld

MRI's van de borst zijn waardevol in de kliniek. Hoewel de diagnose van borstkanker meestal wordt gesteld aan de hand van mammografie (een röntgenfoto van de borst), echografie en bipten, wordt MRI routinematig ingezet voor het beoordelen van de tumor voorafgaand aan een operatie, controle van de behandelingen voortgang en bevolkingsonderzoek in hoogrisicopopulaties. De gevoeligheid van MRI voor het detecteren van invasieve borstkankers is beter dan die van mammografie en echografie. Tot slot is MRI de meest accurate beeldvormingsmodaliteit voor het bepalen van de tumorgrootte.

In de kliniek worden MRI's van de borst gemaakt op veldsterktes tot 3 T. Hogere veldsterktes, tot 7 T, worden ingezet voor klinische studies. Argumenten voor het inzetten van hogere veldsterktes voor MRI zijn onder andere een lagere hoeveelheid ruis t.o.v. het signaal en een groter verschil in signalen van protonen van verschillende soorten moleculen. Het eerste voordeel kan worden ingezet om de resolutie van de beelden te verbeteren. Hiervan is aangetoond dat dit mogelijk is in een klinische setting op een veldsterkte van 7 T en dit zou eerdere en betere diagnoses kunnen bevorderen. Het tweede voordeel kan worden ingezet om met spectroscopische technieken het tumormetabolisme in kaart te brengen. Dit soort metingen kunnen wellicht de respons op chemotherapie voorafgaand aan een operatie eerder voorspellen, waardoor sneller van therapie kan worden gewisseld indien nodig.

Het inzetten van hogere veldsterktes heeft ook nadelen. Eén van deze nadelen wordt uitgelicht in dit proefschrift: bij hogere veldsterktes worden de gebruikte elektromagnetische velden minder uniform. Het eerste elektromagnetische veld dat we verkenen is dat van de RF-excitatiepuls. Dit RF-zendveld (B_1^+) geeft aan welk deel van de elek-



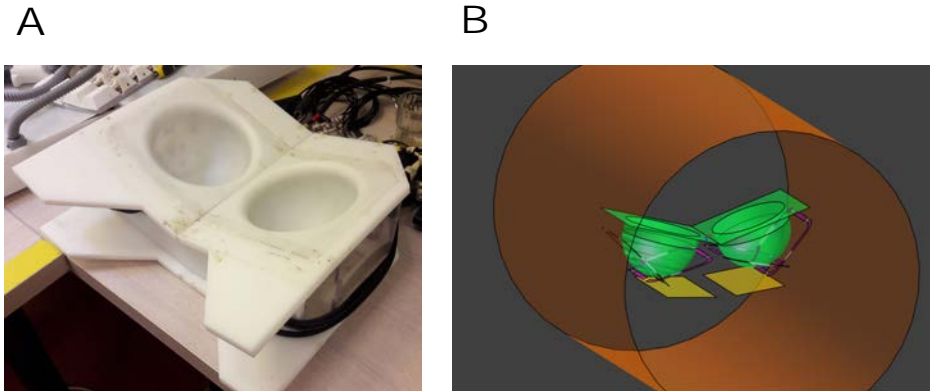
Figuur 2: Een DCE-MRI-scan, opgenomen op 7 T, van een patiënt met een borsttumor in de linkerborst (rechts in beeld). De tumor heeft een verhoogde signaalintensiteit vanwege het ingespoten contrastmiddel. Merk op dat ook dit beeld is verstoord door het B_1^+ ongelijkmatighedsartefact. Afkorting: DCE-MRI - dynamische contrast-verbeterde MRI.

tromagnetische energie van de RF-puls alle hoeken van het beeld bereikt. Het tweede elektromagnetische veld is het permanente magneetveld van de scanner zelf (B_0). De ongelijkmatigheden van deze elektromagnetische velden veroorzaken beeldfouten in de opgenomen beelden, zogenaamde artefacten. Deze artefacten kunnen zo ernstig zijn dat ze afbreuk doen aan de diagnostische waarde van de beelden. Dit proefschrift richt zich daarom op artefactcorrectie voor twee veelgebruikte MRI-beelden in de borst: dynamische contrast-verbeterde MRI (DCE-MRI) en diffusiegewogen beeldvorming (DWI).

DCE-MRI

Tijdens een DCE-MRI-scan krijgt de patiënt een T_1 -verkortend contrastmiddel ingespoten. Door hun snelle groei hebben tumoren vaak meer en lekke bloedvaten. Als gevolg hiervan zal een grotere hoeveelheid contrastmiddel vanuit de vaten de tumor inleken. Dit zorgt ervoor dat de T_1 van de tumor afneemt en dat het MRI-signaal vanuit de tumor toeneemt. Figuur 2 laat hiervan een voorbeeld zien. Na een tijdje zal het contrastmiddel weer uit de tumor terug de vaten in lekken. Een DCE-MRI-scan neemt gedurende langere tijd meerdere beelden op, zodat de snelheid van zowel de opname als de afgifte van het contrastmiddel kunnen worden vastgesteld. Dit kan worden gekoppeld aan de kwaadaardigheid van de tumor: hoe sneller de opname en afgifte, des te groter is de kans op een kwaadaardige tumor.

Al vroeg tijdens de ontwikkeling van 7 T-scanners voor het hele menselijk lichaam, werd ontdekt dat er grote ongelijkmatigheden zaten in de verdeling van het B_1^+ veld. Deze ongelijkmatigheden zijn te wijten aan de kortere golflengte van de RF-excitatiepuls op hoge veldsterktes. Dit zorgt voor staande golven in het excitatieveld en een globaal lagere B_1^+ efficiëntie. Alle 7 T MRI-experimenten in dit proefschrift gebruiken daarom lokale zendspoelen, die een hoge B_1^+ in de borst mogelijk maken. Figuur 3 laat een lokale zendspool zien zoals die is gebruikt in dit proefschrift. Aangezien deze spoelen voor het lichaam worden geplaatst en B_1^+ afneemt naarmate de afstand tot de spool groter wordt, is er een lagere B_1^+ in de achterste delen van de borst.



Figuur 3: A: Een lokale zendspool zoals die wordt gebruikt in dit proefschrift. B: Schematisch overzicht van dezelfde spool in een MRI-scanner. De cups die te zien zijn in A zijn hier in groen weergegeven. De eigenlijke spoелеlementen zijn weergegeven in paars en grijs. De oranje cilinder geeft de tunnel van de MRI-scanner weer.

Om het effect van een laag B_1^+ -niveau op de beelden te begrijpen, is het belangrijk ons te realiseren dat een laag B_1^+ -niveau betekent dat er een lagere fliphoek wordt toegepast. Zoals beschreven in de sectie over T_1 -weging, zorgt een lagere fliphoek niet alleen voor een lager signaal in de evenwichtstoestand, maar ook dat het opgenomen beeld minder T_1 -weging heeft. Met andere woorden, een laag B_1^+ -niveau zorgt ook voor een verminderde gevoeligheid voor veranderingen in T_1 . Aangezien de contrastmiddelen die worden gebruikt bij DCE-MRI de T_1 verkorten, zorgt een laag B_1^+ niveau voor een verminderde gevoeligheid voor veranderingen in de concentratie van het contrastmiddel. Dit bemoeilijkt de diagnose van tumoren.

De eerste stap om dit artefact te kunnen corrigeren, is bepalen hoeveel B_1^+ eigenlijk in ieder deel van het beeld is aangekomen. Er bestaan veel methoden om deze B_1^+ verdeling te meten. Hoewel de eerste methoden ongeschikt waren voor in-vivo metingen, vanwege praktische beperkingen variërend van zeer lange meettijden tot zeer hoge RF-vermogens, hebben recente methoden bewezen bruikbaar te zijn in een klinische omgeving met werkbare, korte meettijden. De meest gebruikte meetmethoden schatten B_1^+ aan de hand van een ratio van twee T_1 -gewogen beelden. Om te voorkomen dat deze schattingen afhankelijk zijn van de T_1 van het weefsel, gebruiken ze ofwel hele lange TR's, wat tot lange meettijden leidt, of benaderingen van de signaalvergelijking die slechts geldig zijn voor een beperkt B_1^+ -bereik.

Hoofdstuk 2 van dit proefschrift beschrijft een methode om B_1^+ in de borst op 7 T af te schatten die geen scantijd vereist en in principe ruisvrij is. Dit is mogelijk door een B_1^+ -sjabloon van de zendspool te maken en deze sjabloon toe te passen bij alle proefpersonen. We onderzoeken of het gebruik van deze sjabloon verantwoord is door de B_1^+ verdelingen van een groep vrijwilligers met een grote variatie in borstanatomie onderling te vergelijken. De prestaties van deze methode worden vergeleken met een B_1^+ meetmethode.

Het corrigeren van DCE-MRI-beelden voor B_1^+ ongelijkmatigheden is niet gebruikelijk

in de kliniek, waarschijnlijk omdat de B_1^+ velden behoorlijk homogeen zijn bij de veldsterktes die daar gebruikelijk zijn. Er zijn wel studies die dergelijke correcties hebben uitgevoerd op dergelijke veldsterktes, met als doel de concentratie van het contrastmiddel beter te kunnen kwantificeren. De meeste correctiemethoden meten de T_1 van klierweefsel voordat het contrastmiddel wordt ingespoten en corrigeren deze metingen voor B_1^+ indien nodig. Vandaaruit kunnen de T_1 en de concentratie van het contrastmiddel op ieder tijdstip van de DCE-serie worden bepaald. Er zijn methoden voorgesteld om het meten van T_1 en B_1^+ te combineren, om zo meettijd te besparen. De invloed van B_1^+ op concentratieschattingen kan fors zijn en het is aangetoond dat corrigeren voor B_1^+ zelfs nuttig kan zijn op 1,5 en 3 T, terwijl B_1^+ velden daar relatief homogeen zijn.

Hoofdstuk 3 onderzoekt het corrigeren voor B_1^+ van de gemeten beeldintensiteiten tijdens DCE-MRI. Dit gebeurt door de gemeten beeldintensiteiten bij relatief lage B_1^+ -niveaus te verhogen. Hiermee is het mogelijk de gemeten intensiteiten te corrigeren naar het juiste niveau, maar de aanwezige ruis in het beeld wordt hiermee ook opgeblazen. Daarom wordt in dit hoofdstuk een directe vertaalslag van gemeten beeldintensiteiten naar gecorrigeerde beeldintensiteiten voorgesteld die de ruisversterking minimaliseert.

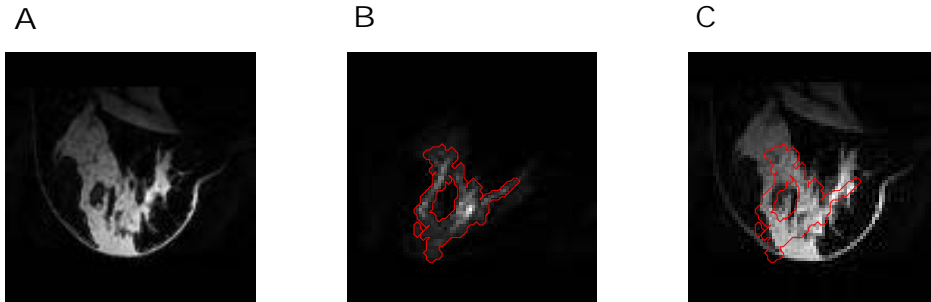
DWI

DWI is een techniek die het MRI-signaal gevoelig maakt voor de (microscopische) beweging van watermoleculen. Dit wordt bereikt door een sterke gradiënt (dezelfde gradiënt die wordt gebruikt voor positiecodering) aan te zetten die het signaal onderdrukt en even later nog een gradiënt, even sterk maar met een omgekeerd effect, die het signaal weer versterkt. De tweede gradiënt zal het effect van de eerste gradiënt tenietdoen. Dit gebeurt echter niet niet (of slechts gedeeltelijk) voor spins die in de tijd tussen de twee gradiënten zijn verplaatst. Daarom neemt de signaalintensiteit van DWI af als er meer diffusie plaatsvindt.

Aangezien tumoren vaak bestaan uit onregelmatige celstructuren is de diffusie in tumoren langzamer dan die in gezond weefsel. Als gevolg hiervan hebben tumoren een hogere signaalintensiteit op DWI-beelden. Studies hebben aangetoond dat het wellicht mogelijk is met DWI onderscheid te maken tussen goedaardige en kwaadaardige tumoren en de respons op chemotherapie te voorspellen, zonder dat het nodig is contrastmiddel in te spuiten.

DWI maakt het MRI-signaal gevoelig voor beweging om de diffusie in weefsels te kunnen meten. Er zijn echter altijd nog meer soorten beweging in een levend menselijk lichaam, met name ademhalingsbeweging en bloedcirculatie. Dit soort beweging is vaak onregelmatig en langzaam. Aangezien we alleen diffusie willen meten en geen andere soorten beweging, moeten we zo snel mogelijk meten nadat het signaal gevoelig is gemaakt voor beweging. Hoewel de meeste MRI-technieken hun beelden lijn-voor-lijn opnemen, is het daarom bij DWI gebruikelijk een geheel tweedimensionaal beeld in één keer op te nemen. Deze techniek heet echo planar imaging (EPI).

De EPI-techniek is zeer gevoelig voor ongelijkmatigheden in het B_0 -veld. Deze onge-



Figuur 4: A: Een MRI-beeld van de borst, opgenomen met een langzame lijn-voor-lijn techniek. B: Hetzelfde beeld opgenomen met de EPI-techniek. Dit beeld is vervormd ten opzichte van paneel A, hoewel is het is opgenomen in dezelfde patiënt op dezelfde locatie. C: De omtrek van het vervormde EPI-beeld in B geprojecteerd op het niet-vervormde beeld in A. Afkorting: EPI - Echo Planar Imaging.

lijkmaticheden veroorzaken geometrische vervormingen in het opgenomen beeld. Een voorbeeld van dit artefact is te zien in Figuur 4. Dit effect is te vergelijken met wat er gebeurt als je een foto neemt door een glas water of een onregelmatig gevormd glazen object. Het mechanisme achter dit effect kan conceptueel duidelijk worden als je bedenkt hoe positiecodering werkt in MRI. Aangezien het B_0 -veld niet gelijk is in de borst, zal de resonantiefrequentie ook variëren. Dit zou ervoor kunnen zorgen dat een spin aan de linkerkant van de borst resonanceert met een frequentie die te hoog is, een frequentie die we geassocieerd hadden met een positie een paar millimeter naar rechts. Ons reconstructiealgoritme zal het signaal van die spin dan, onterecht, een paar millimeter naar rechts plaatsen, wat tot een vervormd beeld leidt. Deze positioneringsfouten zullen verergeren als de verschillen in B_0 groter worden, waardoor EPI-beelden van de borst grotere verstoringen laten zien op plekken waar de B_0 ver afwijkt van het gemiddelde.

Deze onregelmatigheden in het B_0 -veld ontstaan omdat spins in verschillende weefsels in het lichaam anders reageren op het magneetveld van de scanner als gevolg van verschillen in de magnetische susceptibiliteit. Dit is vooral merkbaar bij overgangen tussen weefsels met een andere susceptibiliteit, zoals water en vet. Deze verschillen in magnetische susceptibiliteit komen veel voor in de borst, die veel overgangen van waterige weefsels naar vetweefsels bevat. Als gevolg hiervan is het B_0 -veld in de borst bijzonder ongelijkmatig.

De eerste methoden om EPI-vervormingen te corrigeren verschenen al in de jaren 90. Er zijn sinds die tijd veel verbeteringen voor deze methoden voorgesteld, net als nieuwe strategieën. De meest opvallende nieuwe strategie is een methode om voor B_0 -vervormingen te corrigeren zonder het B_0 -veld te hoeven meten. In plaats daarvan worden er twee EPI's opgenomen met tegengestelde fasecoderingsrichtingen zodat de vervormingen in beide beelden in tegengestelde richtingen gaan. Vanuit deze beelden kan een gladde B_0 -verdeling worden geschat. Deze methode werkt goed als de B_0 -verdeling glad is en is op dit moment één van de twee meest gebruikte correctiestrategieën. De andere strategie maakt gebruik van vervormbare beeldregistratie naar een niet-vervormde referentiescan, bijvoorbeeld de DCE-MRI. Hoewel deze methode ook

goede resultaten heeft opgeleverd, bestaat er altijd een risico dat het gecorrigeerde beeld wordt besmet met informatie uit het referentiebeeld (de DCE). Contrastverschillen in het DCE-beeld die niet aanwezig zijn in het oorspronkelijke EPI-beeld zouden bijvoorbeeld kunnen worden doorgegeven aan het gecorrigeerde beeld. Bovendien kan deze methode lokale vervormingen die ontstaan door steile B_0 -gradiënten bij weefselovergangen onderschatten en onvoldoende corrigeren.

In **Hoofdstuk 4** ontwikkelen we een correctiemethode om het EPI-vervormingsartefact in DWI-beelden te corrigeren. Deze techniek voorspelt de vervorming aan de hand van een gemeten B_0 -veld en compenseert vervolgens voor deze vervorming. Aangezien het B_0 -veld in de borst bijzonder ongelijkmatig is, gebruikt deze techniek hoogresolute B_0 -informatie om bestaande technieken te verbeteren.

Bij het maken van een DWI-scan kunnen de diffusieweging en de richting van deze weging worden ingesteld. Meestal worden er meerdere wegingen en meerdere richtingen opgenomen. Hierdoor kan het signaalverval als functie van de weging worden gekwantificeerd. Het gemeten signaal zal echter een mengsel van signalen zijn die ieder met een andere snelheid vervallen. Dit komt doordat watermoleculen in het lichaam verdeeld zijn in verschillende compartimenten, variërend van vrij diffunderende watermoleculen in bijvoorbeeld hersenvocht tot watermoleculen tussen cellen die worden gehinderd in hun diffusie en watermoleculen in cellen die heel beperkt kunnen diffunderen vanwege de celwand. Voor hersentumoren is aangetoond dat het scheiden van dit gemengde signaal waardevol is voor het karakteriseren van deze tumoren en dat het de zichtbaarheid van tumoren kan verbeteren.

Het kwantificeren van gemengd signaalverval met een multi-exponentieel model kan instabiele resultaten opleveren, vooral in de aanwezigheid van ruis. Een populaire methode om deze instabiliteit te omzeilen is een lineaire aanpak in twee stappen, meestal gesegmenteerde fit genoemd. Deze methode is echter gevoelig voor foutvermeerdering, aangezien de gesegmenteerde fitmethode de modelparameters opeenvolgend schat in plaats van herhalend. Dit leidt tot een afwijking in de parameterschattingen. Een nieuwe methode voor het stabiel schatten van signaalfracties in gemengde signalen, de phasortransformatie, is recente geïntroduceerd. Nadat een signaal is getransformeerd naar de phasoruimte, lijnen mono-exponentiële curves zich uit op een halve cirkel. Multi-exponentiële curves bevinden zich op de lijn die hun mono-exponentiële basiscomponenten verbindt. Dit kan worden gebruikt als voorkennis bij het fitten van een multi-exponentieel model.

Hoofdstuk 5 onderzoekt of de phasortransformatie gebruikt kan worden om gemengde vervalsignalen in DWI stabiel te kwantificeren. De prestaties van methodes geholpen door voorkennis uit de phasortransformatie wordt vergeleken met veelgebruikte methodes. De invloed van bemonsteringsstrategieën en ruis worden onderzocht in zowel digitale fantomen als vrijwilligers.

De belangrijkste bevindingen van dit proefschrift

DCE-MRI

Het verloop van tijd versus intensiteitscurves gemeten met DCE-MRI verandert in het geval van imperfecte B_1^+ : een laag B_1^+ -niveau zorgt ervoor dat de curve vlakker wordt. **Hoofdstuk 2** stelt een snelle en ruisvrije methode voor om de B_1^+ verdeling in de borst te schatten als gebruik wordt gemaakt van lokale zendspoelen op 7 T. Gebaseerd op computersimulaties van 4 vrijwilligsters werd vastgesteld dat de verschillen tussen proefpersonen wat betreft de lokale zendvelden in de borst vergelijkbaar is met de nauwkeurigheid van meetmethoden voor B_1^+ . Om deze reden hebben we voorgesteld een algemene sjabloon te gebruiken om B_1^+ te bepalen. Deze algemene sjabloon werd getest in 15 gezonde vrijwilligsters met een grote variatie in borstanatomie. In drie van deze vrijwilligsters werd de overeenkomst tussen de voorgestelde sjabloonaanpak en een meetmethode vergeleken met de overeenkomst tussen twee opeenvolgende opnames met dezelfde meetmethode. Herhaalde metingen lieten een maximale fout zien van 15% van de nominale hoek. Als de sjabloon werd gebruikt was de maximale fout iets groter, ongeveer 6%. Hieruit concluderen we dat een algemene sjabloon kan worden gebruikt bij personen met een grote variatie in borstanatomie. Hierdoor kan een tijdrovende meting met veel ruis worden weggelaten.

In **Hoofdstuk 3** gebruiken we de sjabloonaanpak van **Hoofdstuk 2** als basis om DCE-sigitaalintensiteiten te corrigeren. Met de sjabloon als bron van B_1^+ -informatie, onderzochten we het bereik van B_1^+ waarin DCE-metingen achteraf nog te corrigeren zijn. Een directe vertaalslag van gemeten naar gecorrigeerde signaalintensiteiten werd ontwikkeld om ruisversterking als gevolg van de correctie tegen te gaan. Simulaties toonden aan dat het minimale B_1^+ -niveau waarbij correctie nog kan plaatsvinden 43% van de nominale hoek is. Na correctie was de verdeling van DCE-curve types in een 7 T-dataset met kwaadaardige borsttumoren, opgenomen met een grote variatie aan B_1^+ -niveaus, beter in overeenstemming met de verdeling die bekend is uit de literatuur. DCE-correcties leken de prestaties van graadpredictiemodellen te beïnvloeden, maar dit dient verder onderzocht te worden gezien de beperkte grootte van de dataset.

DWI

DWI wordt meestal opgenomen met een EPI-techniek, die zeer gevoelig is voor geometrische vervormingen als gevolg van B_0 -ongelijkmatigheden. **Hoofdstuk 4** laat zien dat het B_0 -veld in de borst grote ongelijkmatigheden kent bij klier-vet overgangen. Om deze reden hebben we een vervormingscorrectiemethode ontwikkeld die hoogresolute B_0 -informatie meeneemt om forse vervormingen bij weefselovergangen beter op te lossen. Kwantitatieve vergelijkingen lieten zowel ex-vivo als in-vivo een betere overeenstemming zien tussen gecorrigeerde EPI-beelden en een non-EPI-referentiescan. Alle statistieken lieten een significante verbetering zien wanneer hoogresolute B_0 -informatie werd gebruikt, met name bij weefselovergangen. Het is precies deze verbetering bij weefselovergangen als gevolg van het gebruik van hoogresolute B_0 -informatie die ervoor zorgt dat onze methode een voordeel heeft ten opzichte van bestaande correctietechnieken.

Kwantificatie van de gemengde signalen gemeten met DWI is een uitdaging, aangezien steeds ingewikkeldere modellen steeds instabieler resultaten produceren. **Hoofd-**

stuk 5 verkent de mogelijkheid om met de phasortransformatie stabielere parameterschattingen te verkrijgen, zowel in de context van fractieschattingen bij vaststaande diffusiviteiten als in de context van het fitten van het intravoxel incoherent motion (IVIM) model. Hoewel de phasoraanpak bij vaststaande diffusiviteiten geen voordeel bleek te bieden ten opzichte van het eenvoudig oplossen van een lineair stelsel, produceerde de phasoraanpak voor het fitten van het IVIM-model stabielere schattingen voor twee parameters (de pseudodiffusiefractie, f , en de diffusieconstante, D) ten opzichte van zowel nonlineair als gesegmenteerd fitten.

List of publications

Publications in international journals

M.J. van Rijssel, F. Zijlstra, P.R. Seevinck, P.R. Luijten, K.G.A. Gilhuijs, D.W.J. Klomp, J.P.W. Pluim; Reducing distortions in echo-planar breast imaging at ultrahigh field with high-resolution off-resonance maps, *Magnetic Resonance in Medicine* 2019, 82(1):425-435

M.J. van Rijssel, J.P.W. Pluim, P.R. Luijten, K.G.A. Gilhuijs, A.J.E. Raaijmakers, D.W.J. Klomp; Estimating B_1^+ in the breast at 7 T using a generic template, *NMR in Biomedicine* 2018, 31(5):e3911

M.J. van Rijssel, M. Dahele, W.F.A.R. Verbakel, T.S. Rosario; A critical approach to the clinical use of deformable image registration software. In response to Meijneke *et al.*, *Radiotherapy and Oncology* 2014, 112(3):447-448

M.A.J.M. van Eijnatten, M.J. van Rijssel, R.J.A. Peters, R.M. Verdaasdonk, J.H. Meijer; Comparison of cardiac time intervals between echocardiography and impedance cardiography at various heart rates, *Journal of Electrical Bioimpedance* 2014, 5(1):2-8

Manuscripts submitted for publication

M.J. van Rijssel, J.P.W. Pluim, H.M. Chan, L. van den Wildenberg, A.M.Th. Schmitz, P.R. Luijten, K.G.A. Gilhuijs, D.W.J. Klomp; Correcting time-intensity curves in dynamic contrast-enhanced breast MRI for inhomogeneous excitation fields

M.J. van Rijssel, M. Froeling, A.L.H.M.W. van Lier, J.J.C. Verhoeff, J.P.W. Pluim; Untangling the diffusion signal using the phasor transform

Conference abstracts

L. van den Wildenberg, E. Krikken, J.P. Wijnen, J.P.W. Pluim, D.W.J. Klomp, M.J. van Rijssel; Correcting breast MRI with a generic B_1^+ template for T_1 map calculation, *International Society for Magnetic Resonance in Medicine*, 2019

M.J. van Rijssel, F. Zijlstra, P.R. Seevinck, P.R. Luijten, D.W.J. Klomp, J.P.W. Pluim; High-resolution off-resonance maps improve conformity between distortion-corrected EPI acquisitions and distortion-free references, *International Society for Magnetic Resonance in Medicine*, 2018

M.J. van Rijssel, M. Froeling, J.P.W. Pluim; Where's my water? Untangling the diffusion signal using the phasor representation, *International Society for Magnetic Resonance in Medicine*, 2018

M.J. van Rijssel, F. Zijlstra, P.R. Seevinck, P.R. Luijten, D.W.J. Klomp, J.P.W. Pluim; Susceptibility-induced local ΔB_0 variations are essential for predicting EPI distortions in the breast, *International Society for Magnetic Resonance in Medicine*, 2017

M.J. van Rijssel, J.P.W. Pluim, P.R. Luijten, A.J.E. Raaijmakers, D.W.J. Klomp; Estimating B_1^+ of the breast at 7T using a generic distribution, *International Society for Magnetic Resonance in Medicine*, 2016

M.J. van Rijssel, J.P.W. Pluim, B.H.M. van der Velden, T.A. van der Velden, E. Krikken, J.P. Wijnen, K.G.A. Gilhuijs, D.W.J. Klomp; Evaluation of image-based bias field correction at 7 T, *European Society for Magnetic Resonance in Medicine and Biology*, 2015

Dankwoord

Dit boek staat vol met teksten die ik zelf nooit had kunnen schrijven, experimenten die ik alleen nooit had kunnen uitvoeren en goede ideeën die ik nooit had kunnen bedenken. Het wordt hoog tijd dat ik de mensen ga bedanken die dit toch mogelijk hebben gemaakt. De afgelopen jaren heb ik mogen werken in een geweldige groep vol met slimme, enthousiaste, gemotiveerde, grappige en gekke mensen. Het is vrij uniek om (PhD-)onderzoek te kunnen doen in zo'n grote en leuke groep en ik vond het een fantastische tijd. Ik wil iedereen die hieraan heeft bijgedragen dan ook hartelijk bedanken!

Aan het begin van dit dankwoord moet ik natuurlijk de man bedanken dankzij wie mijn Utrechtse avontuur begon: **Dennis**. Hoewel ik tegenwoordig prof.dr. Dennis moet zeggen. Jouw aanstekelijke enthousiasme heeft me ertoe overgehaald om voor dit project naar Utrecht te verhuizen en heeft me meerdere keren op de been geholpen als het niet helemaal liep zoals we wilden. Bedankt voor het blijven uitdagen van mijn sceptische houding met je positieve instelling en een niet aflatende stroom aan nieuwe ideeën. Iets is slechts onmogelijk tot het niet meer zo is.

Josien, je bent wel professor in 'Medical Image Analysis', maar zeker niet MIA! Door je aanstelling in Eindhoven was je meestal slechts één dag in de week in Utrecht, maar dit heeft je er niet van weerhouden actief betrokken te blijven bij al mijn projecten. Bedankt voor je luisterend oor, goede suggesties, snelle feedback, (zwarte) humor en aanhoudende betrokkenheid op vele gebieden. Stop nooit met luisteren.

Kenneth, door het MR-fysische karakter van het werk dat ik in de afgelopen periode heb gedaan, dreigde jij soms aan de zijlijn te belanden. Desondanks, of misschien juist daardoor, was jouw feedback op mijn werk of de presentatie daarvan altijd bijzonder waardevol, met name als je aangaf bepaalde delen "niet te snappen". Ha, daar trap ik dus niet meer in! Voor alle huidige en toekomstige studenten van Kenneth: hij snapt alles, hij is alleen bang dat je punt niet overkomt. Kenneth, ik heb veel van je geleerd en waardeer je anekdotische aanpak om ingewikkelde concepten over te brengen. Wordt vervolgd.

Peter, door het succes van Dennis en het door de universiteit gestelde maximumaantal promotoren sta jij niet meer als zodanig in dit boekje. Het siert je dat je deze stap opzij hebt gedaan. Ik wil je graag bedanken voor het opzetten van de geweldige 7T-groep waar ik de afgelopen jaren mee heb mogen samenwerken en de vrijheid die je me hebt gegeven tijdens het uitvoeren van mijn onderzoek.

Ik wil graag alle leden van de beoordelingscommissie, prof. **Paul van Diest**, prof. **Arend Heerschap**, prof. **Jan Lagendijk**, prof. **Chrit Moonen** en prof. **Aart Nederveen**, van harte bedanken voor uw interesse in mijn werk en de discussie die ik met u mag voeren.

Alexander Raaijmakers, als er iemand is die mij het belang van het goed bewaren van oude resultaten heeft laten inzien, dan ben jij het wel. Het is inmiddels bijna vijf jaar geleden dat ik je om wat oude simulaties vroeg, die je ook nog bleek te hebben! De rest is geschiedenis, maar zonder deze vliegende start hadden de eerste twee hoofdstukken van dit boekje er heel anders uitgezien.

Frank, onze zelfbedachte EPI-ervormingscorrectiemethode blijft de beste. Zelfs nu is gebleken dat we bij lange na niet de eersten waren die op dit idee zijn gekomen. Ik wil je bedanken voor veel nuttige inhoudelijke discussies, schaamteloos gestolen code (waaronder de LaTeX-template voor dit proefschrift) en je gezelschap tijdens meerdere congressen. Tea! Earl Grey! Hot!

Lieke, je begon bij ons als masterstudent en je hebt je sindsdien ontwikkeld tot een uitstekend onderzoekster. Ik ben dan ook erg trots om je als coauteur op één van de hoofdstukken in dit boekje te mogen vermelden! Geniet van je tijd als PhD-student in deze geweldige groep.

Martijn, bedankt dat je onmiddellijk enthousiast was over dat rare phasor-idee van mij. Toen het toch niet helemaal bleek te zitten hoe wij dachten, heb jij me aangespoord om dan maar goed uit te zoeken hoe het wel zit en daar is een prachtig hoofdstuk uit voortgekomen. Het was ook jouw idee om **Astrid** en **Joost** erbij te betrekken, die me lieten inzien hoe snel de resultaten relevant zouden kunnen zijn voor radiotherapiepatiënten. Ik zie er dan ook naar uit om binnenkort jullie collega te worden!

Bas, vanaf dag één heb je me veel geholpen met vaak praktische oplossingen en nuchtere inzichten. Ik ben dan ook erg trots dat je me niet zo lang geleden om hulp vroeg bij één van jouw artikelen en dat ik daarop coauteur mag zijn. Bedankt voor deze mooie samenwerking, maar nog veel meer voor je droge gevoel voor humor en het feit dat je deur altijd voor me openstond.

Hui Shan, bedankt dat je het bijna vijf jaar met mij in één kantoor hebt uitgehouden. Ik ben blij dat ik je in deze tijd beter heb leren kennen. Ik heb er een gewoonte van gemaakt om je suggesties voor goede boeken, series en films op te volgen en heb daar tot zover nog nooit spijt van gekregen. Mijn suggesties volg je slechts sporadisch op, vermoedelijk alleen als ze 'Niko-approved' zijn (of als hij er een DVD-box van heeft liggen). Ik wil trouwens nog even sorry zeggen voor de roddels over jou en Niko die ik probeerde te starten. Dat had ik pas veel later moeten doen, dan had ik ze nooit hoeven tegenspreken. Ik ben dankbaar dat je tijdens mijn verdediging achter me wil staan. Veel succes met de laatste loodjes van je eigen scriptie!

Erik, ik zal onze interessante discussies en je goede grappen missen. Je bent met recht de man van de juiste grap op het juiste moment. Bedankt dat je me wil steunen op de dag van de verdediging. Nu je niet meer embargo-restricted bent, knal je die PhD gewoon even binnen. **Jurica**, I believe I've never met a man who's so fond of The Sound of Silence. And of stating facts. A true herald of science. All the best with your career in industry! **Alexander Schmitz**, onze tijd in één kantoor was kort maar krachtig. Vooral die stem van jou. Geniet van je tijd in Amsterdam, je wordt een bazenradioloog!

Erwin, bedankt voor je hulp tijdens vele uren scannen en de prettige samenwerking. Met je positieve insteek en relaxte, zelfverzekerde houding ga je ver komen! **Tijl**, vooral in het begin was jij van onschatbare waarde voor mij om die scanner te laten doen wat ik wilde, zonder dat hij daarbij stuk ging. Ik denk dat dat grotendeels gelukt is. **Fredy**, bedankt dat je je hoofd koel hield in een (voor mij) zeer stressvolle situatie. **Jannie**, bedankt voor alle scherpe inzichten en goede adviezen door de jaren heen. Hoewel je

technisch gezien niet mijn begeleider was, was je altijd uitstekend op de hoogte van waar ik mee bezig was. Het belooft daarom een interessante discussie te worden tijdens mijn verdediging, ik hoop dat je nog een spaan van me heel laat.

Fenghua, aka the restaurant classifier, thank you for the cup of Chinese tea on my very first day. A good beginning for every great adventure. **Samuel**, some facts of life for you: 1) People don't hate you. You've made at least one friend in Utrecht, and I'm sure I'm not the only one. 2) Most people couldn't come up with the crazy science-stuff you come up with. Don't underestimate yourself. 3) T-shirts should have four holes. No less, that would be impractical, and definitely not more.

Majd and **Niko**, thanks for all the fun we had in Sicily. We now know everything there is to know about Sicilian lunch and coffee break traditions. I'll never eat tuna again in my life. **Szabolcs**, though our water polo career together was short-lived, I remember fondly our lengthy discussions that invariably started with you saying the phrase "I have a question.". May you never cease to ask questions! **Bea**, thank you for your enthusiasm and for bringing people together in many Harry Potter-themed occasions. Differences of habit and language are nothing at all if our aims are identical and our hearts are open.

Mariëlle, **Britt**, **Sandra** en Hui Shan, bedankt dat ik samen met jullie de MISP heb mogen organiseren. Sorry dat ik er op het moment suprême niet bij kon zijn. **Hugo**, **Matthijs**, **Edwin** en **Chris**, bedankt dat ik onderdeel mocht zijn van jullie vaste lunchclubje tijdens mijn tijd op Q2. Ik voelde me altijd welkom. **Julia**, ik vond het leuk om samen met jou te kunnen trakteren voor onze verjaardagen. Veel succes in het AMC!

Marjan, **Jacqueline**, **Renée**, **Maria** en **Sylvia**, bedankt voor alle ondersteuning door de jaren heen en jullie hulp bij allerlei ingewikkelde verzoeken van mijn kant. Jullie waren vooral onmisbaar als het nodig was om al mijn begeleiders op hetzelfde moment bij elkaar te krijgen. Sorry voor alle hoofdpijn die dit jullie gekost moet hebben. Zonder jullie is er geen 7T, ISI, Imago of CIS!

Their may be some of you who are slightly disappointed not to see their name immortalized in this book. Fret not, dear lunchmate, fellow Potterhead, tea lover or otherwise amazing person. I did not forget you! I think. It's a good thing I have all of you to help me remember.

Er zijn veel mensen buiten het UMC die ik hier even in het zonnetje wil zetten. Bedankt voor alle goede gesprekken, gezellige avondjes en meestal verloren waterpolowedstrijden. Ik heb het onder andere over ToMaMoMaDeMiMa, het Clubje van 11, ex-Heren 4 en Heren 7/8. Jullie weten wie jullie zijn!

Lieve **Pa**, **Ma** en **Ronald**, jullie hebben misschien het gevoel dat jullie niet zo veel aan dit boekje hebben bijgedragen, maar niets is minder waar! Jullie hebben me de ruimte gegeven en de kansen geboden om me te ontwikkelen tot wie ik nu ben. Sorry voor alle avonden die ik in stilte achter mijn bureau zat, terwijl ik probeerde een of ander triviaal feitje of wiskunde-trucje onder de knie te krijgen. Zonder jullie had ik dit nooit allemaal kunnen doen. Of leren fietsen. Of met een lepel eten. Bedankt voor alles!

Tot slot, lieve **Monique**, jij bent degene die me ervan weerhoudt de hele dag met werk bezig te zijn, die ons huis een thuis maakt en me meeneemt de wijde wereld in. Bedankt voor alle knuffels, je vertrouwen en je steun. Samen gaan we naar plekken waar niemand eerder is geweest!

&

About the author



Mike van Rijssel was born in Rijsenhout on May 10th, 1991. He obtained his Bachelor of Science degree from the VU University in Amsterdam in 2012, *cum laude*. His bachelor thesis work at the Department of Physics and Medical Technology of the VU medical center led to his first publication in an international scientific journal. He obtained his Master of Science degree in Medical Natural Science, specialization Medical Physics from the VU University in Amsterdam in 2014, *cum laude*. During his time in Amsterdam, he gained research experience in the Department of Radiation Oncology at the VU medical center and in the Netherlands Institute for Neuroscience.

Mike started his PhD research in the University Medical Center Utrecht under the supervision of prof. dr. Josien Pluim, prof. dr. Dennis Klomp, and dr. Kenneth Gilhuijs in 2015. The results of this work are presented in this thesis.

